UCRL-LR-139295

Spectroscopy of Middle Charge State High-Z Ions in the Ultraviolet for Plasma Diagnostics

S.B. Utter
(Ph.D. Thesis)

December 11, 1999

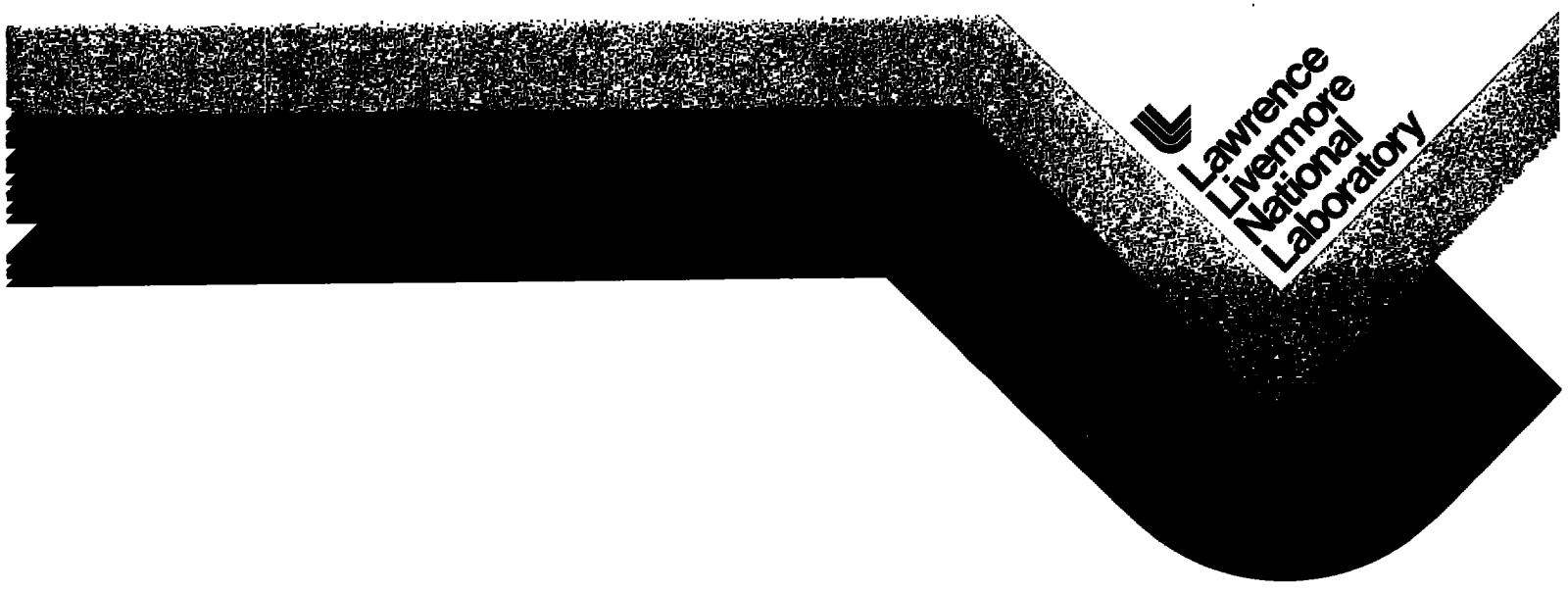

DISCLAIMER

Work performed under the auspices of the U. S. Department of Energy by the University of California Lawrence Livermore National Laboratory under Contract W-7405-Eng-48.

UCRL-LR-139295
Distribution Category UC-71

Spectroscopy of Middle Charge State High-Z Ions in the Ultraviolet for Plasma Diagnostics

S.B. Utter
(Ph.D. Thesis)

Manuscript date: December 11, 1999

LAWRENCE LIVERMORE NATIONAL LABORATORY
University of California • Livermore, California • 94551

SPECTROSCOPY OF MIDDLE CHARGE STATE HIGH-Z IONS IN THE ULTRAVIOLET FOR PLASMA DIAGNOSTICS

Steven Bryan Utter

A Dissertation

Submitted to

the Graduate Faculty of

Auburn University

in Partial Fulfillment of the

Requirements for the

Degree of

Doctor of Philosophy

Auburn, Alabama

December 11, 1999

VITA

Steven Bryan Utter, son of James and Barbara (Ryan) Utter, was born December 3, 1969, in Covington, Kentucky. He graduated *summa cum laude* from Saint Mary High School in Paducah, Kentucky, in 1988. He then entered Eastern Kentucky University in Richmond, Kentucky, and graduated *summa cum laude* with a Bachelor of Science degree in Physics in May, 1992. Subsequently, he entered Graduate School, Auburn University, in September, 1992. In January of 1997, he moved to Livermore, California to perform atomic spectroscopy research at the EBIT facility at Lawrence Livermore National Laboratory. He married Bonnie Nichols, daughter of William and Judith (Isert) Nichols, on April 25, 1998.

ABSTRACT

SPECTROSCOPY OF MIDDLE CHARGE STATE HIGH-Z IONS

IN THE ULTRAVIOLET FOR PLASMA DIAGNOSTICS

Steven Bryan Utter

Doctor of Philosophy, December 11, 1999
(M.S., Auburn University, 1996)
(B.S., Eastern Kentucky University, 1992)

Directed by Eugène J. Clothiaux and Peter Beiersdorfer

The quest for the creation of an economically feasible thermonuclear fusion energy reactor is still active after many decades of research. Modern machines produce plasmas which are both hotter and more dense than those created 30 years ago and future devices promise to continue this trend. Paramount to this research is the capability to adequately measure certain parameters of the plasma such as temperature, density, impurity concentration and radiation loss. This dissertation reports three sets of spectroscopic measurements from intermediate charge state of high-Z ions, which have been performed at the Electron Beam Ion Trap (EBIT) facility of the Lawrence Livermore National Laboratory[1], relevant to the development of spectral plasma diagnostics and to the understanding of radiative energy loss from heavy impurity ions of today's and future fusion devices: measurements of W radiation from 40 – 85 Å, precision measurements along the Cu isoelectronic sequence, and UV spectroscopy of Ti-like W. The results are also compared to the best available theoretical calculations.

[1]This work was performed under the auspices of the United States Department of Energy by Lawrence Livermore National Laboratory under contract number W-7405-ENG-48.

ACKNOWLEDGMENTS

Thanks are in order for many people who have influenced my research, and my life, during my years as a graduate student and the completion of this dissertation. Firstly, Peter Beiersdorder, who has served as my advisor during my 3 years at LLNL, whose dedication and enthusiasm have been an inspiration to my work at EBIT, but most importantly, who has served as a model of excellence, successfully juggling the roles of spectroscopy group leader and research scientist. The quality of this work, and that of much of the EBIT research during the last decade, is a direct result of the his influence.

My gratitude also extends to my Auburn advisor, Eugène Clothiaux. Through his instruction he instilled in me the basic tools necessary to understand the rules of mathematics and concepts of physics required to pursue a career as a research scientist, and who allowed and encouraged me to pursue spectroscopy research at the LLNL-EBIT facility 2500 miles from Auburn.

Greg Brown – my classmate, office-mate, roommate, and friend. Having studied and worked together for nearly seven years we have tackled many problems together as graduate students. The hours spent working through tough problems, both mathematical and technical, have only made me a better student, researcher and person.

Klaus Widmann and Jeff Weinheimer – who each represent the epitome of what a skilled and dedicated student and physicist should be – as well as all the other students with whom I have worked and studied throughout the years. The wealth of knowledge gained amongst the ignorant masses working together is amazing.

The many people from whom I have learned much about laboratory physics, particularly Elmar Träbert and Joserra Crespo López-Urrutia, who have spent many hours with me in the laboratory teaching me about the tools and techniques of spectroscopic research.

Kevin Fournier, whose calculations have been of particular interest to this work, and who willingly offered to provide theoretical results for the intermediate W charge states specialized to EBIT conditions.

The management and staff at LLNL as well as the faculty and staff at Auburn University for the educational support offered through these top notch institutions, particularly Bill Goldstien, the director of the LLNL Department of Physics, Andi Hazi, the V-division leader, and the EBIT technical staff - Dan, Ed, Phil, Ken, Joey, and Jeff. And a special thank you to Candace Lewis, who has been a continuous source of support, as well as a friend.

Finally, my wife, Bonnie, who agreed to take on the challenge of moving to a state thousands of miles from friends and family in order for me to pursue my career goals. And my family, for being in total support of my education, which has moved me so far away.

Style manual used:

Physical Review Style and Notation Guide

Chicago Manual of Style

Computer software used:

PMIS Image Processing Software Ver. 2.0.1,

GKR Computer Consulting, Boulder, CO

Origin Ver. 4.0, 4.1, and 5.0, Microcal Software, Inc., Northampton, MA

Origin Peakfit Module, Microcal Software, Inc., Northampton, MA

Word 97, Microsoft Corporation, Redmond, WA

Excel 97, Microsoft Corporation, Redmond, WA

CorelDRAW Ver. 8.369, Corel Corporation, Ottawa, Ontario, Canada

AutoCad LT for Windows 95, Autodesk, Inc., San Rafael, CA

MathCAD Plus Ver. 5.0, MathSoft Inc., Cambridge, MA

Borland C++, Inprise Inc., Scotts Valley, CA

PCTEX for Windows, Personal TEX, Inc., Mill Valley, CA

CONTENTS

1 INTRODUCTION 1

2 PLASMA DIAGNOSTICS 3

2.1 Tungsten in the EUV 4

2.2 Cu-like ions: Transitions in the EUV 6

2.3 Tungsten in the Near UV 8

3 THE ELECTRON BEAM ION TRAP 12

3.1 Working Principles and Operation 13

3.1.1 Electron gun 15

3.1.2 Electron beam 17

3.2 Ions 20

3.3 Trapping physics 22

3.4 Electronic versus Magnetic Trapping Mode 25

3.5 Spectroscopic observation 27

4 SPECTROSCOPIC INSTRUMENTATION 30

4.1 Extreme Ultraviolet Spectroscopy on EBIT 31

4.1.1 EUV Spectroscopy Basics 31

4.1.2 The Flat Field Gratings 32

4.1.3 The Spectrometer Housing 37

4.2 Transmission Spectrometer 40

4.3 CCD Detectors 42

5 TUNGSTEN IN THE EUV 48

5.1 Theoretical predictions 48

5.2 Experimental Setup 51

5.2.1 Wavelength calibration 55

5.2.2 Intensity calibration 57

5.3 Experimental Results 59

5.4 Discussion 69

6 CU-LIKE IONS 75

6.1 Theoretical predictions of the energy of the $4s_{1/2} - 4p_{3/2}$ transitions . 76

6.2 Wavelength measurements of the $4s_{1/2} - 4p_{3/2}$ transition 81

6.2.1 Ytterbium 84

6.2.2 Tungsten 86

6.2.3 Gold 86

6.2.4 Lead 87

6.2.5 Thorium 88

6.2.6 Uranium 89

6.3 Error Aanalysis 90

6.3.1 Statistical errors 91

6.3.2 Systematic errors 92

6.4 Summary of results 94

7 TI-LIKE W^{52+} IN THE NEAR UV 98

7.1 Measurement of the ground term $J = 2 - 3$ transition of Ti-like W . . 99

7.2 Results 110

8 SUMMARY 114

8.1 Results 114

8.2 Suggestions for future research 118

A TABLES OF LINES AND ENERGIES 119

A.1 Calibration Lines 119

A.2 Ionization Energies 122

B CONCAVE GRATING THEORY 123

B.1 Uniformly Spaced Grooves 123

B.2 Variably Spaced Grooves 129

C CCD FILTER PROGRAM 132

LIST OF FIGURES

2.1 Comparison of hydrogen-like and copper-like systems 7

2.2 Two M1 transitions: one showing an unusual property of wavelength invariance with Z 10

3.1 Diagram of EBIT 14

3.2 Diagram of MeVVA injection system 21

3.3 Top, middle, and bottom drift tube showing trapping potentials. . . . 23

3.4 Typical EBIT timing pattern for MeVVA injection 26

3.5 Cross-sectional view of EBIT including an expanded section showing internal apertures 28

4.1 Spectra taken with the 1200 l/mm grating showing calibration and improving resolution with spectral order 36

4.2 Spectrum from the 1200 l/mm grating demonstrating how the multiple orders produced can at times be detrimental 37

4.3 Diagram of flat field spectrometer system 38

4.4 Diagram of transmission grating spectrometer on EBIT 41

4.5 CCD readout sequence 44

5.1 Simulated spectra made using the predictions of Fournier 50

5.2 System for sequential W data acquisition 54

5.3 FFS efficiency curve by Saemann and Eidmann 59

5.4 FFS raw data for series of W spectra 61

5.5 FFS line-out spectra at the optimal energies for each of the nine measured W charge states 70
5.6 Se-like W compared to simulated spectrum 71
6.1 Comparison of transition energies predicted by Kim *et al.* and the measured values from sources other than EBIT 79
6.2 Comparison of transition energies predicted by Blundell and those predicted by Kim *et al.* 80
6.3 Example of a Cu-like $4s_{1/2} - 4p_{3/2}$ transition measurement 83
6.4 Au spectrum showing a weak line at a wavelength just shorter than the measured Cu-like line 93
6.5 Comparison of Kim's predictions to experimental data including that from EBIT 96
7.1 Comparison between trapped and untrapped photon emitting ions . . 104
7.2 Neon and krypton spectra for calibration of TGS 105
7.3 TGS W spectrum and beam energy dependence 107
7.4 Ti-like $J = 2 - 3$ ground state transition wavelengths predicted by Feldman *et al.* and measured at various EBITs 112
B.1 Diagram of concave grating 124
C.1 Chart of CCD PMIS file cosmic-ray/bad-pixel filtering program . . . 134

LIST OF TABLES

3.1 Electron gun parameters 16

3.2 Comparison of two electron beam compression techniques 17

3.3 Determination of the limiting aperture inside EBIT vacuum chamber 29

4.1 Variable line spaced concave reflection grating properties 35

4.2 CCD technical data and properties 46

5.1 Electron beam energy steps for the W wavelength measurement . . . 56

5.2 List of predicted and measured Rb-like W transitions 63

5.3 List of predicted and measured Kr-like W transitions 64

5.4 List of predicted and measured Br-like W transitions 65

5.5 List of predicted and measured Se-like W transitions 66

5.6 List of predicted and measured As-like W transitions 67

5.7 List of predicted and measured Ge-like W transitions 67

5.8 List of predicted and measured Ga-like W transitions 68

5.9 List of predicted and measured Zn-like W transitions 68

5.10 List of predicted and measured Cu-like W transitions 69

6.1 Predicted and measured wavelengths of the $4s_{1/2} - 4p_{3/2}$ transition in Cu-like ions 95

7.1 $J = 3$ to $J = 2$ or $J = 4$ branching ratio 100

A.1 Calibration lines for the FFS spectra described in this work 119

A.2 Calibration lines used with the TGS 121

A.3 Ionization energies 122

1 INTRODUCTION

The goal of achieving economically significant amounts of energy from controlled thermonuclear reactions is one of the driving forces in the study of plasma physics. Plasma diagnostics is the term used for the study of plasma parameters in order to deduce information about the state of the plasma from observations of physical processes and their effects [1]. There are numerous techniques available to the experimentalist to gather information about the state of the plasma inside of a plasma device. For example, the magnetic field strength in the plasma can be measured by inserting coils and probes into the plasma itself and ion processes can be studied with probing beams of heavy particles. Both of these measurements are classified as intrusive, or active, measurements, since the insertion of foreign material directly affects the properties of the plasmas themselves and the interpretation of data must take this into account. Passive measurements are most often prefered, especially in such situations as when the insertion of a probe is not only impractical, but impossible. The high temperatures achieved in the fusion plasma may preclude the possibility of the insertion of probes. It is for this reason that spectroscopy, the passive study of electro-magnetic radiation emitted from the plasma, has taken a leading role in the diagnostics of present generation fusion devices and will continue to be a necessary tool to achieve the goal of energy production in future generation machines.

This dissertation is organized as follows: Chapter 2 gives a brief description of the motivation for the measurements made for this dissertation and an overview of the current state of theory and experiment for each related topic. In Chapters 3 and 4

are found a thorough description of the equipment used to create the intermediate charge state ions – EBIT – and the spectroscopic instrumentation built as part of this work to make the observations. The following three chapters offer detailed theory, experimental technique, and analysis of the three measurements: a survey of W spectra in the EUV, precise measurements of the Cu-like resonance transitions from Z = 70 to Z = 92, and the study of a Ti-like transition in the near UV predicted to have unusual Z-scaling behavior. The final chapter summarizes all of the work and puts it in the perspective of plasma diagnostics.

2 PLASMA DIAGNOSTICS

Present day plasma devices typically operate with electron temperatures in the range of 1–5 keV with densities varying from $10^{12} - 10^{14}$ electrons/cm^3 for tokamak plasmas to $10^{19} - 10^{23}$ electrons/cm^3 for laser produced plasmas. It is anticipated that future plasma devices will be even hotter and more dense, and therefore there is a continuing need for the development of plasma diagnostics to address the needs of these present and future devices. Of particular interest in this work is the study of the spectra of intermediate charge state ions which can be used in the study of future generation low-density, high-temperature devices. Such ions are in the upper half of the periodic table and have ionization energies in the range 1–6 keV. Under such conditions as will be present in these plasma devices, high-Z elements will be partially ionized, but will typically have a few to many electrons still bound to the nucleus. For instance, tungsten, which has seventy-four electrons in its neutral state, will achieve a charge state of W^{28+} (forty-six electrons remaining) when ionized by electrons with energy near 1 keV, and a charge state of W^{59+} (fifteen electrons remaining) if the bombarding electron energy is raised to 6 keV. Though no hard, fast rule will be established here to designate "intermediate charge states", it is this type of ion which is discussed here.

2.1 Tungsten in the EUV

Of particular interest in plans for future generation fusion devices, such as the International Thermonuclear Experimental Reactor (ITER), is the spectroscopy of tungsten (W) ions in the intermediate charge state regime. Presently in tokamaks, in-vessel components, including the divertor and the first wall, are typically constructed out of low-Z materials such as carbon or beryllium [2]. This choice arose out of the realization during the testing of first generation tokamaks that high-Z material emitted from the chamber walls penetrated into the center portion of the plasma and radiated a large fraction of the power [3]. Attempts made to correct for this deleterious effect by adding small amounts of neon or oxygen as a buffer were insufficient and the choice was made to incorporate lower-Z material surfaces. Sputtered particles from these become fully stripped and then no longer radiate at typical tokamak plasma temperatures. These materials, however, will not satisfy the more stringent requirements of higher-energy machines due to their large sputtering and evaporation rates, as well as their inability to dissipate the intense heat load anticipated in ITER [4]. Some of the requirements of the plasma facing materials should be [5]:

- high heat conductivity and capacity
- high melting point and large thermal shock resistance
- good machining properties
- little degradation of the thermophysical properties with time and use
- low activation and transmutation due to 14 MeV neutron flux
- low permanent tritium retention

- low erosion due to impact by plasma ions and neutrals
- low erosion due to local effects such as electrical arcs or hot spots
- low self-sputtering
- low energy loss by radiation in the central plasma region

Though not all of these properties can be found in any single material, high-Z materials such as W satisfy most of the criteria. Recent studies have been conducted which suggest that W should in fact be the material of choice, at least for divertors and similar structures that bear particularly high heat loads and are exposed to the plasma [2, 4, 5, 6]. Therefore, it is necessary to have available precise measurements of the spectra of W ions, suitable for comparison to theory, for calculation and determinations of particle transport and impurity radiative power loss rates. In plasmas with electron temperatures roughly between $0.3 < T_e < 2$ keV more than half of the total energy emitted by W is expected to fall in the wavelength band of 30 - 70 Å, a region of the electro-magnetic spectrum known as the EUV [3].

Some atomic spectroscopic data from W in the EUV has previously been published. For instance, high-resolution measurements of selected radiative transitions from Fe-, Co-, Cu-, and Zn-like W ions have been made using laser-produced plasmas [7, 8, 9]. Other spectroscopic investigations of W in the EUV have been performed using tokamaks and report the presence of pseudo-continua or bands of radiation as well as isolated lines [3, 10, 11, 12]. These lines are expected to arise from overlapping N-shell ($n = 4$) transition arrays of successive intermediate charge states in W (W^{27+} - W^{55+}), but the measurements were unable to resolve the closely spaced lines. In addition to these measurements, detailed calculations have been performed of the

transition wavelengths, oscillator strengths, and collisional-radiative line intensities for W ions from Co-like W^{47+} to Rb-like W^{37+} [13].

Even though there is an extensive list of measurements and calculations for intermediate charge state W ions, the data is, none-the-less, incomplete. For instance, the high-resolution measurements obtained with laser-produced plasmas are complicated by the fact that many charge states of W are present simultaneously. Since the transitions from successive ions are very similar in nature, – low-l valence electrons experience similar screening, even as the number of core electrons of higher l may differ – they also often occur at nearly the same wavelengths. The presence of many charge states at one time makes accurate measurements of all but the strongest lines futile, even with state-of-the-art spectrometer systems. Additionally, these spectra are obtained at higher densities than those of a typical tokamak plasma by five or more orders of magnitude, so that the atomic processes at work in the creation of the spectra will be somewhat different from lower density plasma sources. As for the spectra presently available from tokamak plasmas, these spectra lack the spectral resolution as well as the charge-state resolution necessary to satisfactorily measure all of the spectral features. The most complete information on the spectra of intermediate charge state W does, indeed, come from the calculations referred to previously [13]. However, it is necessary to provide experimental data with sufficient precision to be used as a measure of the accuracy of such comprehensive calculations.

2.2 Cu-like ions: Transitions in the EUV

In order to test the accuracy of the best calculations of energy levels in intermediate charge state ions, it is useful to look in some detail at what may be considered

a 'simple' system. The best understood of all atomic systems are those of the hydrogen isoelectronic sequence, having only a single electron bound by the Coulomb attraction to the nucleus. Hydrogen-like systems are used in precision tests of such quantities as QED corrections to atomic energy levels or the distribution of magnetic fields in the nucleus, the so-called Bohr-Weisskopf effect [14]. In the range of atomic number, ionization energies and photon energies considered here, the Cu-like system best mimics a H-like system, having, instead of a single electron outside of the nucleus, a single valence electron outside of a closed $n = 3$ electron-orbital shell. (See Fig. 2.1.) It is also profitable to examine a series of transitions along an isoelectronic

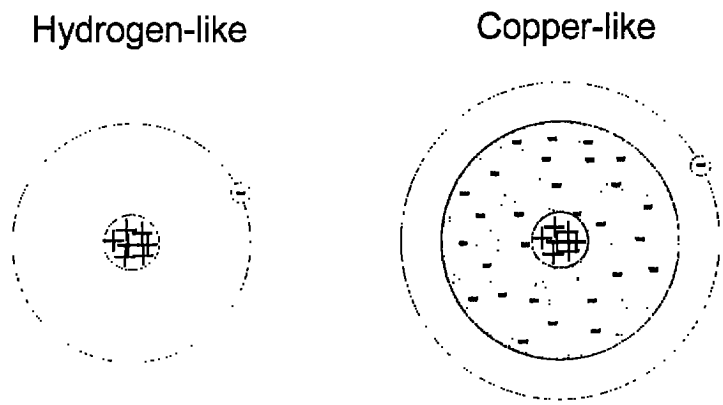

Figure 2.1: Conceptual drawing comparing the hydrogen-like system, having a single bound electron, to the Cu-like system, having twenty-nine electrons, only one of which is outside of the closed $n = 3$ shell. Due to the shell closure, the Cu-like system is said to 'mimic' the H-like system and is, therefore, a good testbed for calculations of the atomic structure of multiply charged ions.

sequence. In this manner effects that vary as a function of Z, such as relativistic effects, screened self-energy, vacuum polarization, and level crossings, may be examined in detail since complications arising from the variation in the atomic electron interactions are minimized.

Calculations of the energies of the $4s_{1/2}$ and $4p_{3/2}$ states are typically carried out either *ab initio* via relativistic many-body perturbation theory (MBPT) [15] or using the relativistic multiconfiguration Dirac-Fock (MCDF) method [16] to which quantum electrodynamic corrections should be added [16, 17]. There has been in recent years some debate concerning discrepancies between measured values and calculated values - and even differences in the various methods of calculation - of these transition energies [7, 16, 18]. It was pointed out by Kim that [16]:

> ... experimental values for ions with $46 < Z < 70$ generated in the Texas experimental tokamak (TEXT) are in excellent agreement with our (theoretically predicted) values .... It is likely that the existing energies from spectra of laser-generated plasmas in general are too high .... The data from laser-generated plasmas seem to have systematic problems that make the measured transition energies too high.

High precision experimental data of high-Z ($Z > 70$) ions from a source other than laser-produced plasmas are needed for this sequence so that either systematic errors in the measurements or deficiencies in the theoretical predictions may be recognized and addressed.

2.3 Tungsten in the Near UV

Spectroscopic diagnostics of high-temperature plasmas in the visible or near UV are often times wanted, because a wide range of instruments is available to make such measurements with high resolution (interferometry) and precision, yielding detailed access not feasible in other spectral ranges. Furthermore, visible light can be easily gathered and transported (e.g. via fiber optics and mirrors) away from the hot plasma

to even a remote spectrometer. Magnetic-dipole transitions (M1) within the ground state of ions in optically thin plasmas play an important role in present plasma diagnostics and will be similarly important for future hotter plasmas if suitable lines can be identified in highly-charged ions which can be easily measured and related to the plasma properties.

Typical visible transitions used for plasma diagnostics come from ions with the ns^2np^k ($n = 2, 3$) ground configurations [19, 20]. Figure 2.2 shows one such transition from the Si-like isoelectronic sequence ($3s^2 3p^2\ ^3P_1 - {}^3P_2$). As is the case here, along an isoelectronic sequence the wavelength of most M1 transitions is expected to vary regularly, rapidly moving to higher energy, as the atomic number Z increases. Here, as Z changes from twenty-nine to forty-two, the wavelength of this transition spans the entire visible and a portion of the near UV spectrum. This extensive variation of wavelength occurs over a corresponding ionization energy range of only 0.5 to 1.5 keV as is typical for transitions between fine structure levels of a given electron configuration. Calculations by Feldman, Indelicato, and Sugar, however, predicted the existence of one such line with unusual properties within the ground state configuration of ions in the Ti isoelectronic sequence. In particular, they predicted that the M1 transition $3d^4\ ^5D_2 - {}^5D_3$ in ions ranging from Nd^{38+} through U^{70+} (corresponding to ionization energies of 2.6 to 8.3 keV) would occur at wavelengths from 3560 to 3200 Å, respectively, that is with remarkably little variation in wavelength[2] [21]. Thus a wide variety of charge states could be studied with a given set of experimental instruments. (See Figure 2.2.) These lines certainly will be useful for the diagnostics

[2]Their predictions actually included ions of the Ti isoelectronic sequence ranging from Z = 45 (Rh^{23+}) to Z = 92 (U^{70+}), but only those in the range stated are predicted to occur in such a narrow wavelength range.

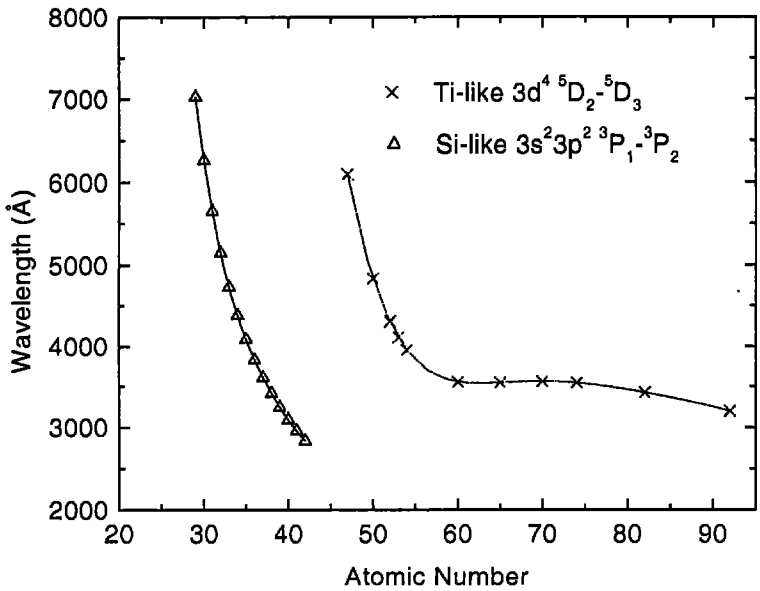

Figure 2.2: Predictions for the wavelengths of two magnetic dipole (M1) transitions. × represents calculations of the ground-state M1 transition, $3d^4\,{}^5D_2 - {}^5D_3$, in Ti-like ions[21]. Of interest is the "flat" portion in the range $Z = 60$ to $Z = 92$ through which the wavelength has a variation of only 360 Å while ionization energies vary from 2.6 to 8.3 keV, respectively. △ represents calculations of a more typical ground-state M1 transition, $3s^2 3p^2\,{}^3P_1 - {}^3P_2$, in Si-like ions[19]. Note that for a range of $\Delta Z = 14$ the wavelengths span the entire visible and a portion of the near UV region of the spectrum.

of low-density, high-temperature plasmas as, for example, they represent a simple tool for the determination of such properties as local ion temperature and bulk plasma velocities from the measurement of the Doppler widths and shifts [22, 23]. In addition to these, a measure of the electron temperature can be established by the presence or absence of this line from various elements. For instance, the presence of this transition after the introduction of Xe (Z = 54) into a tokamak plasma would suggest an average

electron temperature near 2.0 keV, whereas the identification of the same transition from W (Z = 74), a naturally occuring background in several tokamak plasmas, would indicate an electron temperature that is significantly higher, near 5.5 keV, at which the Xe transition should be absent. The real advantage in the identification of this set of lines is found in the fact that all of these lines can be measured in a single setting of a modest-resolution spectrometer. Proper experimental identification of the wavelengths and intensities of some of the lines along this sequence is necessary for positive identification of each line emitted from the plasma.

3 THE ELECTRON BEAM ION TRAP

The Electron Beam Ion Trap (EBIT) is an invaluable source for the production and study of highly-charged ions of nearly any element. The development of EBIT at Lawrence Livermore National Laboratory (LLNL) in the mid-1980's arose as a modification to the Lawrence Berkeley Laboratory (LBL) electron beam ion source (EBIS), which was designed to be used as a source of ions for injection into accelerators and storage rings. It was found upon bringing the LBL EBIS on line that it was unable to produce the desired high charge states. The root of this failure was determined to be caused by heating instabilities inherent to "long" plasmas. The major modification from an EBIS to an EBIT was the reduction of the trap length from about 1 m to about 2 cm, thereby reducing the instabilities incurred in an EBIS. The first EBIT was brought on line in 1987 under the guidance of principal investigators Mort Levine and Roscoe "Ross" Marrs. The primary goal of the original EBIT project was the production of high charge state ions of high-Z elements for precision X-ray measurements. Therefore, measurements in those first years focused on precision measurements of K-shell and L-shell X rays and in-depth studies of EBIT's ionization and trapping properties. These included studies of electron impact ionization cross-sections, dielectronic recombination, line overlap for X-ray laser pumping schemes, X-ray transition energies, and measurements of the trap properties themselves, such as trapping times and ion temperature[3] [24, 25, 26, 27]. The success of this first EBIT lead to some

[3]There are many references to the above listed work. In fact, by mid-1992 there were more than 40 publications describing measurements made with and properties of the LLNL EBITs. Today,

minor modifications and the creation of a second machine, EBIT-II, or what is now sometimes referred to simply as EBIT. The original EBIT was then reconfigured to operate at much higher electron beam energies and currents in order to achieve much higher charge states of heavy elements, and is now known as SuperEBIT. Since the development of the EBIT program at LLNL several institutes world-wide have built or are in the process of building electron beam ion traps for the study of atomic, nuclear, and surface science physics. The interest and value of these devices continues to grow throughout the world-wide physics community. The LLNL EBIT facility, however, continues to set the standards for achievement.

3.1 Working Principles and Operation

The EBIT is designed for systematic spectroscopic studies of trapped highly-charged ions. A beam of energetic electrons is used to accomplish not only the stripping of the ions of their bound electrons, but also as part of the trapping mechanism. This beam emanates near the bottom of EBIT, shown in Fig. 3.1, at the electron gun. By the application of an electric field from the focus electrode, the electrons are formed into a beam in a magnetic field free region governed by the bucking coil. They are then accelerated (to the "ionization energy") by the potential applied to the drift tube electrodes in the trapping region. The beam travels through the trapping region where it is compressed to a diameter of about 70 μm [28] by the 3 T magnetic field of a pair of superconducting Helmholtz coils. It continues to the end of its path at the collector while passing through the electric fields of the suppressor, extractor, and transition electrodes, being guided along its path by two

there are several hundred. Only a few examples are mentioned here.

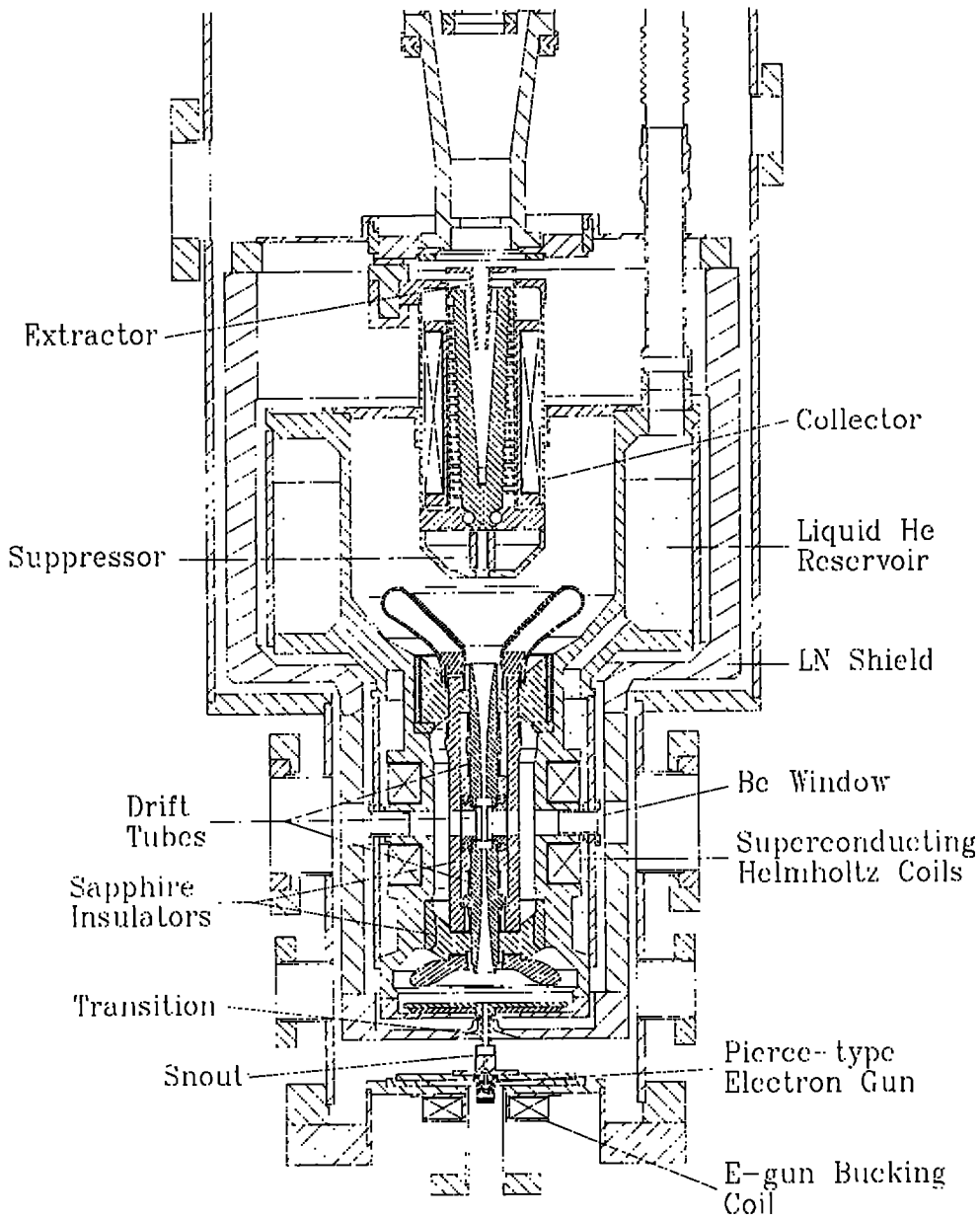

Figure 3.1: The electron beam ion trap (EBIT) highlighting its major components.

sets of external steering magnets, as well as the collector magnet. The operation of EBIT has been well studied and characterized as reported in the literature ([26, 29, 30, 31, 32, 33], and others). Proper operation is contingent upon the tuning of EBIT, which involves adjustments to the focus electrode, bucking coil, steering magnets, collector magnet, as well as the suppressor, extractor, and transition electrodes. The tuning is a function of the electron beam energy, current, and high-vacuum properties of EBIT and is an active undertaking during the experimental runs. The following sections describe some of EBIT's primary components, particularly those related to spectroscopic measurements.

3.1.1 Electron gun

The electron gun is of the Pierce type, following the design principles identified by J. R. Pierce in the 1950s for the production of electron beams. The cathode is typically operated at a potential of 6 V and draws a current of about 0.5 A from the power supply creating a cloud of electrons which surrounds the cathode. An accelerating potential on the order of 2 kV applied between the cathode and anode is used to extract the electrons from this cloud. Electron guns are characterized in terms of their perveance by $P = I/U^{3/2}$, that is, the ratio of the current (in Amperes) drawn from the gun to the three-halves power of the voltage (in Volts) applied between the gun's cathode and anode ($1\ perv \equiv 1\ A/V^{3/2}$). A greater value of the perveance results in a greater electron beam current drawn from the gun for a particular applied potential, leading to a greater electron current density.

The perveance is directly dependent upon the gun geometry and cathode material. For the type of gun used on EBIT, the cathode is made of tungsten machined into the

shape of a partial sphere. A barium dopant is embedded into the tungsten in order to reduce the work function of the cathode, thereby increasing the perveance. Early work on EBIT reported significant levels of barium from the electron gun making its way into the trap. It is for this reason that many of the first EBIT publications were studies of barium X-ray transitions. Another effect of this is that the working lifetime of an electron gun is limited to the depletion period of the barium dopant. In recent years the period of barium depletion has been found to be less problematic to the electron gun lifetime than such factors as oxygen poisoning due to accidental venting of the EBIT vacuum chamber. Some of the parameters of the electron guns used on EBITs are listed in Table 3.1.

Table 3.1: Typical electron gun parameters for the electron guns used on the LLNL EBITs. The actual values of the temperature, beam focus, and current depend on settings of EBIT power supplies and may be changed from run to run. This information is taken from an internal LLNL technical report [29].

EBIT Electron Gun Parameters	
Manufacturer	Raytheon Manufacturing Company
Cathode material	tungsten doped with barium
Operating temperature	1300° C
Perveance	0.5 μpervs
Cathode diameter	3 mm
Primary beam focus	0.36 mm radius
Maximum current	approximately 200 mA

3.1.2 Electron beam

Two general methods for the formation of a narrow, high-current-density electron beam have been thoroughly explored in EBIS experiments: 1) magnetic compression and 2) Brillouin focusing. Some of the differences in these two techniques are listed in Table 3.2. Of the two techniques, it has been found that magnetic compression leads to a more stable electron beam, but the fact that for Brillouin focusing the current density, j, goes up as the square of the magnetic field, B, makes this technique quite appealing [34].

Table 3.2: Comparison of two electron beam compression techniques: magnetic compression, which relies on the magnetic fields of a long magnet for compression, and Brillouin focusing, which requires a somewhat complicated electron beam optics design for proper implementation.

Two Electron Beam Compression Techniques	
Magnetic Compression	Brillouin Focusing
magnetically immersed electron gun	magnetically screened electron gun
high emission electron gun	normal emission electron gun
$j \propto B$	$j \propto B^2$
	electro-static compression

The LLNL EBIT design relies on the process of Brillouin focusing. Because the electron-emitting cathode is not a complete sphere, an external focus electrode must be used to compensate for the 'missing' fields to direct the electrons toward the focal point. This focusing must occur in a magnetic-field-free region. The bucking coil, which lies just beyond the focus electrode, is an electro-magnet used to compensate

for any residual magnetic fields that extend into the region near the electron gun. These fields arise mainly from the superconducting coils which surround the trap region.

One of the most important properties of EBIT related to spectroscopic measurements is the position and size of the electron beam in the trap region. Its narrow width allows spectroscopic instrumentation (both in the X-ray and optical regimes) to operate using the beam as an effective slit. While some types of spectroscopic measurements require no slit, such as those performed with a Ge or Si(Li) solid state X-ray pulse height analysis system, other high-resolution spectroscopy techniques implemented on an EBIT, such as those using flat crystals [35], focusing crystals in the von Hámos or DuMond geometry [36, 37], grating spectrometers in the EUV through visible regions, and optical prism spectrographs [38] require a narrow entrance slit. In these instruments the size of the slit is one of the limiting parameters to the spectral resolution. This is exemplified, for instance, in the ion temperature measurement of Mg^{11+} where, using a flat crystal spectrometer, a nominal resolving power of 30,000 was achieved to infer an ion temperature of 246 eV [39]. To achieve this sort of resolution it is required that the slit width be small, so that the source width remains insignificant as compared to other line broadening factors (*e.g.*, Doppler, natural linewidth) under study. It is, therefore, important to know the slit width (*i.e.*, electron beam diameter) accurately.

Knowledge of the electron beam's size is also imperative to the determination of the electron density (n_e). A higher electron density means faster ionization times and higher excitation rates. The radius of the electron beam has been measured for the low-energy EBIT (EBIT-I: 27.5 ± 2.5 μm) as well as for the high-energy

EBIT (SuperEBIT: 47.3 ± 0.7 μm) [28, 40]. These measurements were performed using a narrow slit positioned close to the electron beam and a position-sensitive X-ray detector set a distance away, as to provide a magnification of about 50×. Using this information, the electron density has been determined to be in the range $10^9 - 10^{12}$ cm^{-3} [33].

In addition to the beam size, the position of the beam with respect to the diffracting element (crystal, grating, prism) is a determining factor in the position of the image on the detector. A shift in the position of the beam in EBIT during a measurement would be reflected in a corresponding spatial shift and a possible smearing of the image of an observed spectral line. As part of the present work, systematic studies have been performed on Super-EBIT which verify that the position and size of the electron beam is, in fact, stable for ordinary operating conditions [28]. Variation of the electron beam current while retaining a constant energy showed a shift of only 1.1 μm, less than the statistical accuracy of the measurement. At constant current with varying energies, the centroid position was found to move a little more, about 6 μm. Some of this movement can be attributed to required adjustments to other Super-EBIT parameters that are necessary to keep the electron beam from hitting the walls of the vacuum chamber. Regardless, this shift is small compared to the size of the beam, being less than 20% of its full-width half-maximum (FWHM). Other significant shifts in the beam's position were observed, but only due to running EBIT in ways that were otherwise detrimental as well. For instance, by drastically changing the current in the steering magnets the beam was moved about 50 μm, but these drastic changes lead to an unstable electron beam as well.

3.2 Ions

An important feature of EBIT is its ability to trap ions of any element. Since elements occur naturally in many different phases, various methods of introducing the ions into the trap have been developed. In addition to the possibility of trapping ions that naturally occur in EBIT (either emanating from the electron gun, such as tungsten or barium, or as a natural background gas such as oxygen or nitrogen), there are two commonly used methods of introducing ions into the trap, depending on whether the natural phase of the element is gaseous or metallic. Gases are introduced into EBIT via a multiple-chamber gas injection system. The outermost chamber of the gas injector is filled to roughly 10^{-6} torr with the gas to be introduced into EBIT. A small aperture leads to another chamber, which is differentially pumped and typically made to be in the $10^{-7} - 10^{-8}$ torr range. The pressure of this chamber is precisely monitored by an ionization gauge. An electronic feedback valve system monitors the ionization gauge readout to control the flow of gas allowed into the primary chamber. A second small aperture leads from the intermediate chamber into the main vacuum chamber. This system permits only a small stream of neutral atoms or molecules directed toward the electron beam to enter EBIT, preventing unnecessary vacuum contamination. It is estimated that at a pressure of 10^{-6} torr in the primary chamber, 5×10^{12} molecules enter the vacuum chamber [29]. As the stream intersects the electron beam some atoms are ionized by the high speed electrons. Those that are not ionized may still be collisionally excited and decay as they pass through the beam, but otherwise pass through unhindered. These neutral atoms are then either frozen to the liquid He temperature wall of the vacuum vessel or are otherwise pumped out of the system. Some small amount also may add to the background pressure of EBIT.

Introduction of metals into EBIT is performed by the use of a Metal Vapor Vacuum Arc, the MeVVA [41]. The MeVVA consists primarily of 4 electrodes: anode, cathode, trigger, and focus, as shown in Fig. 3.2. A high voltage power supply raises the

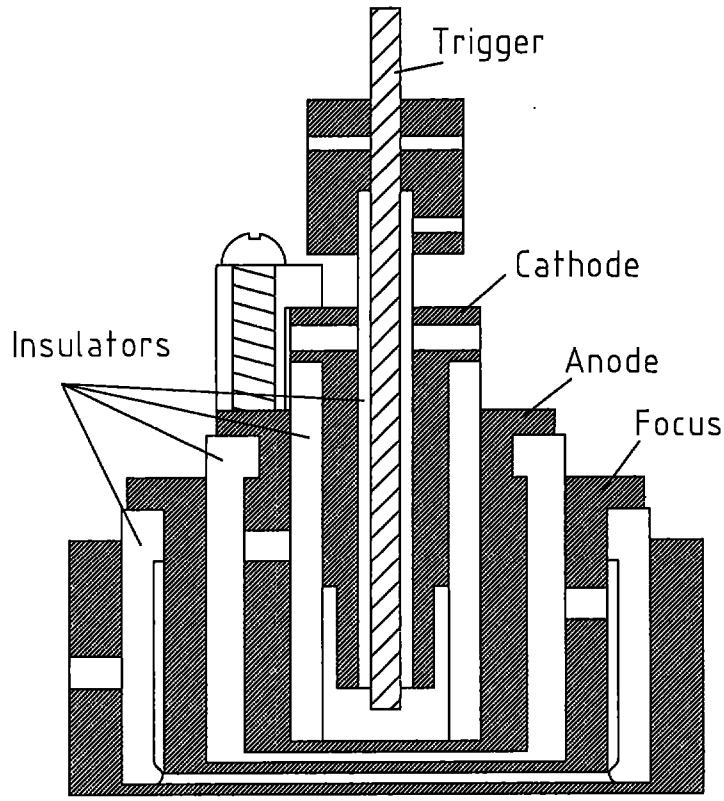

Figure 3.2: Cross-sectional view of the MeVVA. Anode, focus, and housing are stainless steel; cathode and trigger are made of the metal(s) to be injected; insulators are ceramic.

potential of the anode, cathode, and trigger to, typically, 8 kV above ground, and a second power supply introduces a potential difference of 300 - 500 V between the anode and cathode. A fast pulse of several kilovolts supplied to the trigger ejects

fast electrons into the surface of the cathode thereby vaporizing a portion of the cathode material and stripping away some of the least bound electrons. As the positive ions approach the anode they are attracted by the 8 kV potential and drawn away from the MeVVA toward the EBIT trapping region through small holes bored in the anode. Simultaneous to the firing of the MeVVA, conditions of the trap must be made suitable for the reception of the ions. The potential of the drift tube assembly is set temporarily to match that of the MeVVA voltage, at around 8 kV, so when the ions reach the trap they are nearly at rest. With too much kinetic energy, the ions would pass by the trap region; with not enough, they never arrive there. Additionally, the top drift tube's potential must be lowered to allow ions with the lowest energy into the middle trap region. Once the ions have passed the top drift tube, its potential is again raised above that of the middle drift tube for trapping to take place. The material makeup of the electrodes determines the element to be injected into the trap. While the anode and focus are composed of stainless steel, the donut-shaped cathode and wire trigger materials can be nearly any metal, although limitations sometimes occur due to the "workability" of particular metals. The roles of the trigger and cathode can be interchanged so that the material from the trigger, rather than the cathode, is injected. This allows for two different elements to be used as injector material without having to install another MeVVA, a process which typically takes five to seven hours.

3.3 Trapping physics

Ions injected either by the MeVVA or the neutral gas injection system are trapped in the central drift tube region. This section of EBIT is actually composed of a set of

three independent, cylindrical, copper electrodes called the top, middle, and bottom drift tubes. The geometry of these electrodes is critical to the ion trapping efficiency. Figure 3.3 shows a cross-sectional view of the drift tube assembly. It is the middle that has several long slots (approximately 2.5 mm × 25 mm) through which light can escape the trap region for spectroscopic observation. This section is also what defines the "trap region". The top and bottom drift tubes are normally set to a matching voltage, typically 500 V, while the middle drift tube is set at a potential 100 – 400 V lower, depending on the desired run conditions. The potential well, depicted in the figure as the axial potential, is what traps the ions along the electron beam axis. These ions must have a maximum kinetic energy less than the depth of the well. Notice the tapered ends of the top and bottom drift tubes versus the very flat middle drift tube. This geometry produces a potential profile flat in the central region and gently sloping down outside of the trap. This ensures that ions in the trap have an optimum uniform density while allowing high-energy, 'hot', ions to easily escape the trap. It also helps to steer the electron beam without disruptive potential steps.

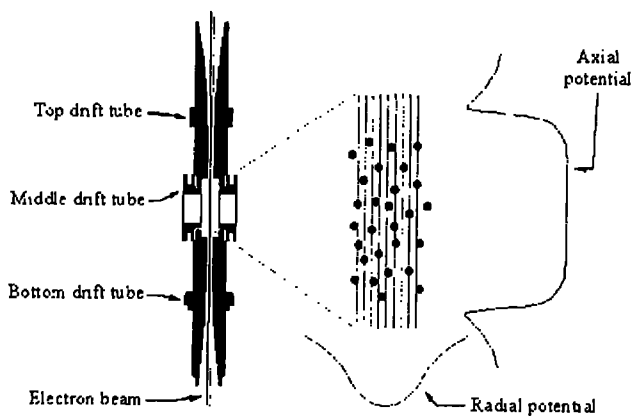

Figure 3.3: Schematic of trapping potentials of the drift tube assembly and the electron beam.

In the radial direction the ions are trapped by a combination of the space charge of the electrons in the beam, shown as the radial potential in the figure, and the magnetic field of the superconducting magnets. The potential due to the cylindrical column of the electron beam can be calculated by application of Gauss' Law. Using as a model a cylinder of uniformly distributed charge, a classical estimation of the radial space charge potential between the center and the edge of the beam, U_r can be found to be

$$U_r = 0.4792\frac{I}{\sqrt{U}} \tag{3.1}$$

where I is the beam current given in mA, U is the acceleration potential in kV, and the resultant potential is in V. A relativistic correction of about 2.5% for EBIT-II and 20% for Super-EBIT should be added [33]. Ions with a radial kinetic energy less than $q_i U_r$ (q_i is the ion charge) will remain radially trapped. The space charge also has the effect of reducing the acceleration potential of the electrons in the beam. Assuming a reference potential of zero at the middle drift tube wall, this 'deceleration' potential has been estimated to be five to eight times the radial potential. This estimation depends critically upon the compensation factor due to the presence of ions, since the accumulation of trapped ions has the opposite (neutralizing) effect on the space charge as the beam electrons.

As was stated previously, the top drift tube potential is sometimes switched to 0 V (zero volts) so as to allow ions from the MeVVA to make their way into the trap. Even when running with gases injected from the gas injector, however, it is necessary to be able to open and close the trap, even though these neutral atoms entering from the radial direction are unaffected by the trap potential. Heavy elements tend

to remain trapped longer and displace lighter ions from the trap[4], therefore, when making measurements of light gases (carbon, nitrogen, oxygen, argon, etc.) it is necessary to regularly empty and re-fill the trap. In the study of light elements, this empty/refill cycle can be as rapid as ten times per second, or faster. Figure 3.4 shows a typical timing pattern for the injection of a metallic element using the MeVVA. The cycling of the trap can be made to occur in this mode from one to tens of seconds or more, depending on the experimental needs. Trapping times of many hours have been recorded for heavy elements [42]. For gases, the timing pattern is similar to that with the MeVVA, but there is no need to switch the acceleration potential (ionization/injection) since the gases enter as neutral species.

3.4 Electronic versus Magnetic Trapping Mode

The following is a short description of an alternate method of ion trapping in an EBIT to emphasize the versatility of this device. The usual operation of EBIT comprises a continuous stream of electrons interacting with the trapped ions as described above, referred to here as the Electronic Trapping Mode. However, it is sometimes wanted to observe the photon emission of the trapped, highly charged ions without the continuous ionization and re-population affected by the electron beam. This is important for such studies as the measurement the lifetime of an electron occupying a particular level or the observation of charge exchange between two elements in the

[4]Since ion collisions tend to equally distribute the energy of the ions, heavy ions have a lower maximum kinetic energy than light ions in the same potential well. It is, therefore, more likely for a light ion to escape from the trap region. This means, it is easier to trap heavy ions, and heavy ion background gases will displace light ions in the trap. Also, eqU results in a higher potential wall for more highly charged ions.

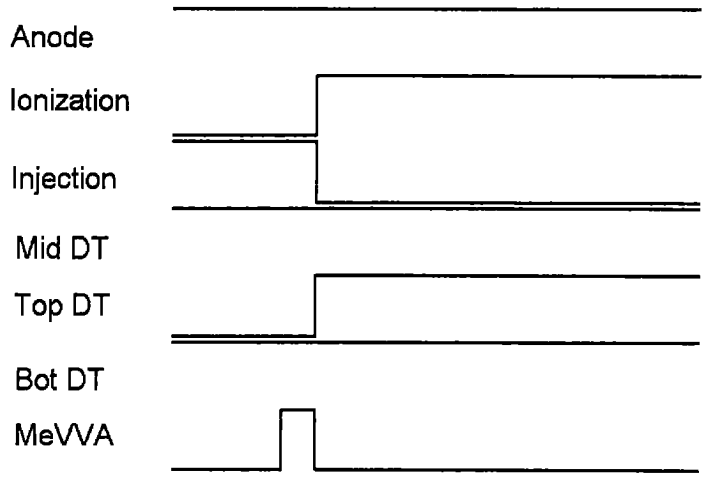

Figure 3.4: Representation of a typical EBIT timing pattern for injection with the Metal Vapor Vacuum Arc (MeVVA). The timing pattern sets each power supply as either ON or OFF; the applied voltages are controlled elsewhere. Notice that in the case shown, the anode and middle drift tube voltages are always on. There are cases in which this may not be true. At the instant of the MeVVA trigger the acceleration potential is set by the injection voltage and the top drift tube is turned off allowing ions to escape the trap axially. Just after the trigger, the trap is closed (ions are trapped) and the acceleration potential is set to the desired ionization energy.

trap. The Magnetic Trapping Mode has been developed for such cases [43]. In this mode EBIT is initially operated in the standard way to trap the ions and create the wanted charge balance of ionic states. The electron beam is then switched off by one or several means (i.e. turning off the anode power supply, reducing the ionization potential of the electron beam to zero, setting the focus potential to a very high value) but without switching off the top drift tube electrode, so that the ions remain trapped in the axial direction by the potential well of the three electrodes. Even though the ions are no longer bound in the radial direction by the space charge of the electron

beam, they are still contained by the strong magnetic field of the superconducting Helmholtz coils. Trapping times in the Magnetic Trapping Mode have been observed to be on the order of seconds to tens of seconds. It has been shown that with the electron beam turned off, photons are produced by electron capture from ambient neutrals in the trap. All of the measurements reported in this dissertation have been performed using the more standard mode, the Electronic Trapping Mode, and are dominated by electron impact excitation from the beam electrons.

3.5 Spectroscopic observation

EBIT has six ports encircling the trap through which spectroscopic measurements can be made. The orientation of these ports is such that the four largest ports are offset by 90° from each other (NE, NW, SW, and SE), with the two remaining ports being at the N and S positions, 45° from their neighbors. Inside the vacuum chamber each of the ports is identical, consisting of a 2.5 mm × 25 mm aperture in the middle drift tube, a 4.0 mm × 26 mm aperture in the drift tube shield, a 16 mm cylindrical slot in the liquid-He dewar, a 27 mm cylindrical slot in the liquid N_2 dewar, followed by the aperture in the vacuum hull. Four of the observation ports are fitted with $4\frac{1}{2}''$ conflat flanges while the two others are fitted with $2\frac{3}{4}''$ conflat flanges. The limiting aperture of such a system is important when knowledge of the subtended solid angle of light is needed. A measure of this is the f-number, defined by

$$f/\# = \frac{distance\ from\ source}{size\ of\ aperture}.$$

Since the apertures are all collinear, this limiting value can be measured from a point at the center of the trap. For a complete treatment of the solid angle one should take into consideration the volume of the ions in the trap. Table 3.3 shows the relative

apertures ($f/\#$) of the components inside of EBIT. It is the hole in the liquid He dewar that sets the limit of light collection in the vertical direction (along the direction of the beam) with $f/4.4$, and the slot of the middle drift tube, with $f/5.6$, that acts as the light stop in the perpendicular direction.

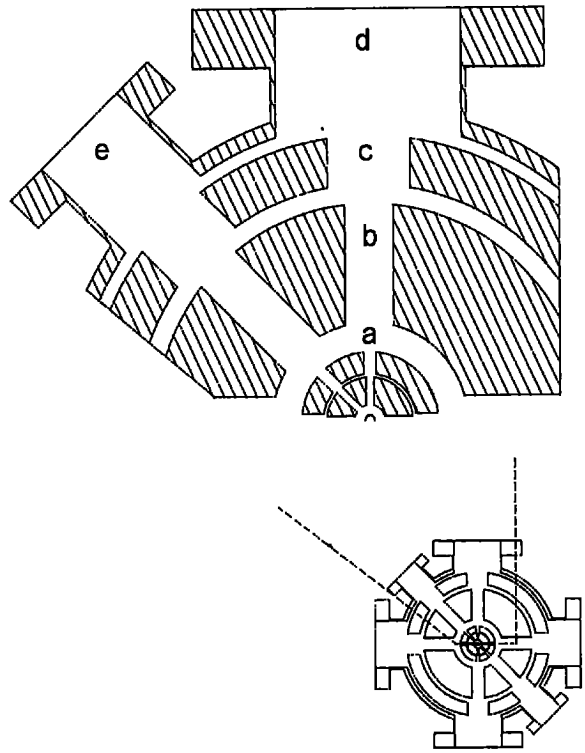

Figure 3.5: Horizontal cross-sectional view through the center of the middle drift tube in EBIT. The expanded region shows the apertures created by the various components inside the vacuum chamber. The alphabetic labels point out the a) middle drift tube and drift tube shield, b) liquid helium dewar, c) liquid nitrogen dewar, d) $4\frac{1}{2}''$ flange, and e) $2\frac{3}{4}''$ flange. The $f/\#$ and dimensions of each of the apertures is listed in Table 3.3.

The arrangement of the six sets of collinear slots and ports allows for a multitude of instrumentation to simultaneously look into EBIT, limited only by the physical

Table 3.3: Sizes of and distances to apertures inside EBIT. The ratio of the distance to the size determines the $f/\#$. The largest $f/\#$ is the most limiting relative aperture. This limit is made by the slot in the liquid He dewar in the vertical direction, that is, parallel to the beam axis, and by the middle drift tube in the horizontal direction. All distances and sizes are in units of mm.

Relative Apertures			
	distance from source	size of aperture	$f/\#$
Middle DT width	14	2.5	5.6
Middle DT length	14	25	0.6
DT shield width	22	4.0	5.5
DT shield length	22	26	0.8
Liquid He dewar (round)	70	16	4.4
Liquid N dewar (round)	90	27	3.3
Vessel flange: $2\frac{3}{4}''$ (round)	133	35	3.8
Vessel flange: $4\frac{1}{2}''$ (round)	133	60	2.2

size of the spectrometers. Current available instrumentation consists of a variety of crystal X-ray spectrometers (i.e. flat crystal, von Hàmos, DuMond), solid state Ge and Si(Li) detectors, grazing-incidence grating spectrometers, high-efficiency quartz-grating transmission spectrometers, a 1-m normal incidence grating spectrometer, and an optical prism spectrometer plus a variety of other spectroscopic instrumentation. This large selection of high quality optical instrumentation permits the study of photon emission from trapped ions continuously for photon energies near 1 eV (infrared) to many keV (hard X ray).

4 SPECTROSCOPIC INSTRUMENTATION

In its simplest description a neutral atom consists of a nucleus comprised of combinations of protons and neutrons surrounded by a number electrons equal to the number of protons. These electrons are bound to exist in certain quantized states, or energy levels, while transitions of electrons between energy levels is governed by the absorption or emission of a photon with an energy equal to the energy difference of the two levels. These atomic transitions can range in energies from about 100 keV to much less than 1 eV corresponding to wavelengths of emitted photons in the range of about 0.1 to longer than 15000 Å. There is no single spectrometer able to make precise measurements throughout this entire range. In fact the spectrum is subdivided into regions which are mainly defined by the type of instrumentation used to probe the regions. Loosely speaking the ranges are (in units of Å) infrared (IR: >8000), visible (4000 - 8000), near ultraviolet (UV: 2000 - 4000), vacuum ultraviolet (VUV: 200 2000), extreme ultraviolet (EUV or XUV: 10 - 500), and X ray (<1 - 50). Though these ranges are sometimes overlapping and somewhat arbitrary, they serve as a descriptive guideline. The distinction used in this work between the three shortest wavelength groups is that photons dispersed with a crystal are X rays, those dispersed using grazing incidence gratings, EUV, and those dispersed with a normal incidence grating, VUV. The term soft X ray is sometimes used to describe the region of overlap between X ray and EUV where either crystal or grating spectrometers can be implemented. The measurements in this work fall in the category of either EUV or UV.

4.1 Extreme Ultraviolet Spectroscopy on EBIT

4.1.1 EUV Spectroscopy Basics

The basic methods for spectroscopy using concave reflection gratings were developed by Prof. H. A. Rowland in the latter half of the 19th century. He found that if a concave grating is placed tangentially to a circle with a diameter equal to the radius of curvature of the grating, a source placed somewhere along this circle produces spectral images focused also on the circle. This circle, called the Rowland circle, forms the basis of nearly all vacuum grating-spectrometer designs [44, 45]. His further research was to conclude that the rulings should be so spaced on the concave surface as to be equidistant on the chord of the circular arc. Many people since then have contributed to the full development of the theory of concave gratings with two particularly complete descriptions coming from Beutler[5] and Namioka [46, 47]. Two important results that come out of the theory of concave gratings (refer to Appendix B for details) are *the grating equation* (Eq. B.20),

$$m\lambda = d\left(1 - \frac{z^2}{2r^2}\right)(\sin\alpha + \sin\beta)$$

and the parameterized equations defining the Rowland circle (Eq. B.21),

$$r = R\cos\alpha \text{ and } r' = R\cos\beta$$

where λ is the wavelength of light of interest, m is an integer ($m = 1, 2, 3, \cdots$), d is the distance between grooves, α and β are the angles of incidence and diffraction,

[5] It was pointed out by Namioka in 1959 that Beutler's treatment of the characteristic function, or path function, is incorrect making many of his results wrong. However, these errors appear only in high order terms of the path function not discussed here. His treatment is correct as a first order approximation.

respectively, r and r' are cylindrical coordinates describing the position of the source and focus position, respectively, z is the vertical distance of the source point from the xy-plane, and R is the radius of curvature of the concave grating. Using eq. B.20 the dispersion and resolving power of the grating can be calculated, and from eq. B.21 the geometry of the spectrometer is defined. Much of the theory of concave gratings is devoted to the understanding and attempted correction of many orders of aberration such as coma and astigmatism. However, inherent physical properties prohibit the perfect focusing of a spectral image obtained using a spherical grating.

4.1.2 The Flat Field Gratings

The measurements to be discussed in Chapters 5 and 6 were made using an EUV spectrometer only recently implemented at the LLNL-EBIT facility. This spectrometer is designed to use either of two gratings having the property of producing spectra on a flat image plane. The gratings are manufactured using a mechanical ruling technique that allows for variable distance between grooves across the surface of the concave grating. A ruling machine capable of etching these gratings was designed by Harada and Kita in early 1970's [48] and in the years since these gratings have become commercially available. A set of equations which correct for several orders of aberration are analytically solved to provide a result that can be optimized for the desired spectroscopic operating parameters such as the average groove spacing, the radius of curvature of the grating, and the angle of incidence. The result is a single equation for the variable groove density which can be programmed into the ruling machine and the grating precisely manufactured. See Appendix B for details of the analysis and comparisons to uniformly line spaced gratings.

One of the restrictions of traditional EUV grating spectroscopy is that the entrance slit, grating, and detector should be aligned on the cylindrical surface defined by the radius of curvature of the grating, known as the Rowland circle, so that the photons strike the grating and the detector at grazing incidence (see, for instance, [49]). For spectrometers using film to record the spectra this poses no technical problems provided an adequate method for mounting the film on this cylinder is implemented. However, film presents other problems at EBIT such as its insufficient sensitivity for single photon counting (as compared to other detectors, to be discussed below) and the requirement of additional steps to develop the film. The low photon flux of EBIT requires detectors which are sensitive to individual photons, i.e., photodiodes, multichannel plates (MCPs), and charge coupled devices (CCDs). Whereas photodiodes may be precisely aligned to the Rowland circle, they view only a small area, provide no spatial information, and must be either scanned over a region of interest, or used as an array of many in order to obtain a spectroscopic image. MCPs and CCDs, while gaining spatial resolution, are typically planar and can never be situated so that all points reside on the Rowland circle. It is common when using MCPs or CCDs (or any other flat detectors) with a Rowland circle type spectrometer that the detector be placed tangentially to the circle so as to be in approximate alignment throughout the image. Since the spectral lines are no longer in perfect focus except at either one or two points, this technique degrades the overall resolving power. Even though some of the detrimental geometric effects may be minimized, the efficiency of these detectors is still diminished at grazing incidence [50]. Another restriction resulting from the cylindrical focal plane of a uniformly spaced grooves grating is that translating the detector to access different wavelength ranges requires moving the detector along a

circular path. This is usually achievable by mechanical means such as detector tracks or arms governed by precisely machined cams, but is, at the very least, another consideration in the spectrometer design. An example of this type of spectrometer is discussed in [49].

Because of flexibility in the ruling parameters of a variable line spaced (VLS) grating, it is possible to define a set of equations which results in a portion of the focus region of the grating being along a flat plane, rather than the Rowland circle. Not only does this mean that the entire surface of the detector can be aligned on the focal plane, but that a change of wavelength regions simply requires a linear translation of the detector. Additionally, since the photons strike the detector surface at nearly normal incidence, the detector's efficiency is increased. The fact that these gratings are mechanically ruled rather than holographically etched adds the further advantage that the gratings can be blazed; that is, the grooves can be optimally angled to enhance a desired wavelength region.

Two VLS gratings have been used at EBIT to study the EUV region: a 1200 line/mm and a 2400 line/mm grating[6]. The gratings are similar in that they are manufactured to have the same object and image distances, and they have the same physical dimensions; they can, therefore, be interchanged within the same spectrometer by making only minor adjustments. Other than the average line spacings, the main difference between the gratings is the spectral range over which each is designed to be used.

[6]The line densities of 1200 and 2400 line/mm are actually the line densities at the center of the grating. The actual line density is given by the formula $n = \frac{1}{d_0}\left(1 + \frac{2b_2}{R}w_\theta + \frac{3b_3}{R^2}w_\theta^2 + \frac{4b_4}{R^3}w_\theta^3 + \cdots\right)$ as described in Appendix B where d_0 is the nominal line spacing, R is the radius of curvature of the grating, w_θ is related to the horizontal distance from the center of the grating, and the b_i are the adjustable ruling parameters.

The 1200 has an operational range of approximately 30 – 400 Å and the 2400 has a range of 10 – 100 Å. Other properties of the gratings are listed Table 4.1.

Table 4.1: Properties of the two gratings used in the EUV spectrometer on EBIT where n_0 is the nominal groove density, R is the radius of curvature of the grating blank, λ_{blaze} is the blaze wavelength of the grating grooves, α is the required angle of incidence, and I is the focal distance of the image plane from the grating center. This data is taken from *Hitachi Diffraction Gratings* technical information sheet.

Grating Properties						
n_0	R	λ_{blaze}	Dimensions	α	I	Range
g/mm	m	Å	h × w × t	degrees	mm	Å
1200	5.649	100	30 × 50 × 10	87.0	235	50 ∼ 300
2400	15.920	15	30 × 50 × 10	88.7	235	10 ∼ 100

There is one notable difference in the spectra produced by each grating: the 1200 reproduces each spectral line in multiple orders throughout its range, whereas the 2400 produces only first order lines. Experience has shown that there are advantages and disadvantages to the use of each grating. The presence of multiple orders in the 1200 grating makes calibration of the entire spectral range possible using only a few very well known transitions. For instance, the $K_{\alpha 1}$ line ($1s^2\ ^1S_0 - 1s2p\ ^1P_1$) in He-like N at 28.7870 Å has been identified in orders ranging from 2^{nd} through 12^{th}, albeit at varying intensities. A similar result occurs for the $Ly_{\alpha 1}$ line in H-like N at 24.7792 Å. Figure 4.1 shows two examples of spectra taken on EBIT with the 1200 line/mm. The top spectrum is of nitrogen gas injection; the bottom spectrum is from W injection at an electron beam energy E_{beam} = 3.70 keV. The strongest

line in the N spectrum is the He-like $K_{\alpha 1}$ shown in orders 2nd through 7th. These precisely known lines are used to regularly calibrate the spectrometer prior to and

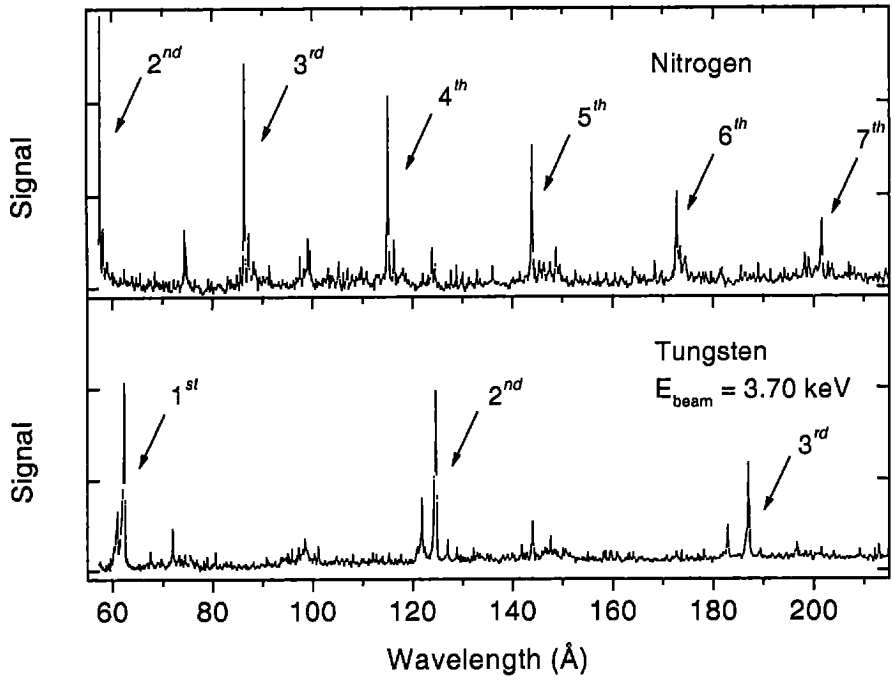

Figure 4.1: Spectra taken with the 1200 l/mm grating. The top spectrum was taken during N_2 gas injection and is used for calibration. The line marked in 6 spectral orders is from the He-like $K_{\alpha 1}$ transition. The bottom spectrum was taken during W injection with an electron beam energy of E_{beam} = 3.70 keV. This energy optimizes the Cu-like charge state of W in the EUV.

throughout measurements. The W, dominated by the Cu-like charge state, exhibits several neighboring transitions around 62 Å, for which the resolution improves with increasing spectral order. However, due to the complexity of typical EUV spectra, the presence of multiple orders of several lines at the same time is sometimes a hindrance,as shown in Fig. 4.2. For example, line groups found in first order near 45 Å blend in the third order with second order 65 Å lines. resulting in sometimes

confusing and blended spectra, rather than the desired improved resolution. Contrary to this, the 2400 grating produces very "clean" spectra and there is no ambiguity

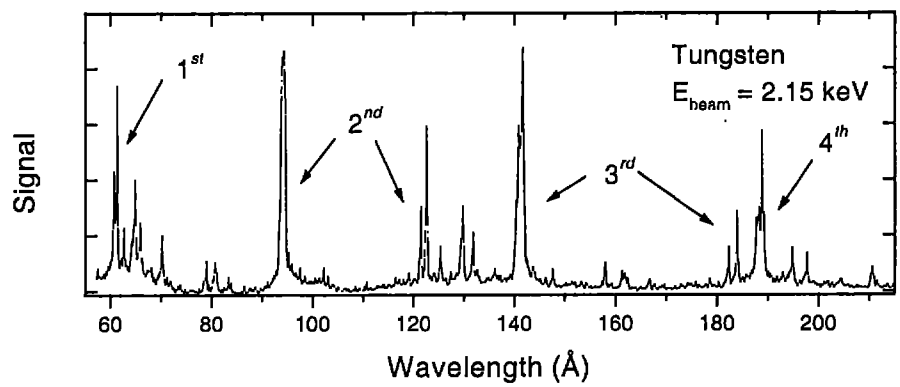

Figure 4.2: Tungsten spectrum taken with the 1200 l/mm grating at a lower energy than in Fig. 4.1. The overlapping spectral lines from multiple orders inhibits better spectral resolution.

to the assignment of a spectral line's wavelength. The drawback here is that many more individual precisely known transitions are needed to adequately calibrate the entire spectral range. This difference between the gratings has also been noted by other groups using the same type of grating [51]. As a result, for the best possible spectral resolution, all of the EUV measurements reported here were taken with the 2400 grating. A description of the calibration procedure is provided in Chap. 5.

4.1.3 The Spectrometer Housing

To a certain extent it is true that a spectrometer is made up of just a properly positioned grating and detector, the rest are just bells and whistles. However, it is the 'bells and whistles' which make the spectrometer easier to use. The EUV flat-field spectrometer housing (hereafter this shall be referred to as the FFS) is designed

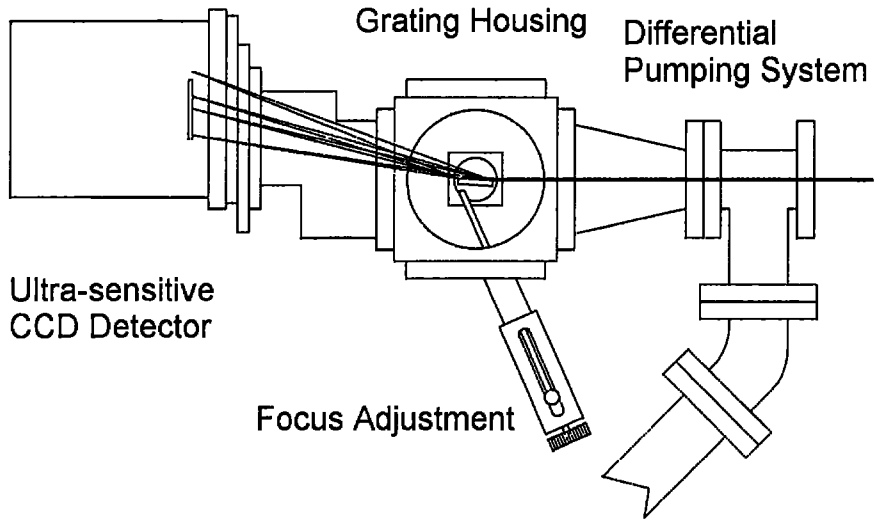

Figure 4.3: The Flat Field Spectrometer system. In this configuration, the EBIT port would be to the right of the page. The differential pumping system prevents the relatively high pressure of the spectrometer housing ($\simeq 10^{-7}$ torr) from contaminating the ultra-high vacuum of the EBIT drift tube region ($< 10^{-10}$ torr). The focus adjustment rotates the grating, and therefore, the angle of incidence, to align the focal plane of the grating with the CCD detector.

around a $6.9 \times 6.9 \times 6.9$ in^3 aluminum cube with six ports and appropriate vacuum flanges (see Fig. 4.3) [52]. Contained in the cube is the grating mount which sits atop a rotatable stage, which, in turn, is fastened upon a linear translation stage. These stages are used to align the grating so that its center corresponds to the center of the cube at an incident angle appropriate for whichever grating is to be used. A vacuum feed-through – added after initial results were unsatisfactory – allows the incident angle to be adjusted while the spectrometer is under vacuum for fine tuning. This modification more than doubled the resolving power achieved with this spectrometer. To the aft of the cube attaches an angled adapter, matched to angle of direct reflection

from the grating, which positions the detector to observe the light diffracted by the grating. The adapter has two adjustable features. The first is a set of slotted bolt holes which allows two flat plates to slide against each other in order to set the detector to the desired wavelength range prior to pumping on the chamber. The second is a slotted bolt circle which permits the rotation of the detector approximately $\pm 2^{\circ}$ about it central axis[7].

A major concern when working with EBIT, or any highly charged ion experiment, is that the pressure in the trapping region must be kept as low as possible to avoid both detrimental charge exchange with background gas — which would lower the average charge state of ions in the trap - - and the production of background spectral lines -- which could interfere with the interpretation of the experimental data. The Electron Beam Ion Trap was originally designed for spectroscopic measurements of X-ray transitions of trapped, highly-charged ions. The observation ports were, therefore, fitted with beryllium windows which were only penetrable by photons with energies on the order of 1.5 keV and higher (wavelengths shorter than 10 Å). These windows served the purpose of isolating the EBIT vacuum from the spectrometers, some of which are operated with atmospheric pressure helium, while allowing the study of X-ray phenomena. Somewhat later, quartz windows were substituted for the beryllium in order to investigate optical transitions from highly-charged ions. Because the energy of a photon in the EUV is in the range of 25 to 1200 eV, a range of energy readily absorbed by any type of solid barrier, special considerations were required

[7]The rotation is necessary since the CCD chip is not perfectly aligned within the detector housing. This slight offset, left uncorrected, causes an apparent broadening of the spectral lines. The rotation can be adjusted during the initial focusing procedure with the chamber under vacuum and the detector cooled.

for the implementation of an EUV spectrometer. The main portion of the FFS is evacuated using a 170 liter/s turbo pump and achieves a base pressure on the order of 10^{-7} torr, at least 4 orders of magnitude higher than the trapping region pressure. Between the main FFS and EBIT chambers is a differential pumping system consisting of a 6″ "T" having slotted apertures on the opposite open ends and a 30 liter/s turbo pump on the mid-section. This pumping technique reduces the amount of gas flowing into EBIT from the FFS by more than an order of magnitude. In fact, upon opening the FFS to EBIT, no change in the EBIT chamber pressure is measured.

4.2 Transmission Spectrometer

High-precision spectroscopy is most easily performed for light in the visible and near UV where quartz lenses and mirrors are easily used. However, this is also a region where investigations of middle charge state ions is somewhat lacking. Typical transitions from middle charge state ions more often exist in the EUV or X-ray region reducing the emphasis on measurements in the visible and near UV. There is a need for the development of instrumentation to study transitions in the visible and near UV and the identification of transitions relative to the plasma diagnostics. For this purpose a high-efficiency, high-precision transmission grating spectrometer (TGS) has been developed at EBIT.

The TGS uses a 6″ diameter, 0.250″ thick quartz grating as its dispersive element. This grating was manufactured using special techniques developed at LLNL[8] [53].

[8]The gratings were developed as high-efficiency transmission gratings for frequency-tripled 3ω radiation in solid state UV lasers at 351 nm. At this wavelength these grating have been shown to exhibit a diffraction efficiency of 94% in order $m = 1$

The flat, quartz plate has rectangular grooves spaced 350 nm apart (2857 l/mm) with a duty-cycle of 0.5 (groove width = one-half groove spacing) and is optimized for light at 3800 Å by fixing the groove profile to an optimal shape and depth. In addition to the grating, the spectrometer is composed of a collection lens, a focusing lens, and a CCD detector system all of which are mounted on a portable (light-weight aluminum) optical table and shielded from external light by light-tight walls and lid. Figure 4.4 shows a diagram of the TGS as it is set-up on EBIT. The 130 mm diameter, $f/4.6$ collection lens is positioned so that the focal point coincides with the trapped ion cloud. As such, the light passing from the ion cloud through the lens comes

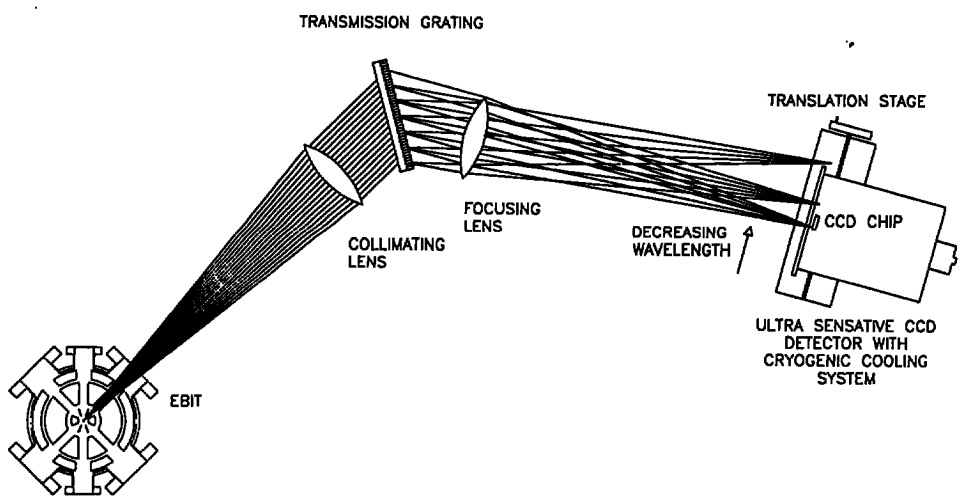

Figure 4.4: Layout of components for the transmission grating spectrometer (TGS) system. The optical components and detector are housed in a light-tight box. The EBIT vacuum is sealed with a $4\frac{1}{2}''$ quartz window and a cylindrical tube connects the EBIT port to the box.

out as parallel light. The transmission grating is set to collect as much of the light cylinder as possible at an angle, α, appropriate for whatever wavelength range of light

is to be studied as determined by the grating equation Eq. B.20

$$\frac{m\lambda}{d} = \left(1 - \frac{z^2}{2r^2}\right)(\sin\alpha + \sin\beta).$$

α is typically set to 30° to match the Littrow angle at which the reflective diffraction into first order coincides with incident light of 3500 Å. The dispersive angle, β, is still a free parameter for wavelength selection. Since the incoming light to the grating is parallel, $r \to \infty$, and the grating equation can be re-written as (for $m = 1$)

$$\frac{\lambda}{3500} = (\frac{1}{2} + \sin\beta)$$

with λ given in Å. Therefore, light at a wavelength of 3600 Å is transmitted at an angle of 31.9°. The focusing lens, identical to the collection lens, is positioned to intercept the transmitted light, which it then focuses at the surface of the CCD detector. The CCD detector is mounted on a linear translation stage with $2\frac{1}{2}''$ of allowable travel along the dispersive direction. This system can be set up to optimize a single wavelength, but also provides access to a band of light approximately 200 Å on either side of this central wavelength.

4.3 CCD Detectors

The recording of spectra with the FFS and the TGS is achieved with a cryogenically-cooled, thinned, back-illuminated charge-coupled-device (CCD). A typical CCD is made of a silicon substrate and polysilicon gate structure separated by a silicon dioxide layer. Photons of sufficient energy produce electron-hole (e-h) pairs in the silicon substrate and a positive electrical potential applied to the gate structure creates a depletion region where the electronic charge can be stored. However, e-h pairs can be created by sources other than light as well. For instance, thermal agitation can also be

a source for e-h pair production. Since the rate of thermal agitation pair production – also called dark current – is temperature dependent, this source of charge can be controlled by cooling the CCD. In addition to thermal agitation, cosmic radiation, hard X rays, and charged particle impact can create unwanted electronic charge. After production, charge accumulates in the potential wells until the readout procedure is initiated. The total charge in the well at any time after initializing (clearing) the CCD is proportional to the product of the exposure time and the light intensity plus any unavoidable dark current. The potential well will collect all charges until it is filled; typical capacities are on the order of several million electrons.

The gate structure is comprised of a 2-dimensional array of several hundreds, or even thousands, of columns and rows. Each gate is equivelant to one picture element, or pixel. Once the charge is collected in the potential well and the readout procedure initiated, the charge must be transfered to an amplifier. This charge transfer is achieved by the application of appropriate potentials to the gates. The charges are pushed across the CCD from one potential well to the next until they reach the final column where they are read out into the output amplifier. Figure 4.5 shows a diagram of the step by step process. Charge transfer can occur in this way for thousands of times without significant loss of charge.

A technique used to increase the signal to noise ratio of the CCD output is called binning. Binning means to combine electronic charge from two or more neighboring pixels into a single, larger potential well at the expense of spatial resolution. The advantage of binning is that all of the signal can be collected while suppressing readout noise and, to some extent, dark current accumulation. Additionally, the size of the binary data file is reduced by the binning factor. For example, unbinned CCD data

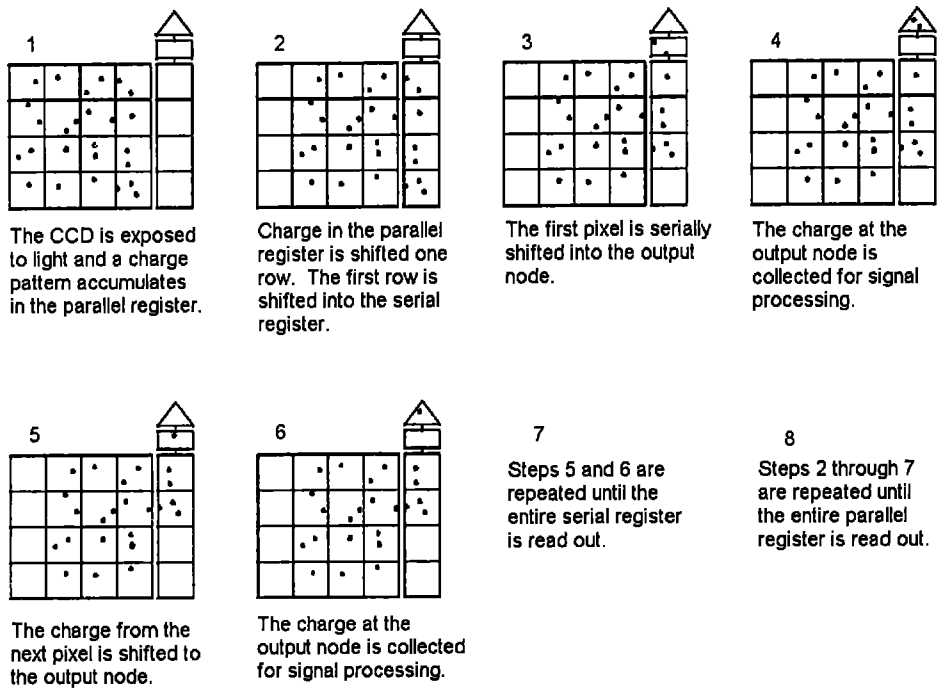

Figure 4.5: CCD readout sequence.

files are typically 2 MB. A factor of 4 binning in the non-dispersive direction yields files which only take up 512 kB of disk space. Since with spectroscopic data there is critical spatial information in the dispersive direction, it is in the non-dispersive direction that any binning should be done. Because binning has the effect of reducing the number of pixels to be processed by the binning factor, the read out speed is also increased by a similar factor.

In a standard CCD the photons must travel through the polysilicon gate structure and the silicon dioxide insulation layer to reach the active silicon layer. Silicon and oxygen have significant attenuation to photons in the EUV range, therefore photons

in this range are absorbed before reaching the active layer. There are two methods used to circumvent this problem that permit the use of CCDs in the EUV range. The first consists of applying a phosphorus coating to the surface of the CCD to convert the EUV photons to visible light which is detectable by the device. Since the light from the phosphor is emitted in 4π sr solid angle, only the portion of converted light directed toward the active layer at an angle less than the angle of absolute reflection will reach the detector, thereby reducing the collection efficiency of such a detector [54]. Additionally, due to the separation of the phosphor and the active region there is a blurring effect of the emitted photons and the spatial resolution is reduced [50].

The second method to make CCDs useful in the EUV region is to use a thinned CCD in which the silicon substrate, the back of the CCD, is etched to a thickness of only 10 to 25 μm and the CCD is illuminated from the back — these are called, appropriately, thinned, backside-illuminated CCDs. The absorption of incident photons before reaching the active layer is reduced since they need only pass through a natural silicon oxide layer and a thin contamination layer of carbon, each less than 100 Å thick [55]. The CCDs used on the FFS and TGS are of this type. Other technical data is given in Table 4.2.

For complete interpretation of spectroscopic data taken with a CCD it is important to understand the detection efficiency in the energy range being investigated. This is discussed in detail in Chap. 5 in which the intensity of spectral lines is of interest.

A source of unavoidable background is present in all of our CCD data. Each integrated image shows intense peaks that are not attributable to directed stray light

Table 4.2: Technical details of the thinned, backside-illuminated CCD. Technical data comes from Photometrics certificate of calibration.

Grating Properties	
Camera Manufacturer	Photometrics
Chip Manufacturer	Tektronix
Chip Type	TK1024 Grade 1
Format	1024 × 1024 pixel
Pixel Size	24μm × 24μm
Physical Size	1″ × 1″
Measured Gain	1.45 e^-/count
Electronics Unit	CE200A
Temperature Range	-90 - -120°C
Dark Current	0.178 e^-/pixel/hour

or thermal noise. High energy particles, known as cosmic rays[9], constantly bombard the earth's surface. Whenever one strikes the CCD detector it leaves as its signature an intense spike of hundreds or thousands of counts in a single or several neighboring pixels. Due to extended integration times, usually on the order of 20 minutes per spectrum, and the fact that the CCD has no energy-gating capabilities each image acquires a significant number of these spikes. While they are a source of random noise, their detrimental effects can be minimized by careful software analysis after

[9]The term "cosmic rays" is used here in a broad sense, including secondary particle emission evolving from primary cosmic ray decay or upper atmosphere interactions.

the data is stored. Appendix C is a description of such a filtering program used in this work for the FFS data analysis.

5 TUNGSTEN IN THE EUV

EBIT is an ideal device for making measurements of a single element over a series of energies for the definite association of each line to its ionization energy and, therefore, charge state. Tungsten is of interest for its intrinsic relationship to fusion plasmas, since many components of present day and planned future generation tokamaks are made of tungsten due to its physical properties. As higher temperatures are achieved, and tokamak systems become more and more sophisticated, the ability to predict plasma properties becomes more and more imperative. It is important, then, to have accurate data on which to base these predictions. Since W is and will be inherently in the plasma, it is expected that a significant fraction of energy may be exhausted via W radiation. The intermediate charge states of W from Rb-like W^{37+} to Cu-like W^{45+} are some of the most prominent in plasmas with ion temperatures of a few keV. These ions radiate a significant portion of their spectra in the EUV from 40 - 85 Å. Precise measurements have been made of W through these charge states in the EUV using the FFS. Stepping the energy of the electron beam in EBIT from 1.7 to 3.0 keV has resulted in positive charge state identifications of more than sixty of these lines with the associated transition identified for most of these.

5.1 Theoretical predictions

While many measurements of particular lines and theoretical predictions of transitions from intermediate charge state ions have been reported in the last twenty years,

by far the most complete compilation of the wavelengths and intensities of these lines comes from the theoretical predictions of Fournier found in Ref. [13], where transition wavelengths were derived from *ab initio* atomic structure calculations. These calculations were performed with the graphical angular momentum coupling code ANGLAR and the fully relativistic parametric potential code RELAC. Of particular interest to this work are the predictions, therein, of the wavelengths and intensities of Rb-like W^{37+} – Cu-like W^{45+} in the spectral range of 40 – 85 Å. Fournier's predictions for ions of these charge states are displayed in Fig. 5.1. These lines are convolved with a Gaussian function with a FWHM the same as the lines measured with the FFS. The peak of the Gaussian is proportional to the calculated collisional-radiative line intensity for each transition computed for a plasma with an electron temperature 60% of the ionization potential for each ion. All of the spectra are shown to the same intensity scale with the exception of the Zn- and Ge-like which are more suppressed than the others.

Most of the strongest spectral lines can be sorted into two groups, those near 45 Å and those near 60 Å. The group near 45 Å is composed of transitions that are typically $l = 2 - 1$ and $\Delta J = 1$, while those in the 60 Å region tend to be of the types $l = 1 - 1$ or $l = 1 - 0$ with $\Delta J = 1$. Several similar transitions can be traced along the changing charge states as the core of electrons slowly changes. (For these purposes, the core is the group of the electrons not directly involved in the transition.) For instance, the core of the Cu-like charge state is a closed $n = 3$ shell, and the transition $(4p-)^1{}_{J=\frac{1}{2}} - (4d-)^1{}_{J=\frac{3}{2}}$ has a predicted wavelength of 49.1651 Å – note that this is not a transition to the ground state. Adding another electron to the core produces the Zn-like charge state and a similar transition $(4p-)^1{}_{J=1} - (4d-)^1{}_{J=2}$

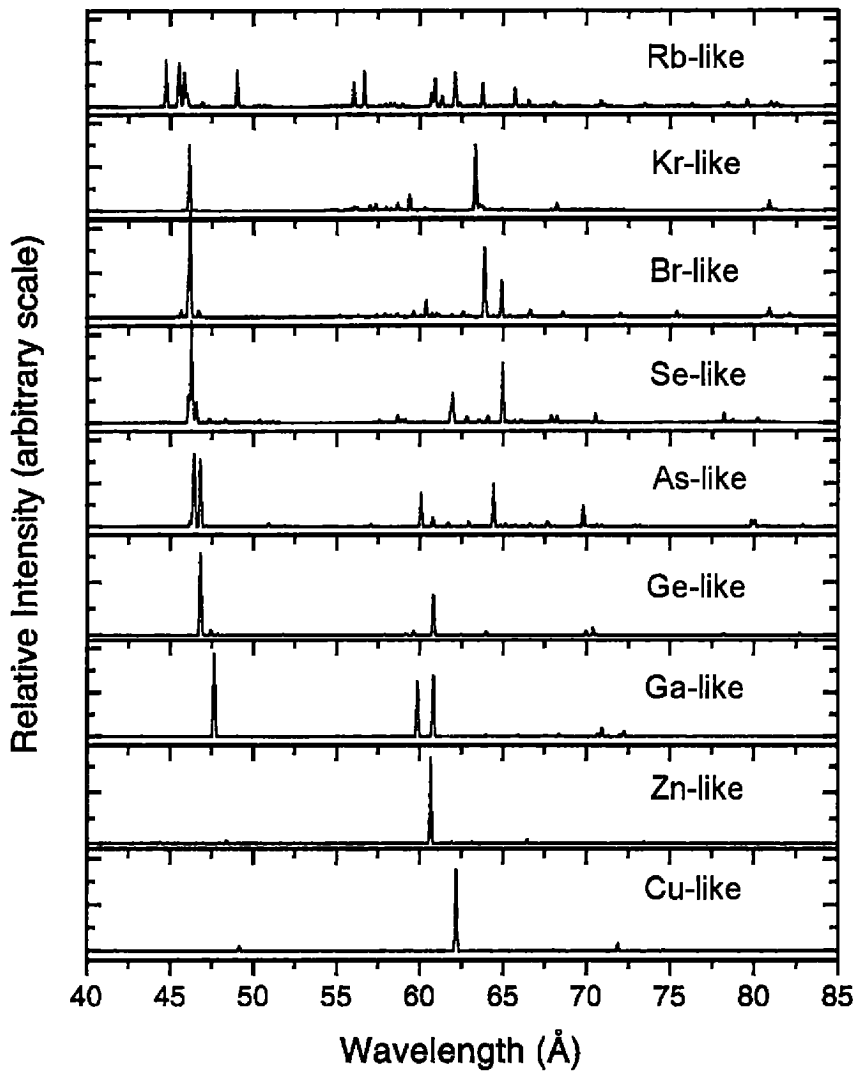

Figure 5.1: Wavelength and intensity predictions taken from results published by Fournier [13]. The range shown (40 – 85 Å) has a wealth of lines resulting from tungsten N-shell ($n = 4$) transitions in these nine charge states. Each of the predicted lines was convolved with a Gaussian function having a line center and peak height proportional to the predicted intensity – tabulated in [13] and a width (FWHM) of 0.120 Å, which is approximately that of the measured lines.

is predicted to be at a slightly higher energy, $\lambda = 48.4122$ Å. The trend continues with the Ga-like at 47.6365 Å and the Ge-like at 46.8054 Å, while the transition has now become one to the ground state of the ion. As-, Se-, Br-, and Kr-like follow suit with similar transitions predicted at 46.7944, 46.2940, 46.1881, and 46.1417 Å, respectively. Identification of this line within a particular ion's spectrum, the strongest in many of these charge states, facilitates the identification of the similar transition in neighboring charge states since the wavelength must sequentially decrease.

The intensity of such lines is also a key to the identification. In a collisionally excited plasma, transitions to the ground state will tend to be more intense than transitions to other excited states. This is exemplified for the transition just mentioned. As can be seen in the Fig. 5.1, for the Cu- and Zn-like charge states the transition is predicted to be very weak, while it is to be one of the strongest in the remaining list of ions. The relative intensities of the measured lines depends on many additional factors including the response function of the CCD camera and the charge balance of the various ions present. Nonetheless, these predictions need to be verified with high-precision experimental measurements if they are to be a trusted data source in future calculations of plasma parameters and radiative power loss.

5.2 Experimental Setup

For the measurement of the intermediate charge states of W, the flat field spectrometer described in Chapter 4 was set to cover the wavelength range of 20 – 86 Å. The MeVVA was used for the injection of W into the trap; the gas injector was used to supply the Ne for calibration; carbon, oxygen and nitrogen, occurring as background elements, were also used in calibration. EBIT was run in a steady state mode

throughout these measurements. That is, the electron beam current (I_{beam}) and energy (E_{beam}) were kept constant throughout the total data integration time. Each of the data files represents a 20 minute exposure time. Multiple exposures were taken at the same conditions until enough statistics were accumulated to facilitate line fitting. Throughout this series, I_{beam} was kept at 60 mA during W and background data acquisition and maximized for the required energy during calibration with Ne. Though at the higher energies the current could have been increased significantly, this would have made comparison of the line intensities in successive steps less clear, since the line intensities and space charge are also a function of I_{beam}. Ideally, it is the emissivity ϵ, that is, the photon emission rate, that should remain the same during the measurements. This can be written as

$$\epsilon = f_{ie} n_e n_i \sigma_i v_e,$$

where f_{ie} is the electron/ion overlap, n_e is the electron density, n_i is the ion density, σ_i is the ion cross-section, and v_e is the speed of the electrons in the beam. Since the beam current can be written as

$$I_{beam} = n_e v_e A,$$

where A is the cross-sectional area of the electron beam, ϵ can be re-written in the form

$$\epsilon = \frac{f_{ie} n_i \sigma_i I_{beam}}{A}.$$

Even assuming that the $f_{ie} n_i / A = constant$, which is true as a first order approximatation for the small energy variation considered here, it is known that σ_i varies as a function of energy. From the lowest to the highest beam energies in these measurements this may have changed by as much as 25%, which directly affected the total

number of electron/ion collisions. This, then, directly affected the signal at the detector. This only has importance when comparing spectra at differing energies, though for measurements at neighboring energies differing by 50 – 100 V the change in σ_i is small. For the calibration gas, requirements were less restrictive for the current since interest was only on the line centers, not on the peak intensity. Increasing the current does not affect the line positions or the line shapes. Settings of $I_{beam} = 27\,mA$ and $E_{beam} = 1.04\,keV$ (appropriate for creating the Li-like species) were used during the acquisition of Ne data.

A point should be made about the electron beam energies in this work. Between the emission from the electron gun and arrival at the middle of the trap region, the electrons are primarily accelerated by the potential applied to the entire set of drift tubes dubbed the "ionization potential". Added to this is the potential on the middle drift tube, which forms the axial trap, so that $U_{ion} + U_{mdl} = U_{appl}$. In these measurements, the middle drift tube was set to 200 V above the ionization potential. However, there is still another potential experienced by the electrons, which was discussed in reference to ion trapping in Chapter 3: the space charge of the electron beam itself. This space charge, a function of I_{beam}, U_{appl}, and r, the radial distance from the center of the beam, can only reduce the net potential. Several previous EBIT related dissertations have discussed this space charge in detail, the most complete description by Widmann [33]. A "rule-of-thumb" approximation of the space charge at the center of the beam is $V_{SC} = 2.5\ I_{beam}/\sqrt{U_{appl}}$, with I_{beam} in mA, U_{appl} in kV, and the result in V. The space charge potential at the edge of the beam is reduced from this by about 15 V. Table 5.1 shows a summary of the twenty-three beam energies (in either 50 or 100 V steps, ranging from an energy of 3.0 to 1.7 keV), including the

contribution from the ionization, middle drift tube, and space charge potentials. All of the beam energies listed in this work are defined as $E = e * (U_{appl} - U_{SC})$, where e is the elementary charge unit, unless noted otherwise.

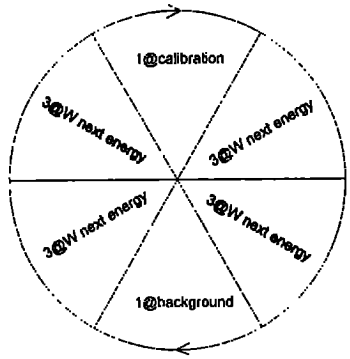

Figure 5.2: Representation of the systematic method used for taking the W EUV data. Calibration was performed with Ne; background lines were identified as H- and He-like carbon, nitrogen, and oxygen and were also be used for calibration.

In order to distinguish background lines from W lines, and to obtain a measure of the background integrated by the CCD detector, a sequence of exposures including background, calibration, and W data acquisition was implemented. Figure 5.2 is a cartoon representation of the scheme, for which each cycle required about 3 hours of acquisition time. The cycle of calibration $\rightarrow$ W $\rightarrow$ background $\rightarrow$ W $\rightarrow$ etc. was repeated until the entire energy range was covered.

The background data were actually of two types. In order to monitor for incidental lines arising from background gases, some background data were taken by only preventing the MeVVA from triggering. This mainly resulted in allowing O, N, and C lines to grow stronger. To obtain a measure of other light reaching the detector

(mainly coming from the hot electon gun), all trapping was prevented by raising the potential of the middle drift tube to a value higher than that of the top drift tube. More will be said about the advantages of inverting the trap in this way in Chapter 7 with regards to UV spectroscopy. The backgrounds with no trapping were smoothed and used as a baseline from which the spectral lines were measured.

5.2.1 Wavelength calibration

To accurately determine wavelengths using the FFS, a suitable method of *in situ* calibration was developed. The versatility of EBIT allows for rapid switching from injecting metals from the MeVVA to gas injection. This permits the regular introduction of light gases to be used for calibration. Ideally, all calibration would be performed using wavelengths (energies) from transitions that have been both precisely measured and numerically calculated. However, this is not a realistic point of view. Precision measurements of spectra throughout the EUV are not yet available. Theoretically predicted (and experimentally confirmed) wavelengths are extremely precise for H-like transitions, and very good for He-like transitions, but become worse at charge states beyond He-like. In the wavelength region of these measurements, roughly half of the spectrum is covered by several He-like transitions of O, N, and C (up to about 45 Å), but the longer wavelengths are not accessed by very well known transitions of these gases. Transitions from He-like Li, Be, or B would extend the limit to longer wavelengths, but there are technical reasons why these elements are difficult to study in EBIT. Therefore, transitions of Li-like Ne were used to cover the range from 55 – 85 Å. Though measurements of these lines have uncertainties of about 5 mÅ, the lines suffice for calibration, but do limit the certainty of these

Table 5.1: Summary of the twenty-three beam energies (in descending order) used to ionize and excite trapped W. The total energy is proportional to the sum of the ionization and the middle drift tube potentials minus the calculated space charge.

W Injection Electron Beam Energies

V_{ion} kV	V_{mdt} kV	I_{beam} mA	V_{SC} kV	E_{total} keV	V_{ion} kV	V_{mdt} kV	I_{beam} mA	V_{SC} kV	E_{total} keV
2.90	0.20	59	0.08	3.02	2.10	0.20	60	0.10	2.20
2.80	0.20	59	0.08	2.92	2.05	0.20	60	0.10	2.15
2.70	0.20	59	0.09	2.81	2.00	0.20	60	0.10	2.10
2.60	0.20	59	0.09	2.71	1.95	0.20	60	0.10	2.05
2.50	0.20	60	0.09	2.61	1.90	0.20	60	0.10	2.00
2.45	0.20	60	0.09	2.56	1.85	0.20	60	0.10	1.95
2.40	0.20	60	0.09	2.51	1.80	0.20	60	0.11	1.89
2.35	0.20	60	0.09	2.46	1.75	0.20	60	0.11	1.84
2.30	0.20	60	0.09	2.41	1.70	0.20	60	0.11	1.79
2.25	0.20	60	0.09	2.36	1.65	0.20	60	0.11	1.74
2.20	0.20	60	0.10	2.30	1.60	0.20	60	0.11	1.69
2.15	0.20	60	0.10	2.25					

measurements, particularly near the longer wavelength end of the spectra. A list of calibration lines used for this (and other) measurements using the FFS can be found in Appendix A, Table A.1. Eight of these known transitions were measured and their line centers were determined by fitting the resultant peaks with Gaussian functions.

A third-order polynomial was fit to this series of data to obtain a dispersion equation for the entire span of the subtended spectral range. The quality of the calibration was tested by fitting weaker, yet well known, "test" lines from the calibration gases. The statistical deviation of the test points was determined to be within approximately 4 mÅ of their accepted values. The statistical deviation of the residuals of the fitted points was measured to be close to 3 mÅ.

5.2.2 Intensity calibration

The intensity of spectral lines gives information about the state of the plasma. For instance, certain transitions may be affected by the density of the plasma and measurement of the intensity can be used as a diagnostic of the density. Under certain circumstances it can give information about the charge state abundance of ions, collisional cross-sections, or recombination rates. Proper theoretical predictions of intensities are critical to such diagnostics as the total impurity radiative power loss rate in a magnetically confined fusion plasma. Reliable intensity measurements, however, are at best difficult, and at worst, sometimes impossible. To obtain a measure of the absolute intensity of a transition several parameters other than the signal rate at the detector are needed. These parameters include the solid angle of the source subtended by the spectroscopic system, any directionality of the photons from the source, the density of the source ions, polarization of the transition, the charge state ratio of the ions, the reflectivity of the grating, and the efficiency of the detector, the last two of which are sensitive functions of the photon energy. For the purposes here, a measure of the absolute intensity is not necessary; measurement of the relative intensity of spectral lines from within a single charge state is sufficient. For this, only

the reflectivity of the grating and the efficiency of the detector as functions of energy are needed.

Several recent studies of the efficiency of spectrometer systems in the EUV using CCD detectors have been reported [50, 51, 54, 55]. Closely related to this work is the measurement by Saemann and Eidmann from 1998 [51]. In it they report an absolute sensitivity calibration of a flat-field spectrometer in the wavelength range 10 70 Å by means of a laser generated plasma of well known x-ray conversion. They implemented a 2400 l/mm *Hitachi* flat-field grating and a back-thinned CCD detector: this is the same type of system as used in the present measurements. Their spectrometer set-up consisted of two mirrors used at grazing incidence, a slit, the grating, and the CCD. An independent measurement of the efficiency of the CCD detector resulted in a quantum efficiency measurement of the detector itself. By unfolding this efficiency from the results from the spectrometer system they were able to obtain a result independent of the CCD as well. Figure 5.3 shows the portion of the efficiency curve for the FFS system used by Saemann and Eidmann related to the present work. The severe dip in the curve near 42.5 Å is attributed to a thin oil layer on the surface of the mirrors used in their spectrometer. Though such mirrors do not exist in the EBIT spectrometer, it is known that the CCD detector has a thin layer of oil (the result of pump oil from a vacuum accident) so it is likely a similar result would be measured from the EBIT instrument. As such, this curve has been used to adjust the intensity measurements of the intermediate charge state W transitions; the 'dip' only affects very few of the measured lines. Proposals have been made to make an absolute efficiency measurement of the EBIT-FFS, but it will likely be nearly a year before those potential results would be available. Other than slight differences inherent to

any two CCD detectors, the efficiency curve in Fig. 5.3 should be compatible to the LLNL-EBIT system.

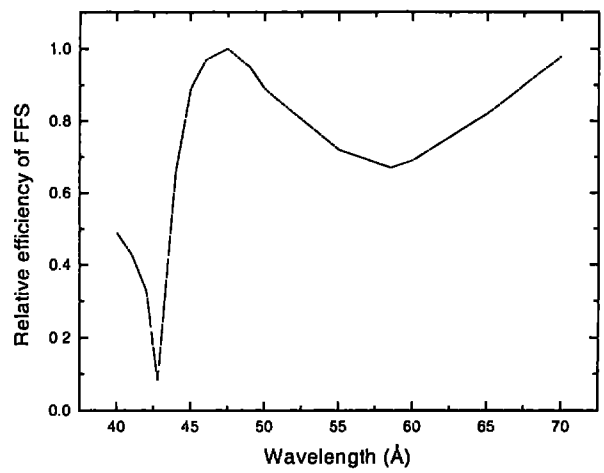

Figure 5.3: Measured relative efficiency of a FFS system similar to the one used in the present measurements at EBIT.

5.3 Experimental Results

Figure 5.4 shows a series of the two-dimensional W raw-data spectra taken with the flat field spectrometer[10]. The x-axis shown is an approximate wavelength scale for display purposes. The individual spectra are marked with their associated beam energy (y-axis) and are stacked to show how spectral lines can be identified not only by wavelength, but by charge state. For instance, the leftmost line near 60 Å in the bottom spectrum (2.61) has been identified as the $(4s+)^1{}_{J=\frac{1}{2}} - (4p+)^1{}_{J=\frac{3}{2}}$ transition from the Cu-like isoelectronic sequence. It is, in fact, the strongest line observed from

[10]Note the random white dots in the figure. Each of these is caused by the interaction of a cosmic ray with the CCD. Removal of these spots was performed by the filtering program described in Appendix C.

this charge state. Note that by 2.46 it is very weak, by 2.41 it is hardly discernible, and by 2.36 it is non-existent. Association with the Cu-like charge state can be confirmed by the fact that the ionization energy of the Zn-like charge state is 2.37 keV, so at energies below this level, no Cu-like W can be present. Much of the charge state identification throughout this work has been performed using this type of analysis as well as comparison to previously reported measurements and predictions. In the following will be presented measurements from the Rb-like (W^{37+}) through Cu-like (W^{45+}) charge states of W, including wavelength assignments and relative intensities.

All of the data files at each of the twenty-three electron beam energies studies were independently filtered of cosmic rays. The smoothed baseline was then subtracted from each spectrum, and the files of the same energy were summed. Each of the summed spectra were then analyzed by fitting the peaks with Gaussian functions using the *Peak Fitting Module* of *Microcal's Origin, version 4.0*, software. The width of the lines were linked, but allowed to vary during the fitting process. In other words, all of the fitted lines in a spectrum were constrained to have the same FWHM, but this parameter was optimized for each spectrum. Of interest from the fit results was the Gaussian line center and total area. The line centers (in channels) were converted to wavelength units using the 3^{rd} order polynomial dispersion equation. By following the developments or decay of the line intensity of any line through a series of energies, the charge state from which the line emanated could be identified. Comparison of wavelengths with the calculations of Fournier and of previous measurements allowed for identification of most of the related transitions. Tables 5.2 through 5.10 summarize the line identifications by charge state. The levels (lower and upper) listed in the tables use the following naming scheme, as described by Fournier. In the intermediate

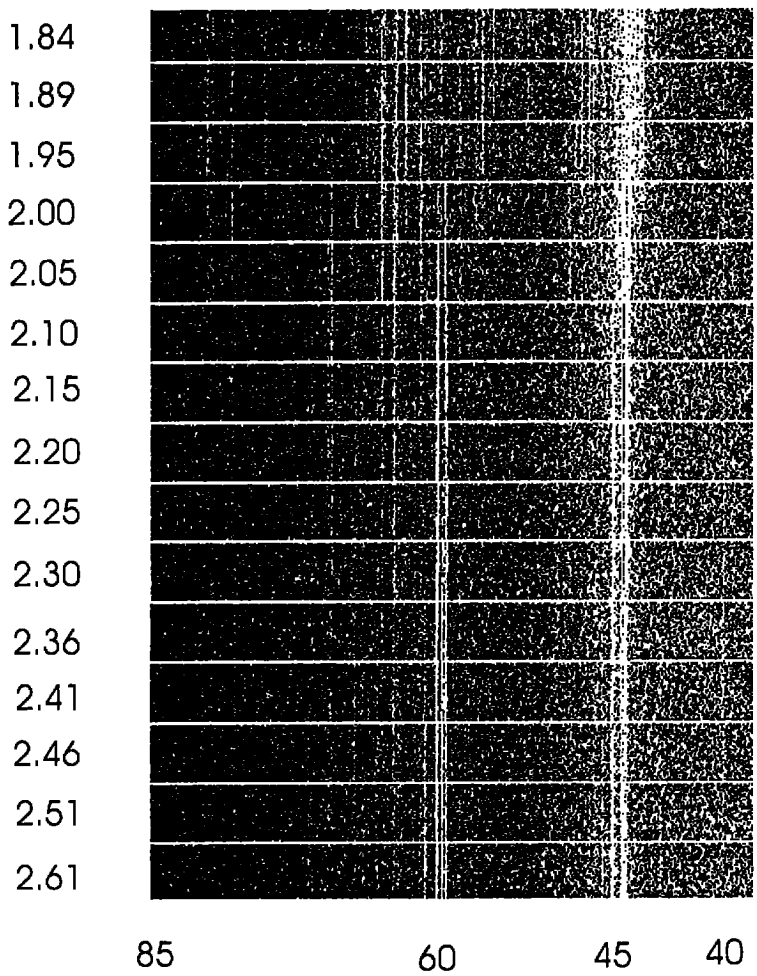

Figure 5.4: Series of spectra taken with the flat-field spectrometer. Each of the fifteen images was obtained at a different beam energy and represents 20 minutes of data accumulation, during which W was injected into EBIT and the electron beam current was set to 60 mA. The spectra are identified by the electron beam energy (keV). The wavelengths (Å) listed at the bottom are only approximate. The short wavelength end of each spectra was cropped to highlight the most interesting region for W; the full wavelength range extends to 20 Å.

charge states of W, LS coupling is no longer appropriate. RELAC's intermediate-coupling calculations are carried out on the jj-coupling basis set. The jj-orbitals nlj are represented by $nl+$ or $nl-$, where the + indicates $j = l + 1/2$ and the − indicates $j = l - 1/2$. Then, $3d_{3/2} = 3d-$ and $3d_{5/2} = 3d+$. In the tables, when both nlj orbitals in a shell are full, the shell is represented by $(nl)^k$, where k is the maximum occupancy of the shell. As an example, $(3d-)^4(3d+)^6 = (3d)^{10}$. These closed shells and subshells are actually omitted from the tables except where omission might result in confusion.

The nine tables are all organized in the same way. First are listed the atomic levels involved in the transition, as described above. Then are the total J values of the lower and upper levels. Next are listed the predicted (from Fournier) and measured (present experiments) wavelengths. In ( ) following the measured wavelengths is a measure of the statistical uncertainty of each wavelength. The best lines have statistical errors which are less than 2 mÅ. Larger error bars (up to a factor of 10) result from transitions which are either somewhat weak, or are blended with neighboring lines from the same or close charge states. An additional 4 mÅ should be added to the uncertainty of each line due to the poor precision of the calibration beyound 45 Å. Finally, the predicted and measured relative intensities are listed. By relative intensity is meant for the calculated transitions the ratio of the line's collisional-radiative line intensity to that of the strongest predicted line of the same charge state, and for a measured line the ratio of that line's area to the measured area of the strongest predicted line in that charge state after taking account of the intensity calibration discussed in the previous section. The strongest predicted line is used rather than the strongest measured line so that comparisons to theory can be better made.

Table 5.2: Rb-like W^{39+}

{ground state: $(4s)^2(4p)^6(4d-)^1$ $J = 3/2$}							
Level				Wavelength		Intensity	
Lower	Upper	J_l	J_u	Pred.	Meas.	Pred.	Meas.
$(4d-)^1$	$(4p-)^1(4p+)^4(4d-)^2$	3/2	3/2	44.7664	45.7810(22)	1.00	1.00
$(4d-)^1$	$(4p-)^1(4p+)^4(4d-)^1(4d+)^1$	5/2	3/2	45.4795	46.0640(55)b	0.39	0.25
$(4d-)^1$	$(4p-)^1(4p+)^4(4d-)^1(4d+)^1$	5/2	7/2	45.5562	46.0640(55)b	0.75	
$(4d-)^1$	$(4p-)^1(4p+)^4(4d-)^2$	3/2	5/2	49.0304	49.6407(54)	0.78	0.58
$(4d-)^1$	$(4p)^6(4f-)^1$	3/2	5/2	56.0552	56.8797(41)	0.52	0.35
$(4d-)^1$	$(4p-)^1(4p+)^4(4d+)^2$	3/2	5/2	56.6804	57.7547(14)	0.38	0.23
$(4d-)^1$	$(4p-)^1(4p+)^4(4d-)^1(4d+)^1$	3/2	1/2	60.7172	—	0.21	—
$(4d-)^1$	$(4p)^6(4f+)^1$	5/2	7/2	60.9222	61.9200(83)b	0.59	0.15
$(4d-)^1$	$(4p)^6(4f-)^1$	5/2	5/2	61.3401	61.9200(83)b	0.22	
$(4d-)^1$	$(4p-)^2(4p+)^3(4d+)^2$	5/2	5/2	62.0895	63.4319(119)b	0.46	0.13
$(4d-)^1$	$(4p-)^2(4p+)^3(4d+)^2$	5/2	3/2	62.1379	63.4319(119)b	0.34	
$(4d-)^1$	$(4p-)^2(4p+)^3(4d-)^1(4d+)^1$	3/2	3/2	63.7745	64.8250(200)	0.50	0.16
$(4d-)^1$	$(4p-)^2(4p+)^3(4d-)^1(4d+)^1$	3/2	5/2	65.7032	66.29252(147)	0.38	0.12
$(4d-)^1$	$(4p-)^2(4p+)^3(4d-)^2$	3/2	1/2	81.2985	81.4573(89)b	0.02	0.05
$(4d-)^1$	$(4p-)^2(4p+)^3(4d-)^2$	3/2	3/2	81.3594	81.4573(89)b	0.05	

Figure 5.5 shows the nine measured charge states of W displayed in a similar fashion to the calculations of Fournier on page 50. Each of the displayed spectra are accumulations of all data taken at each energy after background subtraction. Notice, however, that the apparent baseline for the lower energy charge states is higher than for the higher energies. This suggests the existence of many more unresolved, low-intensity lines adding to a quasi-continuum. This agrees with predictions of many

Table 5.3: Kr-like W^{39+}

{ground state: $(4s)^2(4p)^6$ $J = 0$}							
Level				Wavelength		Intensity	
Lower	Upper	J_l	J_u	Pred.	Meas.	Pred.	Meas.
$(4p)^6$	$(4p-)^1(4p+)^4(4d-)^1$	0	1	46.1417	46.6703(12)	1.00	1.00
unknown	unknown	-	—	--	49.36511(57)		0.11
unknown	unknown	---	—	· · ·	50.2057(64)	-··	0.09
unknown	unknown	—	--	—	57.7171(70)	—	0.18
unknown	unknown	—	--	—	62.3659(43)	—	0.14
$(4p)^6$	$(4p-)^1(4p+)^4(4d+)^1$	0	1	63.3262	63.8834(41)	0.96	0.22
$(4p)^6$	$(4p-)^1(4p+)^4(4d-)^1$	0	1	80.8856	80.6420(226)	0.13	0.06

weak N-shell transitions and the measurement of a quasi-continuum found in tokamak and laser plasma spectra at these energies. Even though these EBIT measurements are well resolved in both wavelength and electron energy, a remnant of this feature still persists.

The most notable difference between the measured and predicted transitions is that the measured lines show a lower than predicted intensity in the 60 Å range as compared to the 45 Å lines. This is exemplified in Fig. 5.6, where the spectra obtained at 2.05 keV (optimized for Se-like) is shown along with a simulated W-spectrum using Fournier's predictions weighted as 10% As-, 35% Se-, 35% Br-, 15% Kr-, and 5% Rb-like. All of the strong features in the measured spectrum appear in the simulated data, albeit, regularly at shorter wavelengths. Even after making the adjustment for the energy response of the CCD detector, the shorter wavelength transitions, that is, those which are typically of the type $l = 2 - 1$, appear much stronger than predicted.

Table 5.4: Br-like W^{39+}

{ground state: $(4s)^2(4p-)^2(4p+)^3$ $J = 3/2$}							
Level				Wavelength		Intensity	
Lower	Upper	J_l	J_u	Predicted	Measured	Pred.	Meas.
$(4p-)^2(4p+)^3$	$(4p-)^1(4p+)^3(4d+)^1$	3/2	5/2	45.6687	45.9539(26)	0.09	0.00
$(4p-)^2(4p+)^3$	$(4p-)^1(4p+)^3(4d-)^1$	3/2	1/2	46.0686	46.8267(09)b	0.44	3.61
$(4p-)^2(4p+)^3$	$(4p-)^1(4p+)^3(4d-)^1$	3/2	3/2	46.1808	46.8267(09)b	1.00	
$(4p-)^2(4p+)^3$	$(4p-)^1(4p+)^3(4d-)^1$	3/2	5/2	46.1881	46.8267(09)b	0.55	
$(4p-)^2(4p+)^3$	$(4p-)^1(4p+)^3(4d-)^1$	3/2	5/2	50.0103	50.6605(99)	0.05	0.17
$(4p-)^2(4p+)^3$	$(4s+)^1(4p)^6$	3/2	1/2	60.3869	61.0499(29)	0.24	0.33
$(4p-)^2(4p+)^3$	$(4p-)^2(4p+)^2(4d+)^1$	3/2	5/2	63.8774	64.6606(155)	1.00	1.00
$(4p-)^2(4p+)^3$	$(4p-)^2(4p+)^2(4d+)^1$	3/2	3/2	64.9009	65.6575(59)	0.53	0.42
$(4p-)^2(4p+)^3$	$(4p-)^2(4p+)^2(4d-)^1$	3/2	5/2	80.8922	81.1531(03)	0.11	0.21

relative to the 60 Å band of lines.

The Rb-like charge state is the most complex of the series of ions in this study. With thirty-five bound electrons, the ground state has nine electrons outside of the greatest-n closed shell ($n = 3$ is closed) leading to a very complex level configuration. Adding to this complexity are the many possible allowed transitions in the wavelength range 40 -- 80 Å. Ten lines were measured which could be attributed to this charge state. As is true throughout this work, the lines' identification showed that the predicted wavelengths were all somewhat shorter - that is, higher in energy – by about 0.8 Å, on average. This difference remains approximately the same regardless of whether the transition is to the ground state or not. Four of the measured lines are believed to be unresolved blends of transition pairs. Each of these states only differs in

Table 5.5: Se-like W^{40+}

{ground state: $(4s)^2(4p-)^2(4p+)^2$ $J=2$}							
Level				Wavelength		Intensity	
Lower	Upper	J_l	J_u	Predicted	Measured	Pred.	Meas.
$(4p-)^2(4p+)^2$	$(4p-)^1(4p+)^2(4d-)^1$	2	1	46.1020	46.3776(27)	0.46	0.57
$(4p-)^2(4p+)^2$	$(4p-)^1(4p+)^2(4d-)^1$	2	2	46.2597	46.9573(21)b	0.80	3.36
$(4p-)^2(4p+)^2$	$(4p-)^1(4p+)^2(4d-)^1$	2	3	46.2940	46.9573(21)b	1.03	
$(4p-)^2(4p+)^2$	$(4p-)^1(4p+)^2(4d-)^1$	2	3	47.3587	47.6044(42)	0.07	0.71
$(4p-)^2(4p+)^2$	$(4p-)^1(4p+)^2(4d-)^1$	2	2	48.3487	48.7460(56)	0.06	0.26
$(4p-)^2(4p+)^2$	$(4s+)^1(4p-)^2(4p+)^3$	2	1	58.6736	59.5257(66)	0.12	0.42
$(4p-)^2(4p+)^2$	$(4s+)^1(4p-)^2(4p+)^3$	0	1	61.8501	62.1934(163)	0.17	0.30
$(4p-)^2(4p+)^2$	$(4s+)^1(4p-)^2(4p+)^3$	2	2	61.9725	62.6885(38)	0.48	0.74
$(4p-)^2(4p+)^2$	$(4p-)^1(4p+)^2(4d-)^1$	2	3	64.9719	65.8729(25)	1.00	1.00
$(4p-)^2(4p+)^2$	$(4p-)^1(4p+)^2(4d-)^1$	2	2	70.5446	71.1180(34)	0.15	0.23
$(4p-)^2(4p+)^2$	$(4p-)^1(4p+)^2(4d-)^1$	2	3	78.2018	78.9521(121)	0.16	0.32

the total J value of the upper state. The transitions are marked in the tables by a 'b' following the measured wavelength. The second component of each line pair is listed with no measured wavelength. Only a single Rb-like transition ($\lambda_{pred.} = 60.7172$ Å) that was predicted to be at least as intense as other identified lines is not found.

Removing another electron from the Rb-like charge state produces an ion of the Kr sequence. Many fewer lines were predicted for this state. Seven were measured, but only three of these could be attributed to predicted Kr-like transitions, even though the other four had intensities which peak at the same beam energy as the other Kr-like lines. Transitions from neighboring states were also checked as candidates,

Table 5.6: As-like W^{41+}

{ground state: $(4s)^2(4p-)^2(4p+)^1$ $J = 3/2$}							
Level				Wavelength		Intensity	
Lower	Upper	J_l	J_u	Pred.	Meas.	Pred.	Meas.
$(4p-)^2(4p+)^1$	$(4p-)^1(4p+)^1(4d-)^1$	3/2	3/2	46.4378	47.0480(58)	0.94	0.73
$(4p-)^2(4p+)^1$	$(4p-)^1(4p+)^1(4d-)^1$	3/2	5/2	46.7944	47.2873(81)	1.00	1.00
$(4p-)^2(4p+)^1$	$(4p-)^1(4p+)^1(4d-)^1$	3/2	3/2	50.8943	51.0906(108)	0.04	0.04
$(4p-)^2(4p+)^1$	$(4s+)^1(4p-)^2(4p+)^2$	3/2	3/2	60.0871	60.7285(11)	0.51	0.23
$(4p-)^2(4p+)^1$	$(4s+)^1(4p-)^2(4p+)^2$	3/2	5/2	64.4133	64.8883(47)	0.63	0.18
$(4p-)^2(4p+)^1$	$(4p-)^2(4d+)^1$	3/2	5/2	69.7964	70.1496(39)	0.30	0.08
$(4p-)^2(4p+)^1$	$(4p-)^2(4d-)^1$	3/2	3/2	80.0287	80.8888(166)	0.09	0.02

Table 5.7: Ge-like W^{42+}

{ground state: $(4s)^2(4p-)^2$ $J = 0$}							
Level				Wavelength		Intensity	
Lower	Upper	J_l	J_u	Pred.	Meas.	Pred.	Meas.
$(4s)^2(4p-)^2$	$(4s)^2(4p-)^1(4d-)^1$	0	1	46.8054	47.1905(28)	1.00	1.00
$(4s)^2(4p-)^2$	$(4s)^2(4p-)^2(4p+)^1$	0	1	60.8203	61.3039(60)	0.49	0.55
$(4s+)^1(4p-)^2(4p+)^1$	$(4s+)^1(4p-)^2(4d+)^1$	1	2	70.3807	70.4349(65)	0.01	0.04
$(4s)^2(4p-)^1(4p+)^1$	$(4s)^2(4p-)^1(4d-)^1$	2	2	82.7390	83.2887(39)	0.00	0.02

but no satisfactory assignments could be made. The two most intense measured lines' wavelengths were about 0.6 Å longer than predicted, while the third was at a shorter wavelength. This weak line, however, had too poor statistics to attain a very accurate measurement. The following three charge states had seven, ten, and seven

Table 5.8: Ga-like W^{43+}

{ground state: $(4s)^2(4p-)^1$ $J = 1/2$}							
Level				Wavelength		Intensity	
Lower	Upper	J_l	J_u	Pred.	Meas.	Pred.	Meas.
$(4p-)^1$	$(4d-)^1$	1/2	3/2	47.6365	47.9029(24)	1.00	1.00
$(4p-)^1$	$(4s--)^1(4p-)^1(4p+)^1$	1/2	1/2	59.8762	60.6157(42)	0.67	0.35
$(4p-)^1$	$(4s-)^1(4p-)^1(4p-)^1$	1/2	3/2	60.8198	61.3341(21)	0.75	0.62

Table 5.9: Zn-like W^{44+}

{ground state: $(3d)^{10}(4s)^2$ $J = 0$}							
Level				Wavelength		Intensity	
Lower	Upper	J_l	J_u	Pred.	Meas.	Pred.	Meas.
$(4s-)^1(4p-)^1$	$(4s+)^1(4d+)^1$	1	2	44.3837	44.5299(62)	0.01	0.04
$(4s+)^1(4p-)^1$	$(4s--)^1(4d-)^1$	1	2	48.4122	48.6165(27)	0.33	0.09
$(4s)^2$	$(4s+)^1(4p+)^1$	0	1	60.6646	60.9310(17)	1.00	1.00
$(4s+)^1(4p+)^1$	$(4s+)^1(4d-)^1$	2	2	66.4622	66.9301(40)	0.05	0.04

measured lines, respectively. Most of these lines were found in the 45 Å complex. The decreased resolution of lines within this grouping from their neighbors resulted in increased scatter of the measured wavelengths. The difference between theory and experiment averaged, again, about 0.6 Å. The final four states in this series produced a combined fifteen measured lines in this range. These lines all were well resolved and

Table 5.10: Cu-like W^{45+}

{ground state: $(3d)^{10}(4s+)^1$ $J = 1/2$}							
Level				Wavelength		Intensity	
Lower	Upper	J_l	J_u	Pred.	Meas.	Pred.	Meas.
$(4p-)^1$	$(4d-)^1$	1/2	3/2	49.1651	49.2080(63)	0.06	0.26
$(4s+)^1$	$(4p+)^1$	1/2	3/2	62.1868	62.3355(19)	1.00	1.00
$(4d-)^1$	$(4f-)^1$	3/2	5/2	68.0099	68.1569(28)	0.01	0.04
$(4p+)^1$	$(4d+)^1$	3/2	5/2	71.8900	71.9437(503)	0.10	0.08

seen over many beam energies. Additionally, since the ionization potentials of these charge states are also more separated than the others, the wavelength measurements were notably more precise than others. These lines also agreed better with wavelength predictions than those of lower charge states, averaging an offset of only 0.3 Å, with the Cu-like sequence being the most accurately described (having a 0.1 Å offset).

5.4 Discussion

The measurements of the wavelengths of the W-EUV radiation from intermediate charge states has shown agreement to within 1% with the fully-relativistic *ab initio* calculations. Even though this agreement is not great, it is sufficient enough to identify most of the lines in the spectra of EBIT due to the capability of optimizing particular charge states. In the case of a tokamak plasma, for which charge state resolution is not nearly as good as EBIT, the calculations are only good enough to identify groups of lines. Furthermore, for high-n_e laser plasmas with many charge

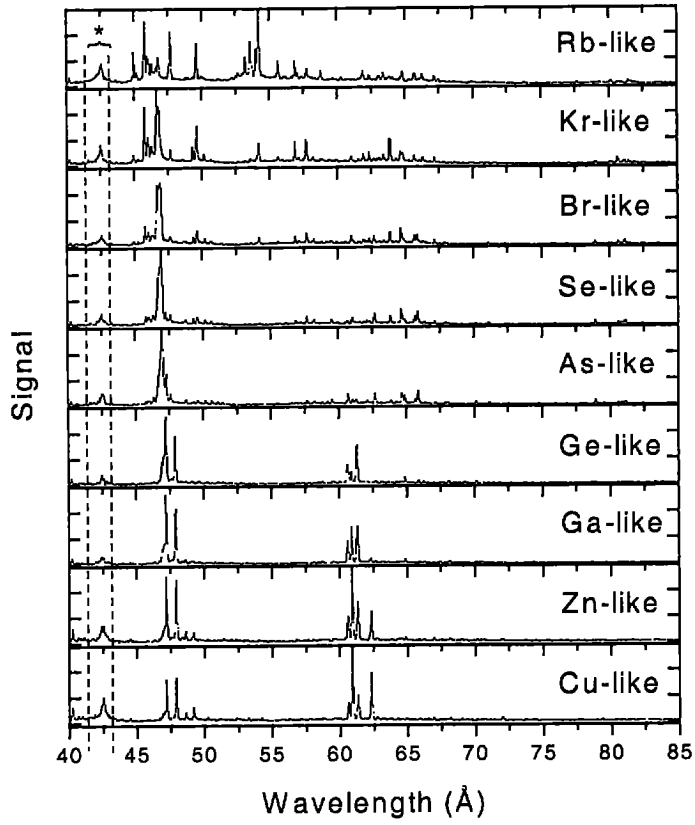

Figure 5.5: Line-out spectra of W at nine energies optimizing the charge states measured in these experiments. The intensity has been scaled according to the method previously described. The raised section within the dotted line and marked by an * is an artifact of the sharp drop due to the carbon-edge in the intensity calibration. Each spectrum is marked by the charge state optimized at that particular energy. The beam energy of each spectrum was 1.79, 1.89, 1.95, 2.05, 2.10, 2.37, 2.46, 2.71, and 3.02 keV for the Rb- through Cu-like, respectively. Typically, three or four other charge states were present simultaneously at varying stages of charge balance. Comparison of this to the similar figure derived from the calculations of Fournier (Fig. 5.1) in general shows good agreement, though the details of intensities are sometimes significantly different. The measured wavelengths and relative line intensities are listed in Tables 5.2 through 5.10.

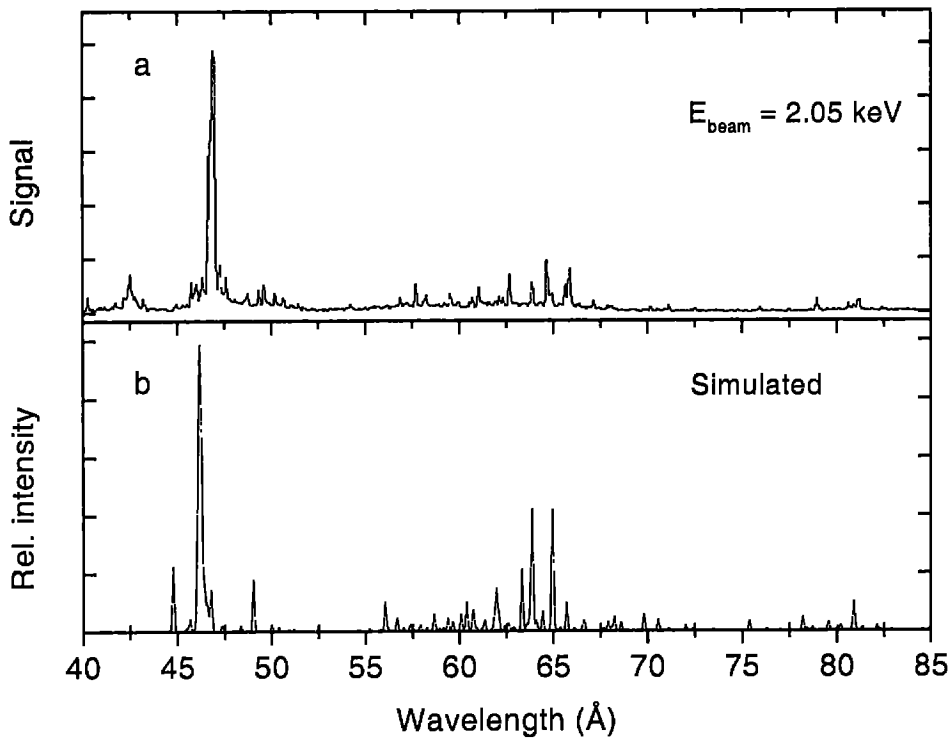

Figure 5.6: Se-like W compared to simulated spectrum. a) EBIT spectrum optimizing the Se-like charge state of W; b) a simulated spectrum from the calculations of Fournier with several charge states represented at levels similar to those found in the EBIT spectrum.

states and many more lines present, identification of most of the lines is hopeless. In fact, the calculations can even be somewhat misleading with shifted predictions leading to the incorrect identification of charge states. Nonetheless, given the complexity of the ions, theory does a good job of producing a first order prediction for the wavelengths as long as experiments such as those at EBIT can be used to test the theory.

In that light, it is not surprising that there is diverging agreement between theory and these measurements as the ionization stages increase in the number of bound

electrons. This is expected as the number of possible transitions increases and the structure becomes more complicated. More refined calculations have been shown to predict the transition energies with better accuracy. [The best calculations and measurements of Cu-like $(4s+)^1_{J=\frac{1}{2}} - (4p+)^1_{J=\frac{3}{2}}$ transitions in the EUV from high-Z ions are addressed in more detail in Chapter 6, where agreement of one part in one-thousand is achieved.] More surprising is the disagreement in the predicted versus measured relative intensities of the transitions. Even after making the adjustments to the spectra for the energy response of the spectrometer system, there remains a discrepancy on the order of 2× in the ratio of the "60 Å" group to the "45 Å" group intensities. Specifically, the intensity of the $4p - 4d$ transitions appear more intense than predicted. Several possible explainations for the disagreement have been investigated and are summarized below.

It is important that the efficiency of the spectroscopic system be known as a function of energy. This includes the response of the reflection grating and the response of the detector. The detector response is known to depend on the energy of the impinging photon. In fact, because silicon is effectively opaque to radiation in the EUV, a thinned, back-side illuminated CCD is used for detection in this region. However, the number of electrons collected by the CCD per incident photon, the quantum efficiency, must be known accurately to make a proper assessment of the relative intesity of the spectral lines. The quantum efficiency depends upon the manufacturing process, the thickness of the silicon oxide layer and the resulting "dead layer" where electrons are repelled rather than collected, as well as on the average photon energy necessary to create an electron-hole pair in the active silicon. Because of the variations inherent in each CCD (mainly due to the variation in the thickness of the dead layer), ideally the

spectrometer would be calibrated using a standard light source such as synchrotron radiation. Instead, for this work, the published efficiency of a spectrometer system similar to the one used at EBIT has been taken, leaving some possiblity that the disagreement could be due to the lacking instrument calibration.

There are also certain approximations in the calculations that need be examined for possible effects. In these calculations the nuclear charge is assumed to be a point charge, whereas other calculations assume some sort of finite charge distribution for the nuclear charge. It is noted that this difference only matters for orbitals which penetrate the nucleus and only affects the calculated energy of the transition, and, therefore, a point charge should be a valid approximation in these calculations. Even so, any small adjustment this may cause to the calculation of the transition energy should have a very small effect on the calculation of the intensities of the transitions.

Another possible cause of variation in the predicted intensities is the lack of inclusion of recombination effects in the calculations. Through the processes of recombination and cascading decays from higher levels, states which are not prone to population through the ionization/excitation process may yet be significantly populated. This may, in turn, weight the intensities of the lines in these measurements differently than in the calculations. Inclusion of these effects in the calculations would be useful, though it is understood that this would result in more complicated atomic codes.

A final factor that has been considered is the differing plasma parameters between tokamak calculations – those reported in [13] – and EBIT measurements. Though the typical tokamak ion density of is similar to that of the EBIT, a tokamak plasma typically has a broad Maxwellian electron temperature distribution with wings extending the energy of a significant portion of the electrons to values much higher and

lower than the average. On the other hand, EBIT has a very well defined electron energy with a spread measured to be only about 50 eV. The possibility that the intensity difference was the result of the difference between these two types of source was checked by re-computing the results for conditions more similar to those found in EBIT[11] [56]. Though some of the intensities changed by a significant fraction, none of the strongest lines varied by a significant amount and no systematic trend of the intensities was identified.

[11] At the request of this author, Fournier graciously re-calculated the transition energies and predicted intensities for intermediate charge state ions of W using parameters similar to those found in the EBIT.

6 CU-LIKE IONS

The study of spectra in the EUV from ions along the Cu isoelectronic sequence provides a stage for attaining important benchmarks through both precision experimentation and modern atomic structure theory. From the experimental standpoint, the production and charge-state isolation of Cu-like ions is easier than for ions of other charge states. The ionization potential necessary to create Cu-like ions is typically of the order 1 – 4.5 keV for the elements being considered here. This is an energy range easily accessible by many experimental devices such as tokamaks, laser devices, and EBITs. Even though the next higher charge state, the Ni-like sequence, is produced within only about 0.1 keV, the spectra of these ions is very weak in the EUV owing to the fact that the spectra are mainly $n' \rightarrow 3$ ($n' = 4, 5, 6 \ldots$) transitions emitting at much higher, X-ray, energies. Therefore, there is a broad range of energies available to create a predominantly Cu-/Ni-like charge balance by burning out the lower charge states, and creating a very 'clean' EUV spectra with only mostly Cu-like lines remaining. This, in turn, reduces the possibility of line blends, or even misidentification. For theory, the Cu-like sequence represents a complicated atomic system, having twenty-nine electrons, that can be simplified due to the fact that only a single valence electron exists outside of the closed $n = 3$ shell. The Cu-like system is, in a way, similar to a H-like system if, as a first approximation, the electrons residing in teh closed shells are assumed to be only weakly interacting with the valence electron. This is even true in a physical sense in that the closed-shell electrons couple and reduce their "individuality". Mastering the techniques to completely describe sin-

gle valence electron systems is a first step in accurately describing all multi-electron atomic systems.

6.1 Theoretical predictions of the energy of the $4s_{1/2} - 4p_{3/2}$ transitions

Many calculations to predict the energy levels and transition energies for the lowest levels of the Cu-like ion have been made in the last twenty years. The first reported measurements of the wavelengths of Cu-like transitions from heavy elements was reported by Seely *et al.* in 1986 in which they compared the wavelengths from Au, Pb, Bi, Th, and U measured using the OMEGA laser to theoretical values calculated with a multiconfiguration Dirac-Fock (MCDF) package, using the extended average level (EAL) method, with transverse Breit and QED corrections [57]. They reported significant differences between the measured and calculated values which they attributed to "a departure from the scaled hydrogenic QED contribution to the 4s energy," in other words, to a deficiency in the theoretical treatment of the QED. In the following year, Cheng and Wagner repeated the calculations made by the previous group, but with some modifications, in an attempt to understand the causes of the difference between theory and experiment [18]. They again used the MCDF package, but instead of the EAL method they calculated the transitions in the optimal level (OL) approximation to account for core relaxation at each energy level. In addition, they included finite-nuclear size effects. With results that agreed better with experiment than the previous calculations they concluded that the residual discrepancy noted by Seely *et al.* was probably due to the omission of the finite-nuclear size effects which are important for low n and l states, and that their improved treatment of QED corrections

was good enough to give good estimates of its contributions. In 1989, a second paper by Seely *et al.* reported the observation of $4s_{1/2} - 4p_{3/2}$ transitions in Cu-like ions from mid-Z elements (including Sn, Xe, La, Nd, Eu, Gd, Dy, and Yb) made on the Princeton Large Torus tokamak (PLT) [9]. They concluded from comparisons of these wavelengths to the calculations of Cheng and Wagner that significant discrepancies still existed and attributed these to electron correlation corrections that are not accounted for in the calculation. So in the course of two years time there appeared some debate over whether there was good agreement between theory and experiment, and the role of QED, finite nuclear size, and correlation corrections in these calculations.

Between 1988 and 1990 a series of three papers on the topic of relativistic many-body perturbation theory (MBPT) studies of energy levels of ions having a single valence electron outside of a closed shell was published by Johnson *et al.*, the third of which reported calculations of energies of $4s_{1/2}$ and $4p_{3/2}$ states of Cu-like ions with nuclear charge in the range $Z = 29 - 92$. These calculations were based on Dirac-Fock (DF) wavefunctions and included Coulomb correlation corrections (second and third order), retarded Breit interaction, correlation corrections to the Breit interaction (second and third order), finite nuclear size corrections, and reduced mass and mass-polarization corrections. They did not include QED corrections such as the electron self-energy and vacuum polarization, but have otherwise been considered to be the most complete theoretical treatment to date.

Two calculations have sought to provide the necessary QED corrections so that comparisons between experiment and these theoretical results could be carried out. The first was published in July of 1991 by Kim *et al.* In that work the authors actually calculated the level energies using a relativistic MCDF method which they

subtracted from the MBPT results of Johnson *et al.* in order to obtain relativistic correlation energies. The correlation energies were then fitted to a power series in Z in order to obtain a smooth correction for this correlation energy. In addition to this, they calculated the QED corrections via three independent approximations in order to compare them which they referred to as the $<r>$ method, the ρ method, and the Welton method[12]. Whereas the ρ and the Welton methods were in close agreement with each other, the $<r>$ method was found to lead to transition energies with poor agreement to experiment, especially at high Z. It was the $<r>$ method, however, that Seely *et al.* had used in their previous comparisons to experiment.

In order to compare the theoretical results to the measured values, a total energy was determined by summing the MCDF energy, the relativistic correlation energy, and the QED correction from the Welton method (in this case it gave results closest to the measurements throughout the range of Z). Kim *et al.* then computed "predicted values" based on the total theory minus the difference between the theory and experiment after adjusting the difference as a function of Z to have smoothly varying first and second derivatives. Comparison of their predicted values to the measured values lead to an interesting conclusion. They noted that experimental values obtained from spectra of laser-produced plasmas had a tendency to be too high in energy as compared to the calculations, while the data obtained from tokamak plasmas were in excellent agreement with their values. A comparison of their calculated and experimental values is shown in Fig.6.1. The tokamak points include data taken at either the Princeton Large Torus tokamak (PLT) or the Texas experimental tokamak

[12] These approximations are only used in the calculation of the screened self energy. For the vacuum polarization they concluded that the correction terms were much smaller than the uncertainties in the screening of the self energy and were, therefore, not included in the total energy.

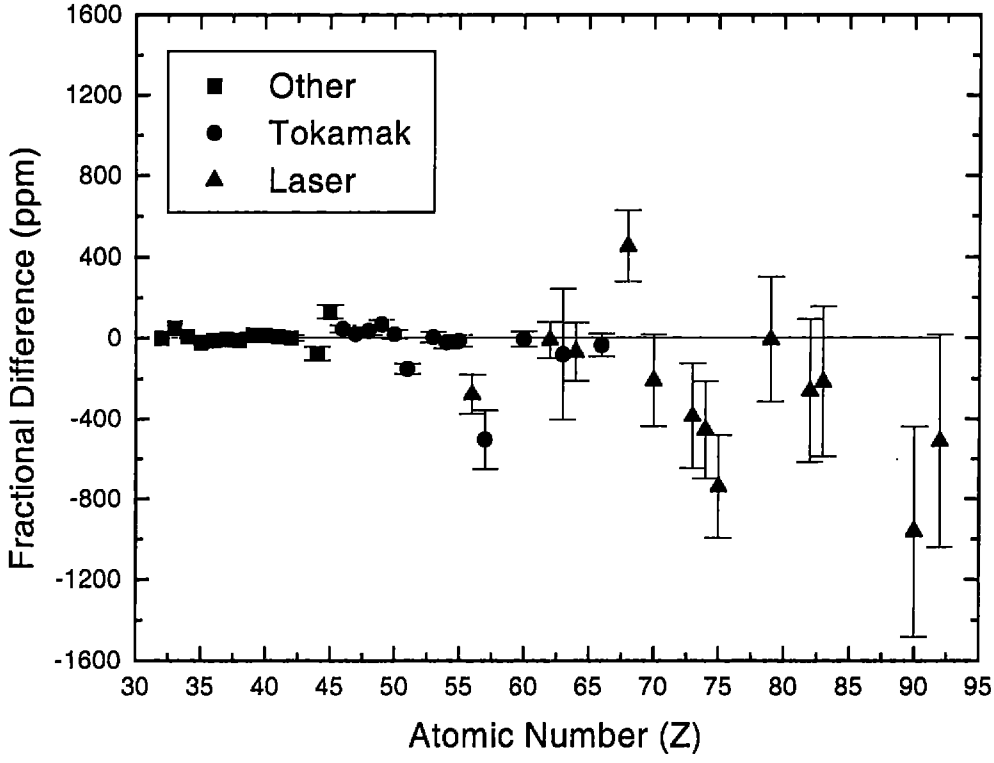

Figure 6.1: Fractional difference between the theoretically predicted and measured values of the energies of the $4s_{1/2} - 4p_{3/2}$ transitions along the Cu isoelectronic sequence. The measurements were made at various sources with those having Z greater than 45 coming from either tokamak or laser produced plasmas. The fractional difference is defined here as $10^6 * \frac{(\text{pred.value} - \text{exper.value})}{0.5*(\text{pred.value} + \text{exper.value})}$.

(TEXT) and the laser points included data from either the OMEGA or NOVA lasers. The noted trend from the spectra obtained at high-Z is obvious.

The second report of calculations of the QED correction terms was published in March of 1993 by Blundell [17]. Unlike the calculations of Kim *et al.*, these were *ab initio* calculations of the screened self-energy and the vacuum polarization. A

comparison of the energies of the $4s_{1/2} - 4p_{3/2}$ transitions as predicted by Blundell and by Kim *et al.* shows that other than for low-Z, the two nearly independent predictions have very similar results, with Kim *et al.* predictions having slightly higher energies. Figure 6.2 shows the comparison of the two theoretical predictions on the same scale as the previous figure. Plotted are the differences (Blundell predictions - Kim predictions) in parts per million for each element. The discrepancy at low-Z is discussed in detail in [17]; regardless, it is below the Z of interest in this work.

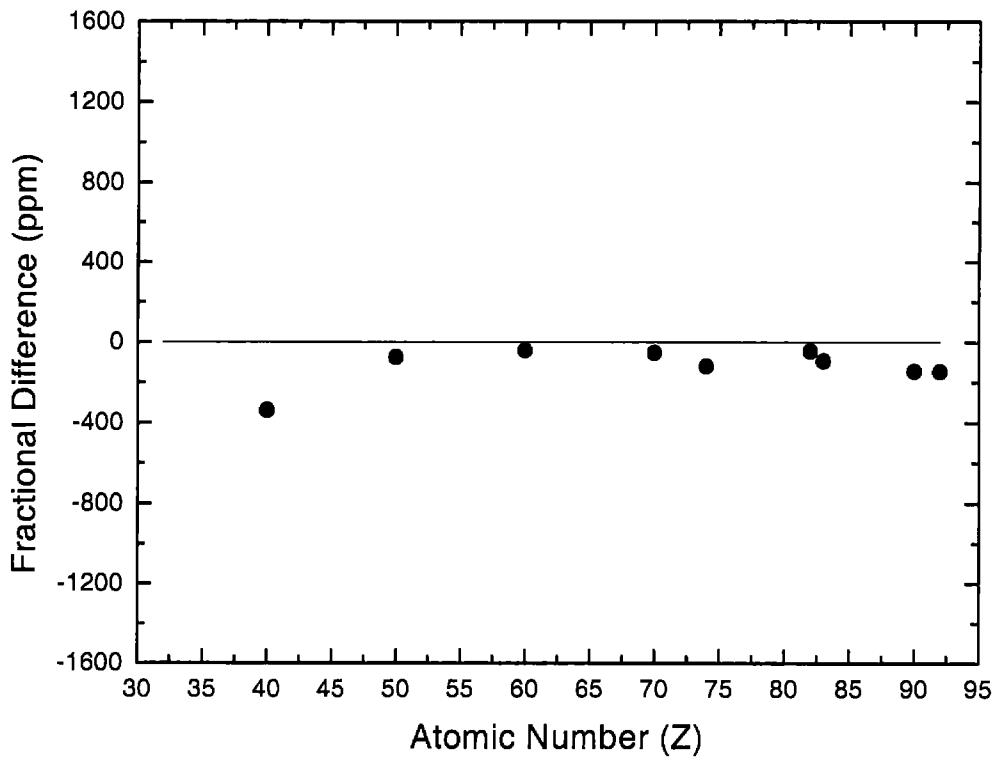

Figure 6.2: Fractional difference between the two sets of theoretically predicted values for the energies of the $4s_{1/2} - 4p_{3/2}$ transitions along the Cu isoelectronic sequence. The fractional difference is defined here as $10^6 * \frac{(\text{Blundell}-\text{Kim})}{0.5*(\text{Blundell}+\text{Kim})}$.

6.2 Wavelength measurements of the $4s_{1/2} - 4p_{3/2}$ transition

Measurements of the wavelengths of the $4s_{1/2} - 4p_{3/2}$ transitions for 6 high-Z elements (Yb, W, Au, Pb, Th, and U) have been made using the same spectrometer system as for the measurements in Ch. 5, that is, using the 2400 1/mm variable line spaced concave grating in the FFS. Each of the measurements was made in a similar manner. The element of interest was injected into EBIT using the MeVVA system with a low-Z element, such as Al or Cu, as the trigger wire. The use of a low-Z element for the trigger wire limited the possibility that spectral features from that element would occur in the same spectral region as the lines being studied. The heavy element was held in the EBIT trap region for a few to several seconds while the energetic electrons from the beam stripped the ions to the desired charge state. Lower-Z contaminants were displaced during the long trapping time as well.

The electron beam energy chosen for each measurement depended on several factors and was optimized for each element. As an example consider the case of Ytterbium (Yb). The energy required to ionize Yb to the Cu-like charge state is 1.99 keV and to the Ni-like charge state is 2.05 keV (A list of ionization potentials relevant to this work may be found in Table A.3, page 122). Since the energy necessary to further ionize the Ni-like state is much higher (3.45 keV), there is a broad energy range available to optimize the Cu-like charge state component. Note, also, that since the ionization of the Ni-like charge state entails breaking into the $n = 3$ shell, the strongest spectral lines associated with this and higher charge states are found at a much shorter wavelength than those of the Cu-like state. This means that the electron beam energy can be raised until the lower charge states (As-, Ge-, Ga-like, etc.) are sufficiently weak, but kept low enough that there is sufficient signal from

the Cu-like state to be detected. This same concept was applied for each ion along the Cu isoelectronic sequence.

One final similarity to be noted in each of the data sets is the method of data accrual. In all cases, the total area of the CCD chip was binned by a factor of four in the non-dispersive direction to create an effective CCD array 256×1024 pixels. Due to minor spectral aberrations, the image of each line is slightly curved at the CCD surface. Simple summing across the dispersion direction would, therefore, artificially broaden the line width. Instead, the files were individually filtered and collapsed into one, three, or eight columns depending on the line intensity and as noted in the descriptions of each element that follow. Each of the sections was independently calibrated, effectively increasing the number of only loosely dependent results[13] by a factor equal to the number of columns. Calibration was performed by determining the central position (in channels) of a number of well known transitions, then fitting these to a 3^{rd}-order polynomial. The background light emission recorded by the CCD was determined by running EBIT with an inverted trap, that is, with the middle drift tube at a higher potential than the top drift tube, so that no trapping occured. Since there is some random noise associated with the readout of each image, even with the trap inverted, several background spectra were averaged and smoothed so that they could be subtracted from the data files before fitting. Then, each of the files was imported into a peak fitting program. Here the *Peak Fit Module* of *Microcal's Origin, version 4.0* was used. The peaks were fit with Gaussian functions of which the peak height, centroid position, and peak area were stored. An example of the

[13]The results are not totally independent since the each of the columns was obtained under exactly identical conditions, and several separate measurements are fitted using the same calibration.

spectra and calibration is shown in Fig 6.3 for the case of uranium. A summary of the results from each of the measurements is found in Table 6.1 at the end of this

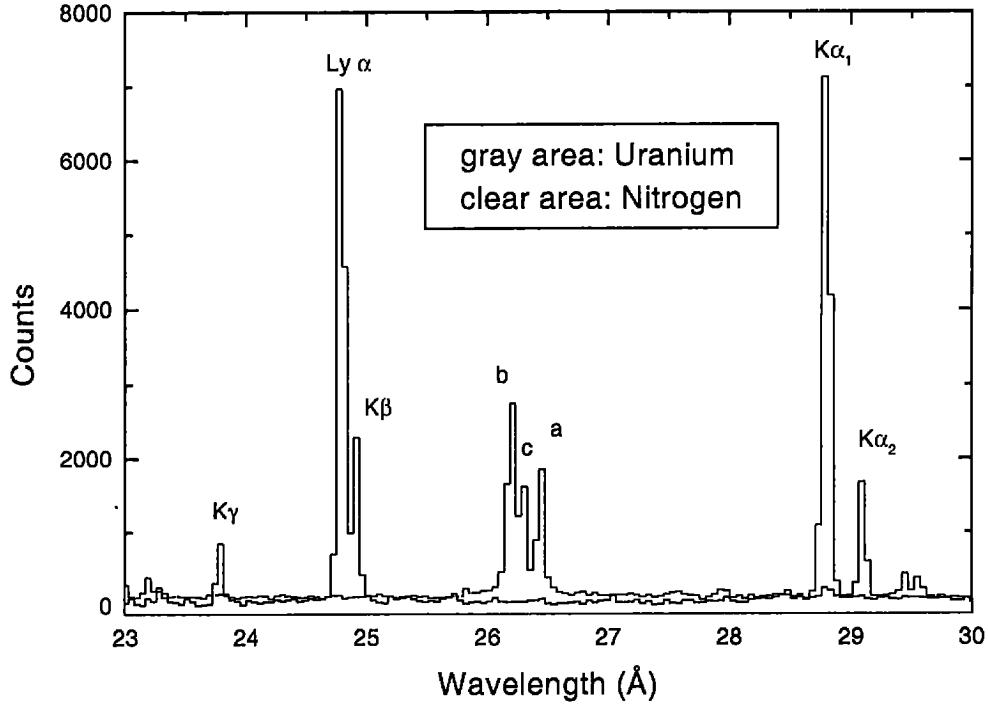

Figure 6.3: EUV spectra obtained with uranium injection (shaded area) and nitrogen injection (unshaded area). The marked N lines are some of those used in the calibration. The lines marked a, b, and c are Cu-like $4s_{1/2} - 4p_{3/2}$, Zn-like $4s^2\ {}^1S_0 - 4s4p\ {}^1P_1$, and a blend of Ga-like $4s^24p\ {}^2P_{1/2} - 4s4p^2\ {}^2P_{3/2}$ and Ge-like $4s^24p^2\ {}^3P_0 - 4s4p^3\ {}^3D_1$, respectively. U was injected with E_{beam} = 6.8 keV and I_{beam} = 113 mA.

chapter (see page 95). A list of all of the calibration lines' wavelengths and limits of precision may be found in Table A.1, page 119.

6.2.1 Ytterbium

Yb (Z = 70) is the lowest-Z element of interest here, and therefore, also that with the longest wavelength. It serves as a useful connection between these measurements and those made of middle-Z elements at tokamaks, which agree well with theory and theoretical trends. In contrast, previous measurements of high-Z (Z $\geq$ 70) elements were all made using the aforementioned laser-produced plasmas and were noted to have a trend of higher energy than predicted. Having a wavelength of near 75 Å, this transition fits well into the optimal range of the 2400 l/mm grating.

Nitrogen, carbon, and neon transitions were used for the calibration of the entire spectral range. Carbon is a normally found in background spectra as a contaminant element so no injection was needed to measure these lines. Nitrogen is also normally found in the background spectra of EBIT, but the intensity was weak enough during this set of experiments so that injection of N_2 gas was warranted. Transitions of hydrogen-like and helium-like carbon and nitrogen in the range of 25 – 40 Å and lithium-like neon transitions from near 56 to 88 Å were used to calibrate the entire spectral range. In all, a total of eleven well-known transitions were used to calibrate the 1024 detector channels and the entire wavelength range covered was determined to be 23.4 - 90.8 Å. Limiting the precision of this measurement was the lack of precise calibration lines near the long wavelength end of the spectrum. The Li-like Ne transitions used in calibration have an uncertainty of 5 mÅ, which added an uncertainty of about 3 mÅ to the calibration in the 75 Å region of the spectrum.

The Yb spectra were made at an electron beam energy, E_{beam} = 2.51 keV, and a beam current. I_{beam} = 57 mA. Each spectrum resulted from an integration of 20 minutes of observation, and for analysis, sets of three spectra were summed. Sufficient

line intensity allowed for each of the sum spectra to be divided into three parallel sections with ranges of CCD columns: a) $5-80$, b) $85-170$, and c) $175-255$. Nine hours worth of observation resulted in twenty-seven measurements of this transition. Neon and carbon calibration spectra were taken in between each two hours of Yb data, whereas the nitrogen was injected before and after the nine hours of Yb injection. The calibration data were separated into two groups with the first 5 hours of Yb data being associated with the first group, and the last four hours with the second. This allowed for a check of any systematic shift of the lines over the course of time – none was found.

As a final check of systematic errors, a transition to the ground state of the Be-like Ne was measured: $1s^2 2s^2\ {}^1S_0 - 1s^2 2s4p\ {}^1P_1$ with an accepted wavelength value of 75.765(5) Å [58]. The wavelength measured using the above method of calibration and six independent measurements was 75.7665(36) Å, where the error in the last two digits listed in parentheses is the statistical deviation of the six measurements. Agreement between the measured and known value is within the statistical limit.

By varying the energy of the beam above and below the threshold to produce the Cu-like charge state, and having knowledge of results from calculations and previous measurements, the $4s_{1/2} - 4p_{3/2}$ transition was identified. Additionally, several lines from lower charge states persisted during these measurements, the strongest of which has been identified as the $4s^2\ {}^1S_0 - 4s4p\ {}^1P_1$ transition from the Zn-like ion. These two, as well as two significantly weaker lines were fit in all twenty-seven sections. Each of these lines was well resolved from the others and had statistical deviations similar to the Be-like Ne line discussed above.

6.2.2 Tungsten

The W measurement has been discussed in detail in Ch. 5, so only a few words about it will be mentioned here. No separate measurement of this line was made. Unlike the other measurements of this transition, for W the electron beam was scanned over a series of energies, both above and below threshold, and all spectra with significant intensity in the Cu-like charge state were used in the analysis.

6.2.3 Gold

One of the easiest elements to inject into EBIT via the MeVVA is Au. As such, the production of intense lines from Au is readily achieved. As before, injections from the MeVVA and gas injection system were alternated, and background spectra were regularly obtained. The Au data, taken at the optimal energy for the production of the Cu-like charge state (E_{beam} = 4.01 keV, I_{beam} = 75 mA), were summed into three data sets. However, the calibration for all of these sets is from a single set of summed data. The intensity of the Au lines and calibration spectra allowed for separation of the spectra into 8 sections to allow for minimal line width and optimal line fitting. The columns summed for each section were: a) 0−32, b) 33−64, c) 65−96, d) 97−128, e) 129 − 160, f) 161 − 192, g) 193 − 224, h) 225 − 256.

The wavelength of the transition in Au, near 48.9 Å, warranted the use of calibration lines between those of the C and Ne. Two transitions to the ground state of Ne-like Ar, having wavelengths of 48.730 and 49.130 Å, respectively, were suited nicely for this purpose. These two lines appeared in the Ar injection spectrum quite intensely, however the wavelengths are known to only ±0.002 Å [59]. This uncertainty increased the error limit of the measurement, but was somewhat compensated for by

use of well known C, N, and O spectral lines in the shorter wavelength region. The entire subtended spectral region was determined to be from 14.6 – 73.0 Å. Varying the wavelength of the two Ar calibration lines by their 2 mÅ uncertainty during the calibration fitting process, an additional uncertainty of 0.4 mÅ was introduced to the measurement of the Au transition.

6.2.4 Lead

Contrary to the easy injection of Au, Pb injection is often more difficult on EBIT, requiring much more time to achieve the same level of statistics. In addition to this, the wavelength of this Cu-like Pb transition coincides with the carbon-edge absorption identified in the intensity calibration of the CCD (see Fig.5.3 on page 59) at 42.4 Å. In fact, the measurement of this Pb transition was repeated a second time after it was found that insufficient injection levels were achieved during the first experimental run to make a precise measurement of the transition. Calibration of the Pb data files was made by fitting known C, N, and Ne lines, as was done for the Yb. The entire spectral range was measured as 23.4 – 90.9 Å. No separation into columns was performed for this data, though several hours of accumulation were summed into each of 9 data sets. Two of the data sets were taken with E_{beam} = 4.53 keV and I_{beam} = 105 mA, the remaining seven sets had E_{beam} = 5.08 keV and I_{beam} = 107 mA. The wavelengths of all of the Pb data were fitted by a single 3rd-order polynomial resulting from the fit of all of the calibration lines. Since the wavelength of this line is close to the He-like C $K\alpha_1$ transition, the uncertainty introduced by the Ne calibration lines was less problematic than was for the Yb.

6.2.5 Thorium

Over the course of completing this set of experiments, a task that spanned some 7 months, conditions in the EBIT chamber varied somewhat. In particular, the level of certain background contaminants and resulting vacuum chamber pressure were at times worse than others. The contaminants are normally light elements such as C, N, and O, but sometimes heavier gases such as Xe are present as remnants of experiments performed by one of the other two groups who regularly operate EBIT. In addition, as with any type of experimental apparatus, unexpected problems occur which must be addressed. These were the case during the measurement of the $4s_{1/2} - 4p_{3/2}$ transition in Cu-like Th. At the time of these measurements, the levels of background C and O were high enough that injection of these elements was not necessary in order to use them for calibration. The injection of N_2 gas resulted in intense spectra with all three of these light elements present. However, this did not impede the progress of these measurements, since light elements are mostly displaced from the trap after several hundred ms by the injected heavy element and the spectral features from C and O do not overlap with the measured Th line.

As for the alluded to "unexpected problems," during the Th measurements the electron beam current was limited by over-heating of the collector. During normal operation the collector, which is used to stop the steaming beam electrons, is cooled with a constant, slow flow of liquid N_2 (LN_2). Over the course of many months of EBIT operation without interruption, the transfer lines carrying the LN_2 from a storage facility to EBIT developed ice blockages, which limited the flow to the collector. The reduced cooling efficiency resulted in the need to operate EBIT at lower currents than otherwise would have been achievable. This problem has since

been corrected and further avoided by regularly warming EBIT to room temperature, thereby melting any blockages.

In spite of the minor problems, the Th results turned out quite well. Six sets of Th data and three sets of calibration lines were collected. Intensities were sufficient for dividing the spectra into eight columns as was done for the Au, resulting in forty-eight measurements of the line position. Adding to the precision of the results is that the position (near 29.0 Å) of the line falls in between the He-like N resonance and intercombination lines at 28.7870 and 29.0843 Å, respectively. As a test of the precision of the fit, residual oxygen lines still present in the Th data were measured. The He-like resonance line of O was measured at a wavelength of 21.6008 ± 0.0059 Å, very close to the precise value of 21.6015 Å and well within the statistical error bar. Hydrogen-like Lyα_1 was measured to be 18.9670 ± 0.0061 Å compared to the calculated value 18.9671 Å, again proving to be quite accurate.

6.2.6 Uranium

The last element in this systematic study was U. Being the heaviest element occuring naturally in significant quantities, the atomic physics of U is of extreme interest. The strong Coulomb attraction between the nucleus and atomic electrons results in a significant overlap of the nuclear and atomic wavefunctions, particularly for high-Z ions of intermediate and high charge states. Injection of U poses no problems for EBIT, and because it is heavier than any other element in EBIT, trapping times of ten seconds or longer allows for the optimization of the Cu-like charge state.

Calibration of the spectra was made with eight known transitions of lines from N and O, only. The spectra had a range from less than 10 to greater than 50 Å. Since

the grating response is no longer focused on a flat plane at wavelengths shorter than around 10 Å, a significant portion of the 1024 channels was out of focus - this portion was ignored in the analysis. The wavelength of the Cu-like U transition is near 26.4 Å, therefore, the N and O lines were sufficient for calibration. Ne-like Ar lines, that were used for the Au calibration, were tested in the calibration of this spectrum and effects from the inclusion of these lines were noted. A difference of less than 0.5 mÅ resulted when comparing the measured wavelength of the Cu-like U line with/without the Ar line included in the fit. However, the uncertainty in the wavelength of the Ar lines limited their usefulness, and it was decided to not include them in the calibration.

Three sets of U data were accumulated for the measurement, all of them calibrated with the same polynomial fit. Two of the sets were obtained at E_{beam} = 6.79 keV and I_{beam} = 113 mA, whereas the third was at a higher energy, E_{beam} = 8.10 keV. At the higher energy, above the ionization potential of the Ni-like charge state, the accumulation rate from the Cu-like charge state was significantly lower, but nearly all of the lower charge state lines were absent. No systematic shift in spectral lines was measured between the data at each energy, suggesting the absence of any hidden line from lower charge states interfering with the measurement. Each of the three sets was separated into eight columns, so, in total, twenty-four measurements were made of the line.

6.3 Error Aanalysis

One of the most important aspects of spectroscopic measurements is to not only report the most accurate results possible, but to adequately account for an error budget, both statistical and systematic. Statistical errors are the easier to understand since there

exist accepted formalisms and proofs leading to an appropriate answer. Systematic errors, however, must be determined from experimental test of parameter variations and cross checks of results. In the following will be shown some of the formalism for the statistical error reported here, as well as a discussion of potential systematic errors.

6.3.1 Statistical errors

The analysis of statistical errors begins with the assignment of an error limit for an individual measurement, σ_i. As was mentioned previously, each of the measured lines - calibration and Cu-like lines, in particular was fit with a Gaussian function[14]. of which the peak center (channel), width (FWHM - channels), and area (total counts in the line) were recorded. The error associated with a single line must be a function of the line shape and the number of counts, N. For a Gaussian, this error is given as $\sigma_i = w(\sqrt{N}/N)$. (A thorough discussion of the derivation of this and other related formulae can be found in numerous books on experimental statistics, such as [60].) Each of the Cu-like lines had at least 3000 counts, usually many more, and FWHM of approximately 1.7 channels. From these, the minimum error for each line is $\sigma_i =$ 0.03 channels.

Each of the Cu-like lines was measured multiple times, the least of which was during the Pb measurement for which 9 measurements were made. The average and error resulting from n multiple measurements are given by $\overline{\lambda} = \sum_{i=1}^{n} \frac{\lambda_i}{\sigma_i^2} / \sum_{i=1}^{n} \frac{1}{\sigma_i^2}$ and $\sigma = \sqrt{1/\sum_{i=1}^{n} \frac{1}{\sigma_i^2}}$, respectively. For the case of Pb, using these formulae results in

[14]For the line fitting the Gaussian function takes the form $y = \frac{A}{w}\sqrt{\frac{4\ln 2}{\pi}} e^{-4\ln 2 \frac{(x - x_c)^2}{w^2}}$, where A is the area, w is the FWHM, and x_c is the x coordinate of the point of greatest intensity.

$\overline{\lambda}_{Pb} = 668.8317 \pm 0.0107$ channels as the measure of the line center. This error is equivalent to 0.0006 Å. More meaningful, however, is a measure of the scatter of the multiple measurements. This total statistical error, not weighted by the number of counts in an individual line, is given by $\sigma_{s.d.} = \sqrt{(n-1)^{-1}\sum(\lambda_i - \overline{\lambda})^2}$. $\sigma_{s.d.}$ is the likelihood that another measure of the same line will end up within this limit. For the test case of Pb, $\sigma_{s.d.(Pb)} = 0.0864$ channels, equivalent to 0.0052 Å. The $\sigma_{s.d.}$ of each measurement is listed in the first set of parentheses for the present measurements listed in Table 6.1.

6.3.2 Systematic errors

Systematic errors are often subtle, requiring checks and cross-checks of data in order to be identified. For this reason several independent measurements of each line were made. When possible, multiple sets of calibration data were used. Measurements were run at various energies in search of lines from other charge states that may skew the peak fitting. Commonly found was a line at slightly shorter wavelength from a lower charge state, as depicted in Fig. 6.4 for the Au data, but this line was easily resolved from the Cu-like line causing no increased uncertainty in the wavelength.

Data taken hours apart were compared to look for temporal shifts of the spectra that might result from fluctuations in the position of the beam or changes that might occur to the spectrometer due to temperature fluctuations in the room · none were found. The only significant systematic error to be noted is in the lack of precision of certain calibration lines. As discussed in the preceding sections, whenever possible only precisely calculated or measured hydrogen- or helium-like transitions were used for calibration. These lines are known to better than 0.001 Å, but, conservatively,

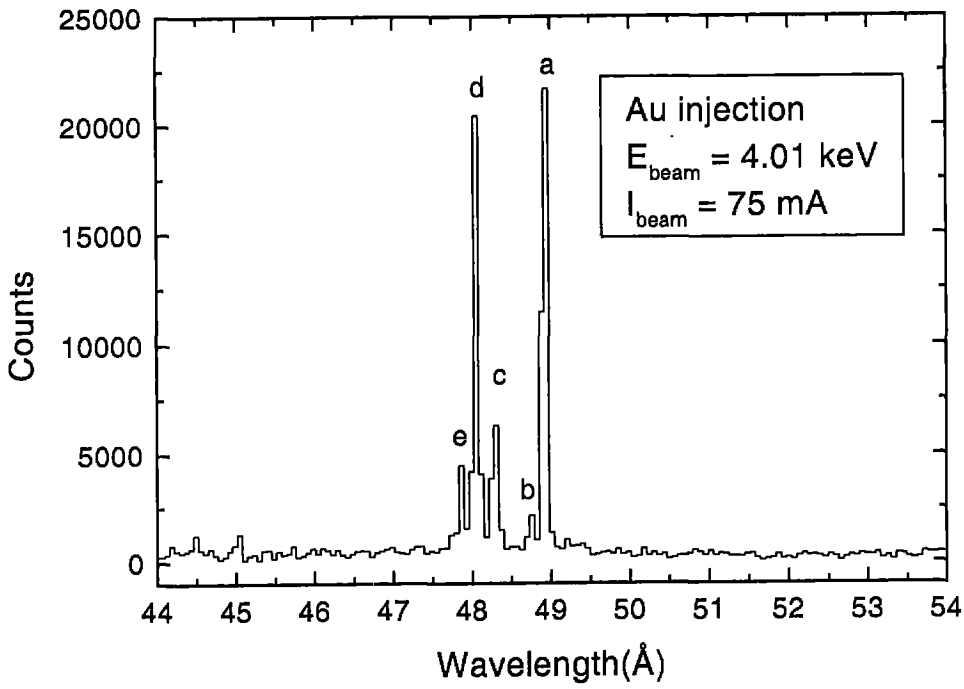

Figure 6.4: EBIT FFS spectrum obtained during Au injection at an energy E_{beam} = 4.01 keV. The alphabetic characters point out: a) Cu-like $4s_{1/2} - 4p_{3/2}$, b) weak transition likely from the Zn-like charge state, c) a blend of Ga-like $4s^2 4p\ ^2P_{1/2} - 4s4p^2\ ^2P_{3/2}$ and Ge-like $4s^2 4p^2\ ^3P_0 - 4s4p^3\ ^3D_1$, d) Zn-like $4s^2\ ^1S_0 - 4s4p\ ^1P_1$, and e) Ga-like $4s^2 4p\ ^2P_{1/2} - 4s4p^2\ ^2P_{1/2}$.

a 1 mÅ systematic error has been assigned to each line due to these calibration line uncertainties. Beyond 45 Å, however, it became necessary to use transitions from the Li and Ne isoelectronic sequences. Increased uncertainty was noted in the text where applicable and added to the systematic error. The total systematic error is listed in the second set of parentheses for the present measurements listed in Table 6.1.

It should be noted that in all cases where it was possible to measure a well-known independent transition, agreement with the known values was much better than these error ranges.

6.4 Summary of results

A summary of the results from this series of measurements, as well as a listing of other measurements and the two theoretical predictions, is given in Table 6.1. All of the wavelengths listed under 'Experimental – Previous' have been taken from laser produced plasma experiments. This is not a complete list of all experimental data, but what is believed to be the previously reported best measurements. The exception is for the lowest-Z element, Yb, for which the value as measured at the NOVA laser is reported at 75.842[15]. Another measurement at the OMEGA laser facility yielded an even shorter wavelength of 75.816[15] Å [62], whereas a measurement made at the PLT tokamak agrees better with the present measurements at 75.85, but with a relatively large error bar of 0.03 Å. A revised version of Fig. 6.1 (page 79) is given now as Fig. 6.5, having removed all of the laser produced plasma results and included the six measurements of the Cu-like $4s_{1/2} - 4p_{3/2}$ transition from EBIT. There now appears to be significant agreement between the measured and predicted values of this transition along the entire range of Z, with the exception of very-high-Z. Although it is impossible to know why the transitions measured from lasers tended to have higher energies than either theory predicted or what was measured at the LLNL-EBIT and the PLT-tokamak, it is plausible that line blends from ions of lower charge states interfered with the proper wavelength interpretation. From the work done on W, reported in Chap. 5, it is evident that intense lines from the

Table 6.1: Summary of the measurements of the $4s_{1/2} - 4p_{3/2}$ transition along the Cu isoelectronic sequence for the 6 ions in these experiments. "Theory - Kim", "Theory - Blundell", and "Experiment - Previous" refer to the predictions and measurements in [16], [17], and [7, 57, 61], respectively. See Sec. 6.1 for details. All values are given in units of Å. The numbers in [] are the errors of the previous measurements as stated in the literature. The value listed for Yb was measured at the NOVA laser facility. Another measurement at the OMEGA laser facility yielded an even shorter wavelength of 75.816[15] Å [62], whereas a measurement made at the PLT tokamak agrees better with the present measurements at 75.85, but with a relatively large error bar of 0.03 Å. The numbers in ( ) are the statistical and systematic error of the present measurements, respectively. Note that the values in [] are an order of magnitude larger than those in ( ). See the text for details.

Cu-like $4s_{1/2} - 4p_{3/2}$				
Element (Z)	Theory Kim	Theory Blundell	Experimental Previous	Experimental Present
Yb (70)	75.860	75.864	75.842[15]	75.8595(24)(40)
W (74)	62.334	62.341	62.304[15]	62.3355(19)(40)
Au (79)	48.929		48.928[15]	48.9280(21)(14)
Pb (82)	42.377	42.381	42.349[15]	42.3740(52)(25)
Th (90)	29.018	29.022	28.990[15]	29.0224(28)(10)
U (92)	26.420	26.423	26.400[15]	26.4325(15)(10)

As-, Ge-, and Ga-like charge states lie between the Zn-like $4s^2 - 4s4p$ and Cu-like $4s_{1/2} - 4p_{3/2}$ transitions. Even with the use of an electron beam with an energy spread of only 50 eV, the measurements on EBIT were not able to fully eliminate the Zn-like charge state and still retain a significant signal from the Cu-like charge state. Laser

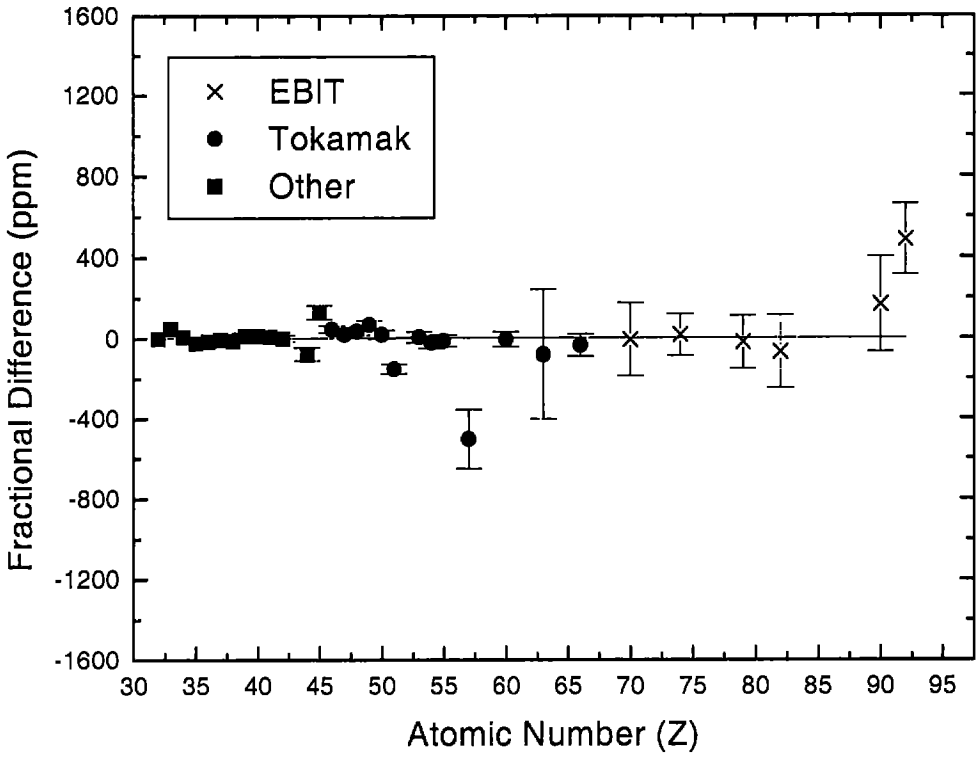

Figure 6.5: Reconstruction of the graph from Fig. 6.1 having removed the laser produced plasma data and introduced the EBIT data from these measurements. Note the significantly improved agreement with theory and the continuation of the trend set by the tokamak data.

produced plasmas do not have the energy resolution of EBIT to comparatively isolate individual charge states, and it is likely that these lower charge states were present in the data used to measure the Cu-like transition. Whenever line blends are present, even if the lines are accounted for and included in the fit, it is impossible to avoid the addition of significant uncertainty. Moreover, should these higher energy lines not be accounted for in the fit, the measured line position of the Cu-like transition would be shifted towards the higher energy end of the spectrum. (A shift towards higher

or lower energy would not necessarily be predictable for the Zn-like case, since it is surrounded on both sides by lines from lower charge state ions. Any shift would have to be addressed in a more systematic way, and likely would depend more critically on the exact plasma conditions.)

As for the slight disagreement between the presently reported value of the U-transition and that predicted by Kim and by Blundell, there are two possible causes. First of all, in any measurement of this type, there is a certain level of statistical fluctuation. It is totally within the precepts of statistical analysis that one or two out of six measurements will be outside of the one-σ error bar. Another factor to weigh is that the effects of quantum electrodynamics become more pronounced at very high-Z and incomplete theories tend to predict transitions that are too high in energy. An independent measurement of this transition in U, or a series of measurements at high-Z with five times better precision, would be required to distinguish theoretical trends from experimental uncertainty.

7 TI-LIKE W^{52+} IN THE NEAR UV

Much has been said to this point about plasma diagnostics from intermediate charge state high-Z ions focusing on measurements in the EUV. Equally important are measurements of transitions in the UV and visible region of the electromagnetic spectrum which may be used to determine plasma parameters. To reiterate what was said in Chap 2, spectroscopic diagnostics in this spectral region, particularly those related to relatively high plasma temperatures, are wanted due to the relative ease of observation and the potential for high precision measurements not achievable in other spectral bands. In low density plasmas, forbidden transitions with lifetimes on the order of milliseconds often appear with a much greater intensity than the more familiar allowed transition.

Feldman, Indelicato, and Sugar predicted the behavior of the M1 transition $3s^2 3p^6 3d^4\ {}^5D_2$-${}^5D_3$ along the Ti isoelectronic sequence to be rather unusual. Their calculations suggested that in ions ranging from Nd^{38+} through U^{70+} the wavelength of this transition would vary only from 3560 to 3200 Å [21]. Typically, transitions along a range as this would span from the IR to the VUV (See Fig. 2.2 in Chap. 2 page 10). Calculations of the $3d^4$ ground state configuration were made using a Dirac-Fock code optimizing each level and with complete core relaxation. Also included was magnetic interaction with full retardation in the Coulomb gauge, screened radiative corrections, and nuclear size corrections. A full description of the calculation is given in their publication.

It should be noted that for $Z \leq 50$, LS designations are most appropriate for the energy levels in the $3d^4\ {}^5D$ ground terms. However, for $Z > 50$, LS coupling becomes

less meaningful in the term classifications, and jj coupling should be used. Nonethe-less, to avoid confusion between designations, and since this transition is between levels differing only in J, the levels will be designated only by their J value with the understanding that these are transitions within the ground term.

For low Z values, the five ground term levels, namely $J = 0, 1, 2, 3, 4$ are predicted to have energies ordered according to their J values, therefore, a magnetic dipole transition from the $J = 3$ state can only occur to the $J = 2$ level. Near Z = 52 a level crossing occurs such that the $J = 4$ level drops below that of the $J = 3$, allowing the latter to decay by an $M1$ transition to either of the levels $J = 2$ or $J = 4$. While the $(2 - 3)$ transition exhibits the unusual wavelength behavior, the $(4 - 3)$ transition behaves in a more usual manner having transition wavelengths in the IR near the level crossing and rapidly moving into the VUV by Z = 74. As the atomic number increases beyond 52, the branching ratio of decay from the $J = 3$ to each of the other two states also changes dramatically. The predicted branching ratio for several elements along this sequence are listed in Table 7.1. At Z = 74 only 16% of the transitions from $J = 3$ should decay into the $J = 2$ state. Furthermore, at very high Z the transition becomes very weak and, hence, is less likely to be useful as a possible diagnostic.

7.1 Measurement of the ground term $J = 2 - 3$ transition of Ti-like W

Since the publication of the calculations of Feldman *et al.* some measurements of the ground term $J = 2 - 3$ transition of Ti-like ions with Z = 54 – 64 have been reported which differ from theory by about 200 Å [23, 63, 64, 65]. The only measurement with

Table 7.1: Calculated branching ratio for the $M1$ transitions A: $J = 2 - 3$ and B: $J = 4 - 3$ in the ground configuration along the Ti isoelectronic sequence. The branching ratio is defined as $A/(A - B)$ [21].

Branching Ratios	
Element (Z)	Branching Ratio
Xe (54)	100%
Nd (60)	77%
Tb (65)	43%
Yb (70)	24%
W (74)	16%
Pb (82)	9%
U (92)	5%

an ion beyond the point which the $J = 4 - 3$ transition dominates the branching ratio was recently made with Au at the LLNL-EBIT using a moderate resolution normal incidence reflection grating spectrometer [66] -- a precursor to the present high precision measurement. To complete the test of theory and to provide a benchmark value on which future measurements and theory can rely between the previously measured values, a high-resolution measurement of the $J = 2 - 3$ transition of Ti-like W was made. As was stressed earlier, W in itself, is of particular interest as this material is used in divertors and other mechanical elements exposed to the plasma.

Paramount to the completion of this measurement was the development of the transmission grating spectrometer described in Chap. 4.[15] The transmission grating

[15]The spectrometer was originally designed and constructed in 1998 for the measurement of the

spectrometer combines extreme precision and optimal collection efficiency in the near UV and visible. The wavelength of the Ti-like transition predicted by Feldman *et al.* was 3546.1 Å; however, each of the previous measurements of other elements determined wavelengths on the order of 5% longer than predicted. Therefore, the spectrometer was set up to scan the range from 3430 to 3880 Å in search of the line.

One of the difficulties of using the TGS was the set-up and focus of the optical system. Being designed for dispersion of laser light, the flat, quartz grating wants the incoming light to be parallel. This, of course, requires the precise alignment of the focal point of the "collection lens" with the center of the electron beam inside of EBIT. The standard technique of autocollimation was not applicable, because the light source is both too weak and also inside the UHV vessel, not yielding any way to observed retroreflected light. In a two-lens system, though, focus at the detector can be achieved for any source/first-lens distance by appropriately moving the second lens. Thus, to achieve parallel light between the lenses requires more than just acquiring a satisfactory focus at the detector. Instead of using the "focusing lens", it was temporarily removed from the system and replaced with a commercial UV camera objective. (The shutter on the detector is also capable of supporting standard *Nikon* lenses to focus on the CCD.) This objective was set to focus parallel light (focus ∞) onto the detector plane. The collection lens was then adjusted until the best focus was achieved. Afterwards, the camera objective was removed, and the transmission grating and focusing lens were put in place. Next, the position of the second lens was adjusted until a good focus was achieved at the center of the detector. As a final

hyperfine transition in H-like Tl near 3800 Å - a measurement requiring extreme precision and optimal collection efficiency. Due to catastrophic failure of the SuperEBIT vacuum system in 1998, the use of this spectrometer was re-directed towards other measurements.

adjustment, the detector was rotated until the best focus was obtained across the entire spectral range of the detector.

The next obstacle to overcome was the calibration of the spectrometer system. Since the optical system is composed of four independent, free-moving parts (2 lenses, 1 grating, 1 detector) mounted on a table only loosely fixed to EBIT, the calibration must be *in situ*, and must be performed each time the spectrometer is set up. Calibration using external sources, such as standard spectral lamps shining though a port opposite to the spectrometer, is quite difficult and has the possibility of adding additional systematic errors. Known lines in the UV/visible emitted from highly charged ions within EBIT are uncommon and do not have the precision and accuracy required for calibration. There is, though, a third option. One of the byproducts of gas injection, other than providing ions to be trapped, is that atoms streaming through the chamber and passing through the electron beam have a good chance of collisions with beam electrons and still not becoming trapped. The collisions may strip one to a few electrons from the atoms while leaving the remaining atomic electrons possibly in an excited configuration. These electrons can then make fast transitions to lower states, many of which are in the range of this spectroscopic system. The spectral lines from these low-charge state ions appear at the CCD detector regardless of whether the drift tube trap is set or not. By raising the potential of the middle drift tube to a higher value than the top drift tube, spectral features from low charged ions can be distinguished from those of highly charged ions. This is called "inverting the trap" and has proven to be very helpful in spectral charge state identification. Since no trapping and further ionization occurs, the spectrum is fairly independent of the beam energy permitting the energy, and therefore, the current, to be run at relatively

high values enhancing the line intensities. A further distinction between these two 'types' of ions is the length of the spectral feature. Whereas trapped ions oscillate between the top and bottom drift tubes, thereby imaging the entire electron beam in the trap region, un-trapped ions simply emit light from the portion of the beam through which the gas jet intersects. Figure 7.1 is a cartoon representation of two possible scenarios. The first case (A) shows the normal situation of an applied trap potential; (B) represents an inverted trap so that none of the ions are bound to travel along the axis of the electron beam.

Identification of lines emitted from low charged ion stages for calibration is one of the keys the TGS precision results. Precise measurements of such lines has been performed for many years utilizing sources designed for low charge state ion production such as spectral lamps and vacuum spark plasmas. Using these sources, values for the wavelengths of these transitions have been well established. For the present measurements Ne and Kr were used as the calibration sources. Figure 7.2 shows the spectra of un-trapped Ne and Kr resulting from many hours of summed data for gas at single position of the CCD translation stage. The strongest lines are mostly from the singly-charged states of the respective elements. The arrows (↓) in the figure point out the 11 lines that were used to calibrate this section. The weak features in the Ne spectrum between 3580 and 3620 Å, identified as lines from neutral Ne, are insufficiently intense to be used for calibration. Kr injection provided a wealth of lines throughout the 135 Å bandpass of the measurement. Again, most of the stronger lines are singly-ionized, though two of those marked with arrows are identified to come from doubly-ionized ions. Table A.2 in Appendix A lists the wavelengths and ionization stages of all of the calibration lines.

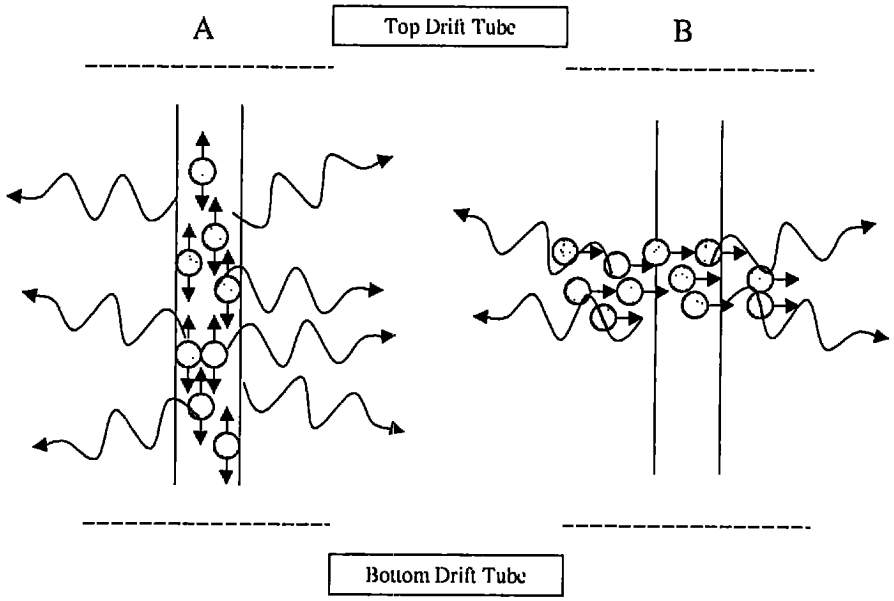

Figure 7.1: A and B represent two situations resulting in photon emission from the region of the electron beam. In A, the ions (dark circles), injected by either the MeVVA or the gas injector, are trapped by the applied potentials of the drift tube and the space charge of the electron beam (shaded region). Photons may be emitted anywhere along the electron beam between the top and bottom drift tubes. B represents the case of an inverted trap. Atoms injected by the gas injector stream through the electron beam where they can be collisionally excited and/or ionized, but not trapped. Photons can only be emitted in the overlap region of the cylinder of atoms and the electron beam.

The production of the Ti-like charge state of W occurs in the range of energies that is optimal with EBIT. The electron beam energy necessary to create the Ti-like charge state - 22 remaining bound electrons - is 4.72 keV [67], an energy at which currents of 130 mA or more are normally achieved. To search for the line, EBIT was set to an electron beam energy E_{beam} = 4.86 keV and current I_{beam} = 130 mA. The MeVVA was loaded with a W cathode and Cu trigger wire. The detector was set

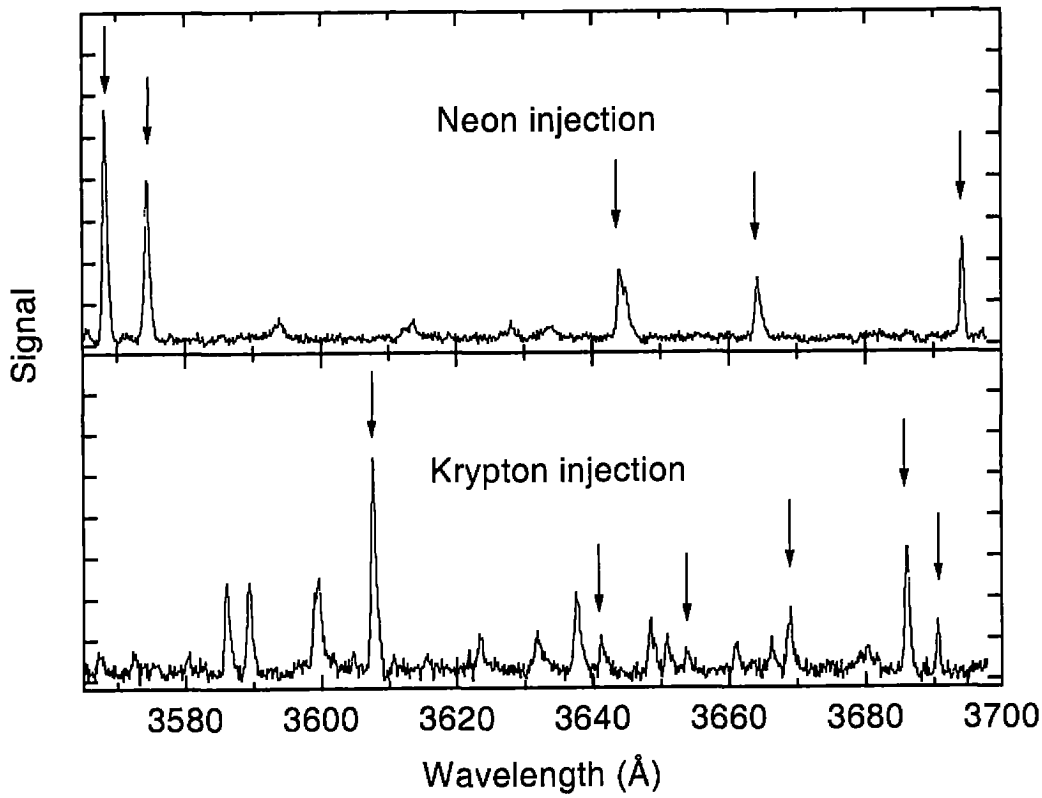

Figure 7.2: Sum of data accumulated during injection of neon and krypton. For both cases EBIT was operated with an inverted trap so that no highly charged ions were formed. ↓ indicate lines that were used in the calibration. Many of the unmarked lines, particularly in the Kr spectrum, are unidentified in the standard reference tables. They are likely to be from doubly- or triply-charged ions of Kr. Some of these lines, for instance, the Kr line at 3586 Å, are significantly enhanced when the trap is turned on suggesting they may be from an even higher charge state.

to the longest wavelength setting - such that the longest wavelength impinging the detector was about 3880 Å. The detector accumulated signal for 20 minutes at a time, was then moved by half of its width towards shorter wavelengths, and started again. In this way the entire spectral region, except the longest and shortest extrema, was

observed twice. Only one line was detected in the band spanning down to 3430 Å. The disappearance of the line after lowering the beam energy below that necessary to create the Ti-like charge state and the relatively close agreement of its wavelength with the theoretical treatment by Feldman *et al.* verified its identification as the $J = 2 - 3$ transition. The electron beam energy was then adjusted until an optimal count rate was achieved in the line. Data was accumulated for many hours, alternating the W-MeVVA injection with either the Ne or Kr gas injection. Figure 7.3a shows the signal from the CCD plotted along the calibrated wavelength axis. The wavelength was measured to be 3627.13 Å with a FWHM of 1.32 Å.

Of interest from the viewpoint of plasma diagnostics is not only the wavelength of the transition, but its behavior, or more specifically, its count rate as a function of electron beam energy. Figure 7.3b displays the count rate (counts/20 minutes) as a function of the total beam energy, taking into account the sum of the applied potentials minus the space charge of the electrons in the beam. This W transition samples electrons with energies in the range of $5 \cdot 6$ keV, having a peak intensity corresponding to a beam energy of 5.5 keV. Due to the typically Maxwellian-shaped electron temperature distribution in a tokamak plasma, the line should be detectable in plasmas with peak tempertures of roughly 3 – 8 keV.

Methods of statistical analysis of spectral lines were discussed in some detail in Chap.6. The same principles can be applied here. Multiple measurements of the same line under various conditions were made. Each of the lines contains a statistically significant number of counts. Using a purely statistical approach, the error in each measurement amounts to about 0.051 channels, or equivalently, 0.0071 Å. However, the scatter of the various measurements was larger, the standard deviation of the fits

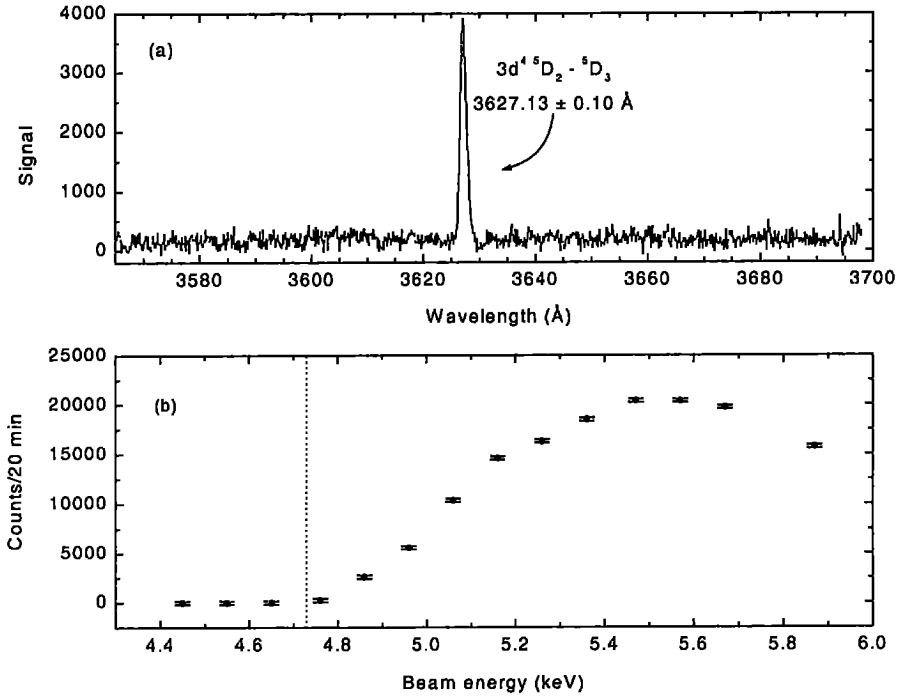

Figure 7.3: (a) Spectrum from a single setting of the TGS from 3565–3700 Å. The single line, the only one detected in the spectral band from 3430–3880 Å, is identified as the Ti-like W ground level $J = 2-3$ transition. (b) The total number of counts above background collected by the spectrometer per 20 minutes as a function of electron beam energy. As was true in the previous chapters, these energies have incorporated applied potentials to the drift tube assembly and the middle drift tube, and an estimation for the space charge. The energy necessary to create the Ti-like charge state is 4.72 keV (dotted line in figure). The line is most intense at a beam energy of 5.5 keV.

being 0.72 channels – about 0.10 Å. The majority of the calibration lines are known to better than 0.01 Å and, therefore, add no significant adjustments to the error budget.

A word should be said about the 0.72 channel scatter of the various measurements. There are several factors that, in principle, could contribute to such a scatter: the

shifting of the electron beam within EBIT, movement of the entire optical system during the measurement, or shifts of the spectral lines due to "bad-pixel filtering" during data analysis. The TGS optical system produces a one-to-one image of the electron beam at the detector, therefore, a shift of 1 channel at the detector would be caused by the translation of the electron beam by 25 μm. However, systematic studies of the stability of the electron beam, carried out as part of this thesis, have shown that by running steady state there is no measurable shift in the electron beam's position [28]. The beam's position has been shown to change slightly as the beam energy is changed (about 6 μm max.), but only with changes in energy that required the re-tuning of EBIT. Throughout these measurements, no re-tuning was required. Additionally, many other high-precision experiments previously performed on EBIT would have detected similar shifts of an un-stable electron beam.

Movement of the spectrometer system is a second possibility. This movement would have to be traced to some sort of external interaction. The optical table is rigidly mounted to its stand, which in turn, is bolted onto the concrete floor, reducing the possibility of motion due to vibrations or accidental bumping. The internal components are also rigidly attached to the table making even slight movements unlikely. However, thermal expansion of the optical table resulting from temperature fluctuations in the room may have a significant effect. A temperature change in the EBIT-II laboratory room of 1 to 3°C throughout a twenty-four hour period has been found to be common. This is particularly significant since meausurements at EBIT are performed day and night. An analysis of the spectrometer's geometry, using the coefficient of linear expansion for the aluminum optical table, has estimated the thermal shift to be approximately 4 $\mu m/^\circ$ C.

The third possibility is that during the CCD pixel filtering process (*i.e.* removal of cosmic rays from the data) the center position of the fitted spectral lines may be shifted. The CCD detector used in the TGS is controlled by a different software package than that used by the FFS (otherwise, the detectors are identical). This newer software includes a function used to remove the cosmic ray spikes, whereas the filtering of the FFS images is performed using software written by this author (see Appendix C). The commercial software detects the bad pixels only by comparing the counts in each pixel to a user-supplied cut-off percentage variation from the local median. It then replaces the value of the bad pixel with the average of the surrounding pixels, which possibly can lead to broadening, or shifting of the resulting line position. "Cosmic rays" affect approximately 400 out of the 260,000 binned pixels (0.15%) during a normal 20 minute exposure. The W line is contained on a section of $\sim$ 2400 – length $\times$ 2*FWHM – binned pixels amounting to, on average, less than four bad pixels in the W region per exposure. To look for any shift resulting from filtering, several spectra were filtered using various levels of "cut-off." With no filtering, the spectral line could not be adequately fitted by a Gaussian, but very low levels of filtering eliminated enough of the severe points for good fitting. It was found that as the level of filtering was increased, small shifts in the line position were measured, but only on the level of less than 0.1 channels, more often, much less than this. Noted, however, was a broadening of the lines to the order of 5%. This is not surprising since the bad pixel replacement value is an average of neighboring pixels. A 5% broadening should have no deleterious effects on the line position.

From the above considerations, it can be concluded that thermal shifts are the most likely cause of the roughly 18 μm scatter of the measured line positions noted in

the analysis. Future measurements will have to address this issue if better precision is to be achieved. There are several possibilities to improve the precision. Thermal stabilization of the optical table could eliminate the majority of the scatter. Monitoring the temperature of the room in the vicinity of the spectrometer during the data acquision would allow for "post acquisition" shift adjustment. A third possibility would be frequent calibration (every two hours) so that the effect of the shift can be minimized. This would be effective since the temperature changes occur over many hours.

7.2 Results

Measurements of the Ti-like ground state $J = 2 - 3$ $M1$ transition have been previously made by groups at various EBITs world-wide including NIST, Oxford, and Tokyo for elements in the range Z = 53−64. These mid-Z elements are important and showed that the trends predicted by Feldman *et al.* were generally correct. Measurements at higher Z are required to make the measurement of this transition useful for higher plasma temperatures. Figure 7.4 shows a summary of all of the reported EBIT work on the same scale as the Feldman predictions. The solid line connecting the predicted values, a spline fit to the points, elucidates the trend towards Z-independence of the wavelength between Z = 60 − 75. Though still showing somewhat of a plateau, the experiments have revealed a greater dependence on Z throughout the region. It, therefore, appears possible to positively identify the elemental source of such lines in a plasma unambiguously, even with a modest resolution spectroscopic system. The wavelength trend is, none-the-less, sufficiently stable in the UV so that the line may be used as a diagnostic as described before. Beyond a Z of 80, the theory is still

untested, and may prove to drop more sharply than predicted. Measurement of this transition at higher Z may prove challenging since the branching ratio to the $J = 2$ state decreases significantly.

Since the time of the first measurements of this transition, some new theoretical predictions of the wavelengths have been made. Along with their reporting of the measurements of this transition in Nd^{38+} and Gd^{42+}, Serpa *et al.* used the measurements to adjust atomic parameters and calculated "improved wavelengths for all such $M1$ transitions between Xe (Z = 54) and Os (Z = 76)" [63]. For W^{62+}, they predicted that the scale factor to would be 1.0, that is, the W line would occur at the wavelength predicted by their own MCDF calculations – 20 Å shorter than what was predicted by Feldman *et al.* Just after the first measurements were reported and about the time that the "scaling" predictions were made, an attempt was made by Indelicato to improve the original calculations by including retardation to all orders, making the magnetic interaction self-consistent, and by doing MCDF calculations with a larger basis set using both valence-shell and core correlations, but better agreement with the measurements was not achieved [68]. It was concluded that these "improvements" affected the $J = 2$ and the $J = 3$ states equally. Subsequent to this report, Beck *et al.* performed *ab initio* calculations of the $J = 2 - 3$ energy difference [69]. Though this work resulted in better agreement with the previously measured transitions (to within 1.5%), no predictions were made toward elements of higher-Z, or even for any element not previously measured. However, very recently theoretical predictions have been made by Kato *et al.* which promisingly come close to this measured value for tungsten [70]. Their predicted value of 3625.7 Å is only 1.4 Å shorter than what is measured and improves the accuracy of predictions by nearly two orders of magni-

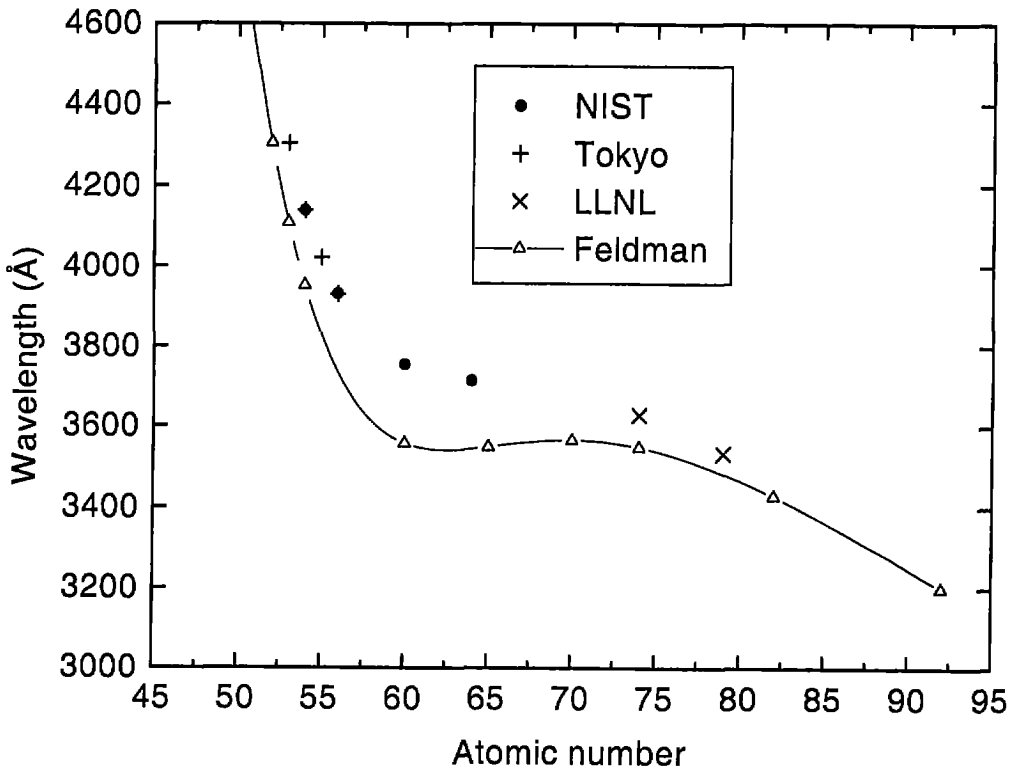

Figure 7.4: Comparison of the wavelengths of the Ti-like $J = 2 - 3$ ground state transition predicted by Feldman *et al.* and measured at various EBITs. △ represent the elements for which the predictions were made and the solid line is a fit to those points emphasizing the trend of wavelengths; • mark the measurements reported by the NIST EBIT group; + depict the points measured at the Tokyo EBIT; × show the two measurements from the LLNL EBIT at highest Z. Not shown is a measurement from the Oxford EBIT of the transition in Ba (Z = 56) which agrees with the other two reported measurements. The error for each of these measurements is much smaller than the relative size of the markers.

tude. The close agreement to the measurement suggests that the new calculations may well fill the void of unmeasured elements between Gd and W. It would still be

interesting and useful to continue such measurements at even higher Z. Since these transitions should be weak due to the competition of the $J = 4 - 3$ transition, the success of these measurements will depend even more on the use of high-efficiency optics.

8 SUMMARY

8.1 Results

This work has successfully described several new measurements of interest for plasma diagnostics and measurements of radiative losses from heavy impurity ions of a variety of plasma sources focusing, however, on those related to tokamak/fusion plasmas. The first part of this dissertation has provided a complete description of the experimental facility, the electron beam ion trap, used to supply a source of ions with selectable ionization stages. The design of two new spectrometers has also been thoroughly described, each capable of high-resolution, time integrated measurements over a broad spectrum and each making use of sensitive CCD detectors. The EUV flat-field spectrometer uses either of two commercial, variable-line-spaced, concave, grazing-incidence, reflection gratings to provide spectral access from 10 to greater than 300 Å. The spectrometer vacuum housing includes *in situ* focus adjustment and a differential pumping system. Having the diffracted photons impinge upon the detector at normal incidence produces improved collection efficiency over the usual grazing-incidence collection inherent of typical "Rowland circle" based spectrometers. The other system, the high-efficiency, high-precision, UV/visible spectrometer, uses a large (6″ diameter) quartz, transmission grating manufactured at LLNL as the dispersive element. Together with a set of two matching $f/4.6$ achromatic lenses, this system can be used for precision spectral analysis from wavelengths less than 3000 to greater than 5000 Å.

Measurements of W in the spectral range of 40 – 85 Å have been known to be useful to the determination of plasma conditions and impurity concentrations in tokamaks. In fact, Asmussen *et al.* [12] used a measurement of the total tungsten radiation obtained from bolometric measurements, and calculated radiation losses to attain a value for the impurity concentration of W in the ASDEX Upgrade tokamak experiment. Spectroscopic observations of a quasi-continuum structure intensity near 50 Å were shown to provide a more sensitive impurity probe. Additionally, comparisons of the intensity of isolated lines from intermediate charge states were compared to calculated results, from which the W concentration at the core of the plasma was determined. Each of these measurements relied upon theoretical predictions of wavelengths and/or intensities as a critical part of the analysis. The present work provides a needed systematic experimental check of the theoretical work. It has been shown that the atomic structure theory used by Fournier [13] provides reasonably accurate wavelength predictions. In all cases the predicted wavelengths agree within about 1 Å of the measured lines. Even better agreement was found for transitions with only a few electrons outside of the closed $n = 3$ shell. Since the relative concentrations of each of the ionic stages of W could not be independently determined, no measure of the intensities between charge states was possible. However, the relative intensities of each of the lines from the same charge state is also provided in the tables in Chap. 5, where the intensity is given as a ratio of the fitted area of the line to the fitted area of the strongest predicted line. Some disagreement is noted between the predicted and the measured relative intensities. In particular, the ratio of the intensities of the $4s - 4p$ and the $4p$ -- $4p$ to the $4p - 4d$ transitions differs by about a factor of two. Several possibilities for the difference have been investigated including precise mea-

surements of the spectrometers efficiency as a function of photon energy, improved calculations using parameters more similar to EBIT than tokamak (e.g. narrow electron beam energy spread), and more complete calculations including recombination. Each of these issues will need to be addressed if the relative intensity is to be known to better than a factor of two.

Through a series of precise measurements of the $4s_{1/2} - 4p_{3/2}$ transition along the Cu isoelectronic sequence, critical comparisons have been made of some of the best theoretical predictions of the energies of transitions within ions having a large number (29) of bound electrons. This same transition has previously been systematically studied though a series of experiments using laser produced plasmas as a source of high-Z (Z = 70) ions and tokamak plasmas as a source for mid-range (Z = 40 to 70) elements. At the cross-over between these two types of source there had been noted to be a shift in the trend of the measured transition energies. That is, measurements made using the tokamak plasma source match very well to theory, while the laser produced plasma results are mostly at higher energies than theory predicts. Six high-Z elements spanning the upper portion of the periodic table were chosen to be used to make a set of systematic precision measurements of this transition using the flat-field EUV spectrometer with the Livermore EBIT. These results exhibit very good agreement with the theory of Johnson *et al.* [15] after QED corrections of either Kim *et al.* [16], using a semi-empirical method, or Blundell [17], who made *ab initio* calculations are added. The precision achieved for each of these EBIT measurements is better than 8 mÅ. A slight divergence of the EBIT measured values from theory at Z $\geq$ 90 suggests that refinement of the theory might still be necessary, especially since it is noted in the paper of Kim *et al.* that for Z $\geq$ 90 new parameters for the

nuclear size were used. An independent measurement of this transition with precision better than 1 mÅ would also serve to validate these measurements.

One of the most useful spectroscopic diagnostics of a plasma is an isolated, intense transition in the visible or near UV. Such a line can be used to measure the bulk plasma motion (the Doppler broadening is measurable from the Gaussian width), the ion temperature, and magnetic field strength (Zeeman effect). As such, forbidden ($M1$) transitions fulfill an important role in the diagnosis of high-temperature plasmas. Through a survey of ions with ground terms of the type $3s^2 3p^6 3d^l$, Feldman, Indelicato, and Sugar identified a transition in the ground state of Ti-like ions ($3s^2 3p^6 3d^1$) which has an unusual behavior: the $J = 2 - 3$ transition wavelength is nearly independent of Z over a broad range of ions [21]. Subsequent measurements from elements near the lower end of this range of Z at the NIST EBIT yielded results that were close to (about 200 Å longer than) the predicted wavelengths. A single measurement at the high-Z end of the range (Au, Z = 79) from the LLNL EBIT showed that this difference was reduced to less than 50 Å; but there still remained a gap between this point and the next highest-Z, Z = 64, the point where the J = 4 – 3 transition begins to dominate the J = 2 – 3 and the predicted "flatness" of the transition energy function is most pronounced. In this work has been presented a measurement of this transition from W, an element of special interest to tokamak plasmas. This high precision UV measurement identified unambiguously the wavelength at 3627.13 ± 0.10 Å, about 80 Å longer wavelength than the calculations of Feldman *et al.* predicted. Having an ionization energy of 4.7 keV, this Ti-like W transition should be strong in plasmas with 5-6 keV electrons. New calculations by Kato have achieved agreement with this measurement to a level of better than 2 Å.

8.2 Suggestions for future research

There is much research still to be done on EBIT in terms of EUV and UV/visible spectroscopy. The following are suggestions for measurements related to the present work.

- Most importantly, a calibration of the EUV spectrometer's response as a function of energy should be made. This requires resources, such as a calibrated light source, outside of the EBIT facility such as could be provided by synchrotron radiation. Plans are currently under way to make such measurements during the first half of calender year 2000 at the Lawrence Berkeley Laboratory Advanced Light Source (ALS).

- In order to be able to study fine details of the QED calculations, the Cu-like measurements could be preformed at higher resolution. This would also be necessary in order to know better the total QED effects at high-Z. However, this requires a new spectroscopic system with greater resolving power and/or a CCD (or other type) detector with at least 5× smaller pixel size.

- The measurement of the Ti-like transition for W filled a void in the experimental data to show the predictions of a slowly varying energy for this transition as a function of Z are more or less correct. As plasma temperatures become hotter, it would be useful to know the trend of the wavelength at the high-Z end of the periodic table. Therefore, it would be useful to make measurements of the transition in several more elements, such as Pb, Th, and U. These measurements could easily be done with instrumentation currently available for use on EBIT-II.

A TABLES OF LINES AND ENERGIES

A.1 Calibration Lines

Table A.1: Lines used in the calibration of the flat-field spectrometer spectra described in this work. The values for hydrogen-like ions were calculated by Johnson and Soff [71]; the helium-like lines are taken from the calculations by Drake [72]; the Li-like Ne wavelengths come from Tondello and Paget [58]; and the Ne-like Ar were measured by Phillips and Parker [59]. Wavelengths marked with an * come from measurements by Edlén [73]. Many of these lines also have been tabulated by Kelly as found in [74]. Values listed for the hydrogen-like and helium-like have an accepted accuracy of at least ±1 in the last digit listed; measurements for the Li-like Ne claim to be good to ±5; while for the case of Ne-like Ar the reported accuracy is ±2. (See table on next page.)

FFS Calibration Lines

Element (Z)	Ion Type	Identification	Wavelength (Å)
C	H	$1s\ ^2S_{1/2} - 2p\ ^2P_{1/2}$	33.7396
		$1s\ ^2S_{1/2} - 2p\ ^2P_{3/2}$	33.7342
	He	$1s^2\ ^1S_0 - 1s2p\ ^1P_1$	40.2680
N	H	$1s\ ^2S_{1/2} - 2p\ ^2P_{1/2}$	24.7846
		$1s\ ^2S_{1/2} - 2p\ ^2P_{3/2}$	24.7792
		$1s\ ^2S_{1/2} - 3p\ ^2P_{3/2}$	20.910*
	He	$1s^2\ ^1S_0 - 1s2p\ ^3P_1$	29.0843
		$1s^2\ ^1S_0 - 1s2p\ ^1P_1$	28.7870
		$1s^2\ ^1S_0 - 1s3p\ ^1P_1$	24.898*
		$1s^2\ ^1S_0 - 1s4p\ ^1P_1$	23.771*
O	H	$1s\ ^2S_{1/2} - 2p\ ^2P_{1/2}$	18.9725
		$1s\ ^2S_{1/2} - 2p\ ^2P_{3/2}$	18.9671
	He	$1s^2\ ^1S_0 - 1s2p\ ^3P_1$	21.8036
		$1s^2\ ^1S_0 - 1s2p\ ^1P_1$	21.6015
Ne	Li	$1s^22s\ ^2S_{1/2} - 1s^23p\ ^2P_{3/2}$	88.092
		$1s^22s\ ^2S_{1/2} - 1s^24p\ ^2P_{3/2}$	67.382
		$1s^22s\ ^2S_{1/2} - 1s^25p\ ^2P_{3/2}$	60.796
		$1s^22s\ ^2S_{1/2} - 1s^26p\ ^2P_{3/2}$	57.747
		$1s^22s\ ^2S_{1/2} - 1s^27p\ ^2P_{3/2}$	56.043
Ar	Ne	$1s^22s^22p^6\ ^1S_0 - 1s^22s^22p^53s\ ^1P_1$	48.730
		$1s^22s^22p^6\ ^1S_0 - 1s^22s^22p^53s\ ^3P_1$	49.180

Table A.2: Wavelengths of the lines used in the calibration of a single setting for the TGS. The third column shows the state of the ion: II – singly-charged; III – doubly-charged. The lines are listed in order of increasing wavelength. The precision of each line is better than ±1 in the last digit shown. The single wavelength marked by the * is the weighted average of an unresolved blend of two lines. Each of the other lines appears well resolved. These wavelengths are taken from the National Bureau of Standards compilation *Wavelengths and Transition Probabilities for Atoms and Atomic Ions, Part 1* [75].

TGS Calibration Lines

Element	Wavelength (Å)	Spectrum number
Ne	3568.50	II
Ne	3547.47*	II
Kr	3607.88	II
Kr	3641.34	III
Ne	3643.93	II
Kr	3653.928	II
Ne	3664.07	II
Kr	3669.01	II
Kr	3686.182	II
Kr	3690.65	III
Ne	3694.21	II

A.2 Ionization Energies

Table A.3: Relevant ionization energies for the measurement of $4s_{1/2} - 4p_{3/2}$ transitions for 6 high-Z elements [67]. These calculated values have an estimated precision of about 1%.

Ionization Energies (keV)			
Element (Z)	Zn-like	Cu-like	Ni-like
Yb (70)	1.9943	2.0488	3.4546
W (74)	2.3708	2.4299	4.0648
Au (79)	2.8930	2.9581	4.8960
Pb (82)	3.2352	3.3039	5.4314
Th (90)	4.2614	4.3402	6.9933
U (92)	4.5456	4.6270	7.4144

B CONCAVE GRATING THEORY

B.1 Uniformly Spaced Grooves

Consider a spherically concave grating with a uniform groove separation, d, oriented with the x-axis normal to the grating at its center, the z-axis parallel to the grooves, and the y-axis completing the regular Cartesian coordinate system, as shown in Fig B.1. $A(x, y, z)$ represents a point on the entrance slit, $B(x', y', z')$ represents a focal point, $P(u, w, l)$ represents a point on the grating surface, and $O(0, 0, 0)$ indicates the origin of the coordinate system on the surface of the grating. For the condition of constructive interference of light from A, striking two grooves some distance, w, apart imaged at B, it must be true that the path difference, (Δ)

$$\Delta = \frac{m\lambda w}{d}, \tag{B.1}$$

where λ is the wavelength of light, and m is an integer $(m = 1, 2, 3 \cdots)$. For an arbitrary light path, the path function, F, may be written

$$F = AP + BP + \Delta \tag{B.2}$$

The distances AP and BP may be represented in terms of Cartesian coordinates as

$$(AP)^2 = (x - u)^2 + (y - w)^2 + (z - l)^2 \tag{B.3}$$

and

$$(BP)^2 = (x' - u)^2 + (y' - w)^2 + (z' - l)^2 \tag{B.4}$$

It is convienient to represent the distances from AO and BO in terms of their angles of incidence and diffraction in the xy-plane, therefore introducing cylindrical

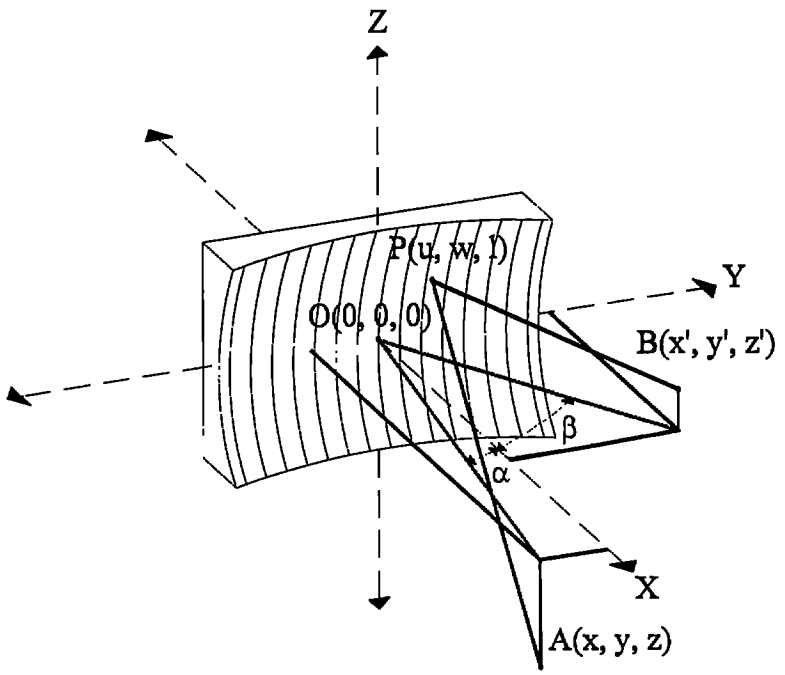

Figure B.1: Concave grating geometry.

coordinates with their origin coinciding with that of the Cartesian system,

$$\begin{aligned} x &= r\cos\alpha \quad x' = r'\cos\beta \\ y &= r\sin\alpha \quad y' = r'\sin\beta \end{aligned} \tag{B.5}$$

Note that the signs of α and β are opposite if A and B lie on different sides of the xz-plane.

Consider, also, that any point, P, on the grating surface lies on a sphere of radius, R, centered at the position (R, 0, 0), that can be represented by the equation

$$R^2 = (u - R)^2 + w^2 + l^2 \tag{B.6}$$

which, solved for u, yields

$$u = R \pm \sqrt{R^2 - (w^2 + l^2)} \tag{B.7}$$

Only the minus sign is important here since the plus sign represents solutions on the opposite side of the sphere where no grating exists. Inserting Eqs. B.5 and B.7 into Eq. B.3 yields the expression for $(AP)^2$

$$(AP)^2 = \left\{ r\cos\alpha - \left[R - \sqrt{R^2 - (w^2 + l^2)} \right] \right\}^2 + (r\sin\alpha - w)^2 + (z - l)^2 \tag{B.8}$$

which can be rearranged to be

$$(AP)^2 = r^2 - 2rw\sin\alpha + w^2 + (z-l)^2 + 2R^2 \left(1 - \frac{r\cos\alpha}{R}\right)\left(1 - \sqrt{1 - \frac{w^2 + l^2}{R^2}}\right) \tag{B.9}$$

By series expansion of the term within the square root of the form
$(1 - \frac{a}{b}) \Longrightarrow 1 - \frac{1}{2}\frac{a}{b} - \frac{1}{8}(\frac{a}{b})^2 - \frac{1}{16}(\frac{a}{b})^3 + \cdots$ where $a < b$, then

$$(AP)^2 = (r - w\sin\alpha)^2 + (z-l)^2 - l^2\frac{r\cos\alpha}{R} + w^2(\cos^2\alpha - \frac{r\cos\alpha}{R}) + \left(1 - \frac{r\cos\alpha}{R}\right)\left[\frac{(w^2+l^2)^2}{4R^2} + \frac{(w^2+l^2)^3}{8R^4} + \cdots\right] \tag{B.10}$$

Taking the square root of both sides and expanding the right hand side leads to the result

$$AP = r - w\sin\alpha + \frac{w^2(\frac{\cos^2\alpha}{r} - \frac{\cos\alpha}{R})}{2(r - w\sin\alpha)} + \frac{l^2(\frac{1}{r} - \frac{\cos\alpha}{R})}{2(r - w\sin\alpha)} 2(r - w\sin\alpha) + \frac{z^2 - 2lz}{2(r - w\sin\alpha)} + \frac{(1 - \frac{r\cos\alpha}{R})}{2(r - w\sin\alpha)}\left(\frac{(w^2+l^2)^2}{8R^2}\right) + \frac{(1 - \frac{r\cos\alpha}{R})}{2(r - w\sin\alpha)}\left(\frac{(w^2+l^2)^3}{16R^4}\right) + \cdots - \frac{w^4(\cos^2\alpha - \frac{r\cos\alpha}{R})^2}{8(r - w\sin\alpha)^3} - \cdots + HOT \tag{B.11}$$

where HOT refers to higher order terms not considered here. Expanding
$\left(1 - \frac{w\sin\alpha}{r}\right) \Longrightarrow \left(1 + \frac{w\sin\alpha}{r} + \left(\frac{w\sin\alpha}{r}\right)^2 + \cdots\right)$

yields a final expression for AP

$$AP = r - w\sin\alpha + \frac{w^2}{2}\left(\frac{\cos^2\alpha}{r} - \frac{\cos\alpha}{R}\right) + \frac{l^2}{2}\left(\frac{1}{r} - \frac{\cos\alpha}{R}\right) - \frac{lz}{r} + \frac{z^2}{2r} + \frac{(w^2+l^2)^2}{8R^2}\left(\frac{1}{r} - \frac{\cos\alpha}{R}\right) - \frac{w^4}{8r^2}\left(\frac{\cos^2\alpha}{r} - \frac{\cos\alpha}{R}\right)^2 + \frac{w^3\sin\alpha}{2r}\left(\frac{\cos^2\alpha}{r} - \frac{\cos\alpha}{R}\right) + \frac{l^2 w\sin\alpha}{2r}\left(\frac{1}{r} - \frac{\cos\alpha}{R}\right) + \frac{w\sin\alpha}{2r^2}(-2lz + z^2) + \frac{(w^2+l^2)^2 w\sin\alpha}{8R^2 r}\left(\frac{1}{r} - \frac{\cos\alpha}{R}\right) + \frac{w^4\sin^2\alpha}{2r^2}\left(\frac{\cos^2\alpha}{r} - \frac{\cos\alpha}{R}\right) + \frac{l^2 w^2\sin^2\alpha}{2r^2}\left(\frac{1}{r} - \frac{\cos\alpha}{R}\right) + \frac{w^2\sin^2\alpha}{2r^3}(-2lz + z^2) + \cdots \tag{B.12}$$

A similar expression can be found for BP by replacing all of the rs by r's, the zs by z's, and the αs by βs.

Finally, an expression for F can be written as

$$F = F_1 + F_2 + F_3 + F_4 + F_5 + HOT(w,l) + \Delta \tag{B.13}$$

where

$$F_1 = r + r' - w\left(\sin\alpha\left(1 - \frac{z^2}{2r^2}\right) + \sin\beta\left(1 - \frac{z'^2}{2r'^2}\right)\right) - l\left(\frac{z}{r} + \frac{z'}{r'}\right) \tag{B.14}$$

$$F_2 = \frac{w^2}{2}\left(\frac{\cos^2\alpha}{r} - \frac{\cos\alpha}{R}\right) + \frac{w^2}{2}\left(\frac{\cos^2\beta}{r'} - \frac{\cos\beta}{R}\right) + \frac{w^3 sin\alpha}{2}\left(\frac{\cos^2\alpha}{r} - \frac{\cos\alpha}{R}\right) + \frac{w^3\sin\beta}{2}\left(\frac{\cos^2\beta}{r'} - \frac{\cos\beta}{R}\right) + \frac{w^4 sin^2\alpha}{2}\left(\frac{\cos^2\alpha}{r} - \frac{\cos\alpha}{R}\right) + \frac{w^4\sin^2\beta}{2}\left(\frac{\cos^2\beta}{r'} - \frac{\cos\beta}{R}\right) + \cdots \tag{B.15}$$

$$F_3 = \frac{l^2}{2}\left(\frac{1}{r} + \frac{1}{r'} - \frac{1}{R}(\cos\alpha + \cos\beta)\right) + \frac{z^2}{2r} + \frac{z'^2}{2r'} \tag{B.16}$$

$$F_4 = \frac{l^2 w\sin\alpha}{2r}\left(\frac{1}{r} - \frac{\cos\alpha}{R}\right) + \frac{l^2 w\sin\beta}{2r'}\left(\frac{1}{r'} - \frac{\cos\beta}{R}\right) - \frac{wlz\sin\alpha}{r^2} - \frac{wlz'\sin\beta}{r'^2} \tag{B.17}$$

$$F_5 = \frac{(w^2+l^2)^2}{8R^2}\left(\frac{1}{r} + \frac{1}{r'} - \frac{1}{R}(\cos\alpha + \cos\beta)\right) \tag{B.18}$$

By Fermat's Principle of least time, point B is located such that F will be an extreme for any point P. Since A and B are fixed while P is any point on the grating, the conditions for F to be an extreme are

$$\frac{\partial F}{\partial w} = 0 \; and \; \frac{\partial F}{\partial l} = 0 \tag{B.19}$$

If these were to be true for any pair (w, l) for a fixed point B, then B would be in perfect focus. However, since $\partial F/\partial w$ and $\partial F/\partial l$ are still functions of l and w these functions may not be made zero for B unless the constant term and all coefficients of l and w in $\partial F/\partial w$ and $\partial F/\partial l$ are made zero. This can not be done for a concave grating. The reason is stated clearly by Namioka [47]:

> A ray diffracted from a point $P(w, l)$ goes in the direction specified by β and z'/r' which are determined by ($\partial F/\partial w$ and $\partial F/\partial l$). Since β and z'/r' are functions of w and l, this direction of the diffracted ray changes slightly with the position of the point P. Therefore, when the point P wanders over the ruled area of the grating, diffracted rays fall on slightly different points on the focal plane. In order to produce an image with the least aberration, the dependence of β and z'/r' on w and l must be minimized.

In the strictest sense, all kinds of aberrations are closely related to each other and should be treated as a whole for a given system. However, for the purposes here, to a good approximation the components of F can still be treated as if independent. Considering the terms first order in w and l, that is $F_1 + \Delta$, from B.19

$$\frac{\partial (F_1 + \Delta)}{\partial l} = \frac{z}{r} + \frac{z'}{r'} = 0$$

therefore,

$$\frac{z}{r} = -\frac{z'}{r'}$$

Similarly,

$$\frac{\partial(F_1 + \Delta)}{\partial w} = -\left(\sin\alpha\left(1 - \frac{z^2}{2r^2}\right) + \sin\beta\left(1 - \frac{z'^2}{2r'^2}\right)\right) + \frac{m\lambda}{d} = 0$$

Therefore,

$$\frac{m\lambda}{d} = \left(1 - \frac{z^2}{2r^2}\right)(\sin\alpha + \sin\beta) \tag{B.20}$$

This equation is a first order approximation to the geometric relation between the object and image points known as *the grating equation*. In most cases, $z \ll r$ and the term $z^2/2r^2$ can be neglected.

In a similar way, consider the lowest order term in w for F_2. $\partial F_2/\partial l = 0$, identically. Further, from $\partial F_2/\partial w = 0$ we have

$$w\left(\frac{\cos^2\alpha}{r} - \frac{\cos\alpha}{R} + \frac{\cos^2\beta}{r'} - \frac{\cos\beta}{R}\right) = 0$$

From this,

$$\cos\alpha\left(\frac{\cos\alpha}{r} - \frac{1}{R}\right) + \cos\beta\left(\frac{\cos\beta}{r'} - \frac{1}{R}\right) = 0$$

By inspection, two solutions to this are

$$r = R\cos\alpha \text{ and } r' = R\cos\beta \tag{B.21}$$

and

$$r = \infty \text{ and } r' = \frac{R\cos^2\beta}{\cos\alpha + \cos\beta} \tag{B.22}$$

Equation B.21 is the equation of a circle in polar coordinates and is known as the Rowland Circle. Equation B.22 is the condition that the source be at an infinite

distance away. Consider, now, F_3. $\partial F_3/\partial w = 0$, identically. From $\partial F_3/\partial l = 0$

$$l\left(\frac{1}{r} - \frac{\cos\alpha}{R} + \frac{1}{r'} - \frac{\cos\beta}{R}\right) = 0$$

Two solutions to this are

$$r = \frac{R}{\cos\alpha} \; and \; r' = \frac{R}{\cos\beta} \tag{B.23}$$

and

$$r = \infty \; and \; r' = \frac{R}{(\cos\alpha + \cos\beta)} \tag{B.24}$$

Equation B.23, complementary to B.21, is the equation of a straight line tangent to the Rowland circle. Therefore any point on the tangent will be focused vertically and brought to a horizontal astigmatic line on the same tangent. Equation B.24 shows the condition to be satisfied for stigmatic imaging when the source is at infinity. Further corrections can be made in this way. As will be seen in the next section, there is another way to reduce the aberrations of a concave grating.

B.2 Variably Spaced Grooves

Consider the case of a spherically shaped concave grating with a groove spacing that is allowed to vary as a function of w, the horizontal distance from the center of the grating. Such a grating is described by Harada and Kita [48]. They consider an in-plane mounting such that $z = z' = 0$ and a ruling machine that defines the blank translation from the center of the grating to the nth groove as a function of w_0 and θ, the tilt angle of the ruling tool with respect to the yz plane, as

$$w_0 = w - n\tan\theta \tag{B.25}$$

Therefore, the relation between the groove number and position can be written

$$n = \frac{1}{d_0}\left(w_0 + \frac{b_2}{R}w_0^2 + \frac{b_3}{R^2}w_0^3 + \frac{b_4}{R^3}w_0^4 + \cdots\right)$$

where d_0 is the groove spacing at $w_0 = 0$, and b_i are the ruling parameters. The groove spacing, d, can be written

$$d = d_0 \Big/ \left(1 + \frac{2b_2}{R}w_0 + \frac{3b_3}{R^2}w_0^2 + \frac{4b_4}{R^3}w_0^3 + \cdots\right) \tag{B.26}$$

From these equations we can write the modified path function as

$$F = r + r' + wF_{10} + w^2F_{20} + l^2F_{02} + w^3F_{30} + wl^2F_{12} + w^2l^2F_{22} + w^4F_{40} + l^4F_{04} + HOT \tag{B.27}$$

Some of the terms in Eq. B.27 follow:

$$F_{10} = -(\sin\alpha + \sin\beta) + \frac{m\lambda}{d}$$

$$F_{20} = \frac{1}{2}\left(\frac{\cos^2\alpha}{r} - \frac{\cos\alpha}{R}\right) + \frac{1}{2}\left(\frac{\cos^2\beta}{r'} - \frac{\cos\beta}{R}\right) + \frac{m\lambda}{dR}\left(b_2 - \frac{\tan\theta}{2}\right)$$

$$F_{02} = \frac{1}{2}\left(\frac{1}{r} - \frac{\cos\alpha}{R}\right) + \frac{1}{2}\left(\frac{1}{r'} - \frac{\cos\beta}{R}\right) - \frac{m\lambda\tan\theta}{2dR}$$

$$F_{30} = \frac{\sin\alpha}{2r}\left(\frac{\cos^2\alpha}{r} - \frac{\cos\alpha}{R}\right) + \frac{\sin\beta}{2r'}\left(\frac{\cos^2\beta}{r'} - \frac{\cos\beta}{R}\right) + \frac{m\lambda}{dR^2}\left(b_3 - b_2\tan^2\theta\right)$$

$$F_{12} = \frac{\sin\alpha}{2r}\left(\frac{1}{r} - \frac{\cos\alpha}{R}\right) + \frac{\sin\beta}{2r'}\left(\frac{1}{r'} - \frac{\cos\beta}{R}\right) - \frac{m\lambda b_2\tan\theta}{dR^2}$$

The terms of this path function are closely related to those of the uniformly spaced groove grating. F_{10} is related to the dispersion of the grating, F_{20} to the horizontal focus, F_{02} to the astigmatism, F_{30} to coma-type aberration, and so forth. As with the uniformly spaced groove grating, the components of the path function including modifications for the varying groove spacing can be treated separately. And, again, as it is impossible to satisfy both conditions from Fermat's Principle simultaneously, each of the terms F_{ij} must be made zero or minimized to reduce aberration. However, the inclusion of the ruling parameters allows more flexibility in this elimination or reduction. The gratings used in this work are of this type, collectively known

as *variably-line-spaced gratings*, or simply as *VLS gratings*. A subtle, yet powerful, advantage to this type of grating occurs at grazing incidence. It is possible to choose the ruling parameters in such a way that the diffracted rays focus on a plane which is nearly perpendicular to direction of travel of the diffracted rays. This advantage is discussed further in the main body of text.

C CCD FILTER PROGRAM

The CCD filter program was written for the purpose of reading a 2-dimensional array stored as a binary file created by Photometrics Imaging Software, *PMIS*, determining which of the pixels have been rendered un-usable by cosmic particles, eliminating these pixels from the data, collapsing the usable data to a 1-dimensional 'line out' spectrum, and outputting this information as an ASCII file. The purpose of this appendix is to describe the process by which the filtering is done and other important details. A copy of the program can be obtained from the Author upon request.

Each pixel in the file is independently examined. The general process of the filtering of the data involves that each pixel is compared to neighboring pixels using criteria input by the user before filtering. The primary condition for identifying a pixel as bad is that it has an exceptionally large number of counts as compared to its neighbors. This would indicate that the counts were created by a single, anomalous event rather than the accumulation of charge from successive photons hitting the chip. Throughout most of the filtering process there are three active columns of data. This is true except for filtering of the first and last columns on the CCD and these special cases are handled separately. An outline of the program in flow-chart format is displayed in Fig. C.1 (see page 134). Prior to filtering, the user supplies the information regarding the filtering limits and the range of columns to be summed for the line out. The limits are defined as (for clarity, columns are designated by n, with an alphabetic range starting with 'a', and rows by i, with a numeric range beginning with '1': 'Across' means varying n; 'Along' means varying i):

- Step size across: Requires the difference between the currently active pixel and either of the neighboring pixels across the dispersion direction to be less than this limit.
- Step size along: Requires the difference between the currently active pixel and either of the neighboring pixels along the dispersion direction to be less than this limit.
- Maximum Value: Requires that any pixel have fewer than this number of counts.

The range of columns allows the user to choose how much of the spectrum should be added to the line-out. Various versions of the program produce one, three, or eight independent line-outs, which allows for sectioning of the data. Other user supplied information is:

- File name and path
- Number of consecutive files to be filtered
- Request for output file in PMI software format
- Request for histogram of counts
- Bias Value: the most likely number of counts that a bad pixel would have if not for the anomalous event. This is used when filtering the first and last columns only.

Use of this software is an iterative task. It is necessary to examine the output file to be assured that the bad pixels have been satisfactorily eliminated, while avoiding cutting away important spectral information. By making adjustments to the maximum pixel allowance and the two step-sizes, the user can optimize the filtering process.

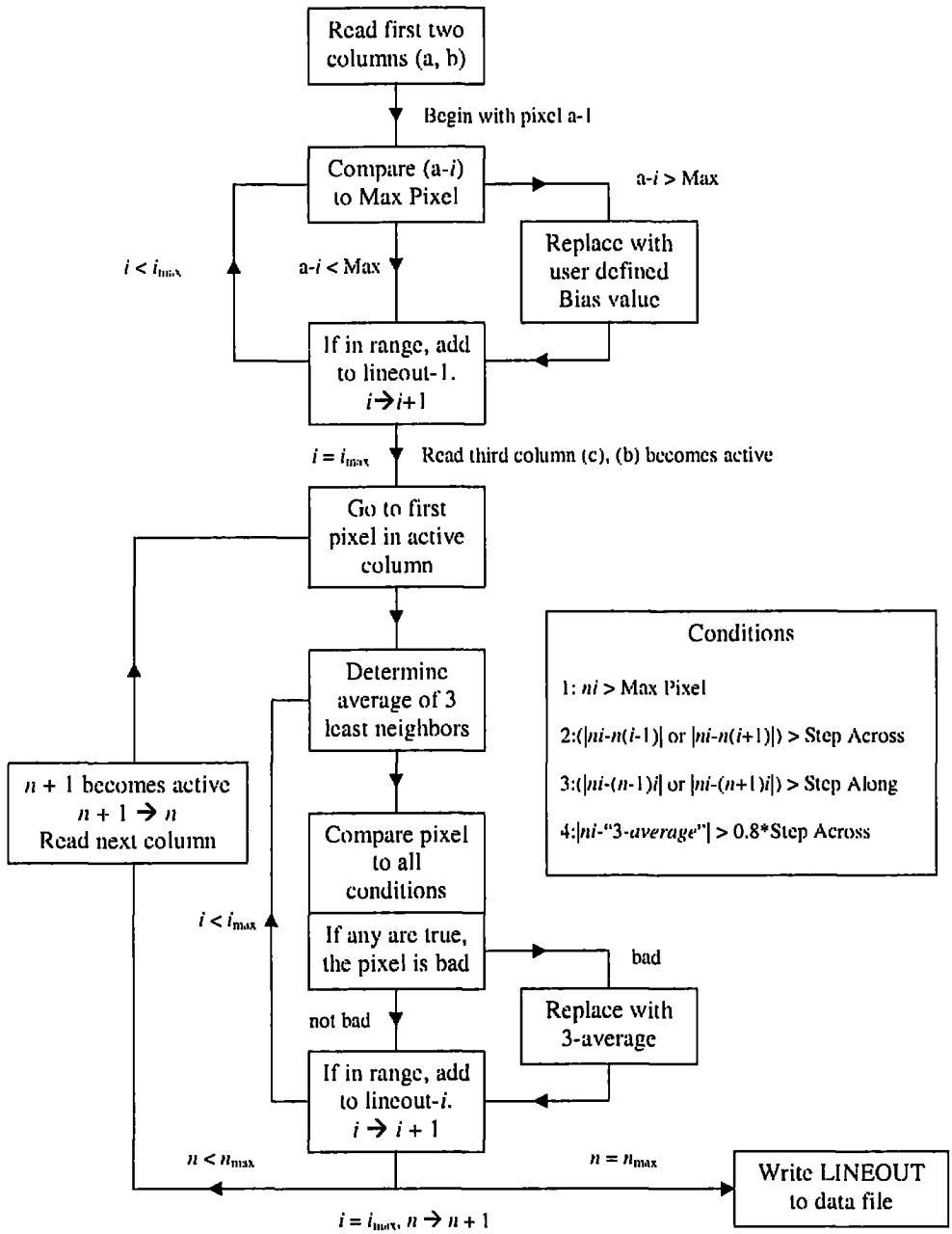

Figure C.1: CCD filter program outline.

REFERENCES

[1] I.H. Hutchinson. *Principles of Plasma Diagnostics.* Cambridge University Press, 1987. ISBN 0-521-38583-0.

[2] M.L. Apicella, G. Apruzzese, M. Borra, G. Bracco, M. Ciotti, I. Condrea, F. Crisanti, R. de Angelis, C. Ferro, L. Gabellieri, G. Gatti, H. Kroegler, M. Leigheb, G. Maddaluna, G. Maruccia, G. Mazzitelli, D. Pacella, V. Pericoli-Ridolfini, L. Pieroni, R. Zagorski, F. Alladio, R. Bartiromo, G. Buceti, P. Buratti, C. Centioli, V. Cocilovo, B. Esposito, A. Frattolillo, E. Giovannozzi, M. Grolli, A. Imparato, L. Lovisetto, P. Micozzi, S. Migliori, A. Moleti, F. Orsitto, L. Panaccione, M. Pannella, S. Podda, G.B. Righetti, E. Sternini, A.A. Tuccillo, O. Tudisco, F. Valente, V. Vitale, R. Zanino, V. Zanza, and M. Zerbini. Experiments in FTU with different limiter materials. *Nucl. Fusion.*, 37(3):381–396, 1997.

[3] E. Hinnov, K. Bol, D. Dimock, R.J. Hawryluk, D. Johnson, M. Mattioli, E. Meservey, and S. Von Goeler. Effects of tungsten radiation on the behaviour of PLT tokamak discharges. *Nucl. Fusion.*, 18(9):1305–1307, 1978.

[4] R. Parker, G. Janeschitz, H.D. Pacher, D. Post, S. Chiocchio, G. Federici, P. Ladd, ITER Joint Central Team, and Home Team. Plasma-wall interactions in ITER. *J. Nucl. Mater.*, 241-243:1–26, 1997.

[5] D. Naujoks, K. Asmussen, M. Bessenrodt-Weberpals, S. Deschka, R. Dux, W. Engelhardt, A.R. Field, G. Fussmann, J.C. Fuchs, C. Garcia-Rosales, S. Hirsch,

P. Ignacz, G. Lieder, K.F. Mast, R. Neu, R. Radtke, J. Roth, U. Wenzel, and the ASDEX Upgrade Team. Tungsten as target material in fusion devices. *Nucl. Fusion.*, 36(6):671–687, 1996.

[6] C. García-Rosales. Erosion processes in plasma-wall interactions. *J. Nucl. Mater.*, 211:202–214, 1994.

[7] J.F. Seely, C.M. Brown, and W.E. Behring. Transitions in Fe-, Co-, Cu-, and Zn-like ions of W and Re. *J. Opt. Soc. Am. B*, 6(1):3–6, January 1989.

[8] C.M. Brown, J.F. Seely, D.R. Kania, B.A. Hammel, C.A. Back, R.W. Lee, A. Bar-Shalom, and W.E. Behring. Wavelengths and energy levels for the Zn I isoelectronic sequence Sn^{20+} through U^{62+}. *At. Data Nucl. Data Tables*, 58(2):203–217, November 1994.

[9] J.F. Seely, C.M. Brown, and U. Feldman. Wavelengths and energy levels for the Cu-like isoelectronic sequence Ru^{15+} through U^{63+}. *At. Data Nucl. Data Tables*, 43(1):145–159, September 1989.

[10] R.C. Isler, R.V. Neidigh, and R.D. Cowan. Tungsten radiation from tokamak-produced plasmas. *Phys. Rev. A*, 63(3):295–297, 1977.

[11] M. Finkenthal, L.K. Huang, S. Lippmann, H.W. Moos, P. Mandelbaum, J.L. Schwob, and M. Klapisch. Soft X-ray bands of highly ionized tungsten, gold, and lead emitted by the TEXT tokamak plasma. *Physics Lett. A*, 127(5):255–258, February 1988.

[12] K. Asmussen, K.B. Fournier, J.M. Laming, R. Neu, J.F. Seely, R. Dux, W. Engelhardt, J.C. Fuchs, and the ASDEX Upgrade Team. Spectroscopic investigations

of tungsten in the EUV region and the determination of its concentration in tokamaks. *Nucl. Fusion.*, 38(7):967–986, July 1998.

[13] K.B. Fournier. Atomic data and spectral line intensities for highly ionized tunsten (Co-like W^{47+} to Rb-like W^{37+}) in a high-temperature low-density plasma. *At. Data Nucl. Data Tables*, 68:1–48, January 1998.

[14] J.R. Crespo López-Urrutia, P. Beiersdorfer, K. Widmann, B.B. Birkett, A.-M. Mårtensson-Pendrill, and M.G.H. Gustavsson. Nuclear magnetization distribution radii determinsed by hyperfine transitions in the 1s level of H-like ions $^{185}Re^{74+}$ and $^{187}Re^{74+}$. *Phys. Rev. A*, 57(2):879–887, February 1998.

[15] W.R. Johnson, S.A. Blundell, and J. Sapirstein. Many-body perturbation-theory calculations of energy levels along the copper isoelectronic sequence. *Phys. Rev. A*, 42(3):1087–1095, August 1990.

[16] Y.-K. Kim, D.H. Baik, P. Indelicato, and J.P. Desclaux. Resonance transition energies of Li-like, Na-like, and Cu-like ions. *Phys. Rev. A*, 44(1):148–166, July 1991.

[17] S.A. Blundell. Calculations of the screened self-energy and vacuum polarization in Li-like, Na-like, and Cu-like ions. *Phys. Rev. A*, 47(3):1790–1803, March 1993.

[18] K.T. Cheng and R.A. Wagner. Quantum electrodynamics efforts in the $4s - 4p$ transitions in Cu-like and Zn-like ions. *Phys. Rev. A*, 36(11):5435–5438, December 1987.

[19] J. Sugar and V. Kaufman. Predicted wavelengths and transition rates for magnetic-dipole transitions within $3s^2 3p^n$ ground configurations of ionized cu to mo. *J. Opt. Soc. Am. B*, 1(1):218–223, April 1984.

[20] V. Kaufman and J. Sugar. Forbidden lines in ns^2np^k ground configurations and nsnp excited configurations of beryllium through molybdenum atoms and ions. *J. Phys. Chem. Ref. Data*, 15(1):321–426, 1986.

[21] U. Feldman, P. Indelicato, and J. Sugar. Magnetic dipole line from U-LXXI ground-term levels predicted at 3200 Å. *J. Opt. Soc. Am. B*, 8(1):3–5, January 1991.

[22] S. Suckewer and E. Hinnov. Observation of a forbidden line of Fe XX and its application for ion temperature measurements in the princeton large torus tokamak. *Phys. Rev. Lett.*, 41(11):756–759, September 1978.

[23] C.A. Morgan, F.G. Serpa, E. Takács, E.S. Meyer, J.D. Gillaspy, J. Sugar, J.R. Roberts, C.M. Brown, and U. Feldman. Observation of visible and uv magnetic dipole transitions in highly charged xenon and barium. *Phys. Rev. Lett.*, 74(10):1716-1719, March 1995.

[24] R.E. Marrs, M.A. Levine, D.A. Knapp, and J.R. Henderson. Measurement of electron-impact-excitation cross sections for very highly charged ions. *Phys. Rev. Lett.*, 60(17):1715–1718, April 1988.

[25] M.A. Levine, R.E. Marrs, D.A. Knapp, and M.B. Schneider. The electron beam ion trap: a new instrument for atomic physics measurements. *Phys. Scr.*, T22:157–163, 1988.

[26] M.A. Levine, R.E. Marrs, J.N. Bardsley, P. Beiersdorfer, C.L. Bennett, M.H. Chen, T. Cowan, D. Dietrich, J.R. Henderson, D.A. Knapp, A. Osterheld, B.M. Penetrante, M.B. Schneider, and J.H. Scofield. The use of and electron beam ion trap in the study of highly charged ions. *Nucl. Instrum. Meth. B*, 43:431–440, 1989.

[27] S.R. Elliot, P. Beiersdorfer, and J. Nilsen. EBIT X-ray spectroscopy studies for applications to photo-pumped X-ray lasers. UCRL 116836, Lawrence Livermore National Laboratory, May 1994.

[28] S.B. Utter, P. Beiersdorfer, J.R. Crespo López-Urrutia, and K. Widmann. Position and size of the electron beam in the high-energy electron beam ion trap. *Nucl. Instrum. Meth. A*, 428:276–283, 1999.

[29] D. Vogel. Design and operation of the electron beam ion trap. UCRL 104990, Lawrence Livermore National Laboratory, May 1990.

[30] D.A. Knapp, R.E. Marrs, S.R. Elliott, E.W. Magee, and R. Zasadzinski. A high-energy electron beam ion trap for production of high-charge high-Z ions. *Nucl. Instrum. Meth. A*, 334:305–312, 1993.

[31] R.E. Marrs, P. Beiersdorfer, and D. Schneider. The electron-beam ion trap. *Phys. Today*, 47(10):27–34, October 1994. Errata: LLNL Ion–Trap Exp't's Austrian Apparatus, Physics Today, Vol.48 March 1995, pg.128.

[32] R.E. Marrs, P. Beiersdorfer, S.R. Elliot, D.A. Knapp, and T. Stoehlker. The super electron beam ion trap. *Phys. Scr.*, T59:941-944, 1995.

[33] K. Widmann. *High-resolution Spectroscopic Diagnostics of Very High-temperature Plasmas in the Hard X-ray Regime.* PhD thesis, Technische Universität Graz, June 1998. Work performed at LLNL EBIT.

[34] Evgeni D. Donets. Historical review of electron beam ions sources. *Rev. Sci. Instrum.*, 69(2):614-619, February 1998.

[35] P. Beiersdorfer and B.J. Wargelin. Low energy X-ray spectrometer for an electron beam ion trap. *Rev. Sci. Instrum.*, 65(1):13, January 1994.

[36] P. Beiersdorfer, R.E. Marrs, J.R. Henderson, D.A. Knapp, M.A. Levine, D.B. Platt, M.B. Schneider, D.A. Vogel, and K.L. Wong. High resolution x ray spectrometer for an electron beam ion trap. *Rev. Sci. Instrum.*, 61(9):2338–2342, September 1990.

[37] K. Widmann, P. Beiersdorfer, G.V. Brown, J.R. Crespo López Urrutia, V. Decaux, and D.W. Savin. A high–resolution transmission type x–ray spectrometer designed for observation of the Kα transitions of highly charged high–Z ions. *Rev. Sci. Instrum.*, 68(1):1087–1090, 1997.

[38] J.R. Crespo López-Urrutia, P. Beiersdorfer, D.W. Savin, and K. Widmann. Direct observation of the spontaneous emission of the hyperfine transition F=4 to F=3 in ground state hydrogenlike $^{165}Ho^{66+}$ in an electron beam ion trap. *Phys. Rev. Lett.*, 77(5):826–829, July 1996.

[39] P. Beiersdorfer, J.R. Crespo López-Urrutia, E. Förster, J. Mahiri, and K. Widmann. Very high resolution soft X-ray spectrometer for an electron beam ion trap. *Rev. Sci. Instrum.*, 68(1):1077-1079, January 1997.

[40] M.A. Levine, R.E. Marrs, C.L. Bennett, J.R. Henderson, D.A. Knapp, and M.B. Schneider. EBIT: Electron beam ion trap. In A. Hershcovitch, editor, *International Symposium on Electron Beam Ion Sources and Their Applications, AIP Conference Proceedings No. 188*, pages 82–101. AIP, New York, 1989.

[41] I.G. Brown, J.E. Galvin, B.F. Gavin, and R.A. MacGill. Metal vapor vacuum arc ion source. *Rev. Sci. Instrum.*, 57(6):1069–1084, June 1986.

[42] Marylin B. Schneider, Morton A. Levine, Charles L. Bennett, J.R. Henderson, D.A. Knapp, and R.E. Marrs. Evaporative cooling of highly charged ions in EBIT. In A. Hershcovitch, editor, *International Symposium on Electron Beam Ion Sources and Their Applications, AIP Conference Proceedings No. 188*, pages 158–165. AIP, New York, 1989.

[43] P. Beiersdorfer, L. Schweikhard, J.R. Crespo López-Urrutia, and K. Widmann. The magnetic trapping mode of an Electron Beam Ion Trap: New opportunities for highly charged ion research. *Rev. Sci. Instrum.*, 67(11):3818–3826, November 1996.

[44] H.A. Rowland. *Phil. Mag.*, 16:197 and 210, 1883. needs to be listed as citation from secondary source (sampson1967).

[45] J.A.R. Sampson. *Techniques of Vacuum Ultraviolet Spectroscopy.* Pied Publications, Lincoln, Nebraska, 1982.

[46] H.G. Beutler. Theory of the concave grating. *J. Opt. Soc. Am.*, 35(5):311-350, May 1945.

[47] T. Namioka. Theory of the concave grating. I. *J. Opt. Soc. Am.*, 49(5):446 460, May 1959.

[48] T. Harada and T. Kita. Mechanically ruled aberration-corrected concave gratings. *Appl. Opt.*, 19(23):3987–3993, 1980.

[49] J.L. Schwob, A.W. Wouters, and S. Suckewer. High-resolution duo-multichannel soft X-ray spectrometer for tokamak plasma diagnostics. *Journal of Electron Spectroscopy and Related Phenomena*, 67(3):463 478, June 1994.

[50] C.H. Skinner and J.L. Schwob. Charge-coupled-device detection of soft x rays for grazing-incidence spectrometers. *Appl. Opt.*, 35(22):4321 4324, August 1996.

[51] A. Saemann and K. Eidmann. Absolute calibration of a flat field spectrometer in the wavelenth range 10 70 Å. *Rev. Sci. Instrum.*, 69(5):1949 1954, May 1998.

[52] S.B. Utter, G. V. Brown, P. Beiersdorfer, E. J. Clothiaux, and N. K. Podder. Grazing-incidence measurements of L-shell emission from highly charged Fe in the soft X-ray region. *Rev. Sci. Instrum.*, 70(1):284–287, January 1999.

[53] H.T. Nguyen, B.W. Shore, S.J. Bryan, J.A. Britten, R.D. Boyd, and M.D. Perry. High-efficiency fused-silica transmission gratings. *Optics Letters*, 22(3):142 144, February 1997.

[54] G. Schriever, R. Lebert, A. Naweed, S. Mager, W. Neff, S. Kraft, F. Scholze, and G. Ulm. Calibration of charge coupled devices and a pinhole transmission grating to be used as elements of a soft X-ray spectrograph. *Rev. Sci. Instrum.*, 68(9):3301–3306, September 1997.

[55] Y. Li, G.D. Tsakiris, and R. Sigel. Self-calibration of a thinned backside-illuminated charge coupled device in the soft X-ray region. *Rev. Sci. Instrum.*, 66(1):80–86, January 1995.

[56] K.B. Fournier, August 1999. Private communication: Recalculation of the transition energies and intensity predictions for intermediate charge state W ions using parameters similar to those in EBIT.

[57] J.F. Seely, J.O. Ekberg, C.M. Brown, U. Feldman, W.E. Behring, J. Reader, and M.C. Richardson. Laser produced spectra and QED effects for Fe-, Co-, Cu-, and Zn-like ions of Au, Pb, Bi, Th, and U. *Phys. Rev. Lett.*, 57(23):2924–2926, December 1986.

[58] G. Tondello and T.M. Paget. Grazing incidence spectra of Ne VII and Ne VIII. *J. Phys. B*, 3:1757–1762, 1970.

[59] L.W. Phillips and W.L. Parker. Spectra of argon in the extreme ultraviolet. *Phys. Rev.*, 60:301–307, August 1941.

[60] L. Lyons. *Statistics for nuclear and particle physicists.* Press Syndicate of the University of Cambridge, New York, NY 10011-4211, USA, 1986.

[61] D.R. Kania, B.J. MacGowan, C.J. Keane, C.M. Brown, J.O. Ekberg, J.F. Seely, U. Feldman, and J. Reader. Transitions and energy-levels for Cu-like Yb^{41+}, Ta^{44+}, and U^{63+}. *J. Opt. Soc. Am. B*, 7(10):1993–1996, October 1990.

[62] G.A. Doschek, U. Feldman, C.M. Brown, J.F. Seely, J.O. Ekberg, W.E. Behring, and M.C. Richardson. Spectra and energy levels of Sm XXXIV, Eu XXXV, Gd XXXVI, and Yb XXXXII. *J. Opt. Soc. Am. B*, 5(2):243–246, February 1988.

[63] F.G. Serpa, E.S. Meyer, C.A. Morgan, J.D. Gillapsy, J. Sugar, J.R. Roberts, C.M. Brown, and U. Feldman. Anomalous Z dependence of a magnetic dipole transition in the Ti I isoelectronic sequence. *Phys. Rev. A*, 53(4):2220–2224, April 1996.

[64] D.J. Bieber, H.S. Margolis, P.K. Oxley, and J.D. Silver. Studies of magnetic dipole transitions in highly charged argon and barium using an electron beam ion trap. *Phys. Scr.*, T73:64-66, 1997.

[65] F.J. Currell, D. Kato, N. Nakamura, S. Ohtani, E.J. Sokell, H. Watanabe, and C. Yamada. Electron – ion interactions and spectroscopy of highly charged ions studied using the Tokyo EBIT. *Phys. Scr.*, T80:154–157, 1999.

[66] E. Träbert, P. Beiersdorfer, S.B. Utter, and J.R. Crespo López-Urrutia. Forbidden transitions in the visible spectra of an electron beam ion trap (EBIT). *Phys. Scr.*, 58(6):599–604, December 1998.

[67] J.H. Scofield. Ionization energies for particular number of bound electrons. private communication. Combination of values from Moore, relativistic Hartree-Slater and Hartree-Fock calculations.

[68] P. Indelicato. Relativistic effects in few-electron heavy ions. *Ab initio* evaluation of levels energy and transitions probabilities. *Phys. Scr.*, T65:57-62, 1996.

[69] D.R. Beck. Relativistic configuration-interaction results for Xe^{32+}, Ba^{34+}, Nd^{38+}, and Gd^{42+} "^5D" $J = 2$ to $J = 3$ energy differences. *Phys. Rev. A*, 56(3):2428-2430, September 1997.

[70] D. Kato, T. Fukami, T. Kinugawa, S. Ohtani, H. Watanabe, and C. Yamada. Magnetic-dipole transitions between ground-state fine-structure levels of Ti-like highly charged ions. In *Proceedings for 1999 ISAPP, Tokyo, Japan*, 1999. In press.

[71] W.R. Johnson and G. Soff. The Lamb shift in hydrogen-like atoms, $1 \leq Z \leq 100$. *At. Data Nucl. Data Tables*, 33(3):405–446, November 1985.

[72] G.W. Drake. Theoretical energies for the $n = 1$ and 2 states of the helium isoelectronic sequence up to $Z = 100$. *Can. J. Phys.*, 66:586–611, 1988.

[73] B. Edlén. Wavelength measurements in the vacuum ultra-violet. *Rep. Prog. Phys.*, 26:181–212, 1963.

[74] R.L. Kelly. *Atomic and Ionic Spectrum Lines below 2000 Ångstroms: Hydrogen through Krypton*, volume 16. American Chemical Society, 1155 16th St. N.W., Washington, DC 20036-9976, 1987. Supplement No. 1 of Journal of Physical and Chemical Reference Data.

[75] J. Reader and C.H. Corliss. *Wavelengths and Transition Probabilities for Atoms and Atomic Ions: Part 1.* National Standards Reference Data Series. U.S. Department of Commerce, National Bureau of Standards, nsrds-nbs 68 edition, 1980.